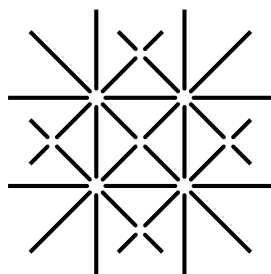# Energy level alignment and site-selective adsorption of large organic molecules on noble metal surfaces

Audrius Alkauskas

aus Anykščiai (Litauen)

UNI
BASEL

Basel, 2006

Genehmigt von der Philosophisch-Naturwissenschaftlichen Fakultät auf Antrag von

    Prof. Dr. Alexis Baratoff

    Dr. Rosa di Felice

    Prof. Dr. Christoph Bruder

Basel, den 24 Januar, 2006

                                    Prof. Dr. H.-J.Wirz, Dekan

Summary

In recent two decades, there has been a large interest in organic molecules on metallic as well as insulating substrates. This interest is caused by the need to understand fundamental properties of large organic molecules on solid surfaces at the level that properties of smaller adsorbates, like carbon monoxide or oxygen molecule, are understood. In addition, theoretical and experimental studies in this field are driven by potential applications of organic materials as active components in light-emitting diodes (OLEDs) and field-effect transistors (FETs), as well as by on-going efforts to use single molecules as building blocks in nano-electronic and nano-mechanical devices.

This Thesis deals with two aspects of large organic molecules on metal surfaces: local adsorption geometry and energy level alignment. Molecules bind to specific sites on metallic surfaces which correspond to the lowest total energy of the molecule-substrate system. It is of fundamental interest to understand the electronic causes of the interaction between the molecule and the surface. Ultimately, one would like to gain understanding of what causes molecule-substrate attraction and why this attraction is stronger for some particular geometries than for others. Another important aspect is the alignment of molecular levels with respect to the Fermi level of the metal. This level alignment governs the electron injection from the metal to the molecule (or vice versa) in electronic devices.

At the beginning of the Thesis, we review our main theoretical tool, density functional theory (DFT), and present details of the plane-wave implementation of DFT. We introduce concepts which are useful in analyzing surface science systems, such as surface energy, work function, electron density difference, difference in density of states, etc. We present calculations of copper and silver bulk and surfaces to assess how density functional theory performs for noble metals. We then investigate a specific surface science system to demonstrate these concepts, namely, chlorine adsorbed on the Ag(111) surface at submonolayer coverages. We find that the adsorption energy of Cl on Ag(111) is about 2.9 eV and depends only weakly on coverage. The Ag-Cl bond is very strong and can be best described as ionic. Adsorption of Cl on the Ag(111) surface leads to electron charge transfer from the metal to the adsorbate. Each chlorine atom acquires about 0.2 additional electrons upon adsorption. Because of this charge transfer the work function of adsorbate-covered substrate increases. We find a very good agreement between theory and available experimental data. Small dependence of adsorption energy on coverage can be explained by lateral repulsion of adsorption-induced dipoles.

Chapter 4 of the Thesis is devoted to site-selective adsorption of one specific molecule, 1,4,5,8-naphthalene tetracarboxylic dianhydride (NTCDA), on the Ag(110) surface. We perform large-scale density functional calculations of several local adsorption sites and

analyze the results in great detail. Calculations reveal that NTCDA prefers adsorption geometry in which the peripheral oxygen atoms lie directly above the silver atoms in the $[1\bar{1}0]$ atomic rows. This nicely agrees with available experimental data. From the analysis of DFT calculations we are able to understand why this happens. Firstly, NTCDA is a molecule with electron accepting properties. In the gas-phase molecule the oxygens of the side groups are negatively charged while the central naphthalene core is positively charged. When the molecule is adsorbed on the Ag(110) surface, about 0.4 electrons are transfered to the lowest occupied molecular orbital (LUMO). Silver atoms in the topmost atomic layer become positively charged and this causes electrostatic attraction between negatively charged oxygen atoms of NTCDA and positively charged silver atoms. This attraction is maximum when oxygens are just above the silver atoms in the $[1\bar{1}0]$ atomic rows. Thus, on the basis of DFT calculations, we have developed a model for site-selective adsorption of NTCDA on the Ag(110) surface. This model should also be applicable in case of adsorption of a related molecule, PTCDA, on the same surface.

In Chapter 5 we analyze the energy level alignment of copper octaethylporphyrin (CuOEP) on three metal surfaces: Ag(001), Ag(111) and Cu(111). The experiments that this analysis is based on were performed in the Institute of Physics of University of Basel, in the NanoLab group. We first critically review and discuss different physical mechanisms that lead to a formation of the interface dipole at metal-organic interfaces. These different mechanisms are: charge transfer (as described by the so-called induced density of interface states (IDIS) model), polarization of the adsorbate near the metal surface, push-back effect, which is a consequence of the Pauli exclusion principle, permanent electrostatic dipoles at interfaces, and charge transfer caused by chemical interactions. Then we discuss in detail experimental results and evaluate the contribution of each mechanism to the total interface dipole. We conclude that the push-back effect is the most important for CuOEP/metal interfaces.

Acknowledgements

The work presented in this Thesis was performed during more than 3.5 years, spent in Basel. Naturally, many people contributed through discussions, seminars and advice.

First and most of all, I would like to thank my supervisors Prof. Alexis Baratoff and Prof. Christoph Bruder for accepting me as a PhD student and for guiding me through the (sometimes dark) forest of science. Also many thanks to Dr. Rosa di Felice who agreed to co-referee the Thesis. I have benefited from the discussions with my experimental colleagues Simon Berner, Laurent Nony, Enrico Gnecco, Silvia Schintke, Markus Wahl, Matthias von Arx, and Thomas Jung. I am especially grateful to Luca Ramoino, whose UPS measurements are presented in Chapter 5. Only because of numerous discussions we had with him, the project reviewed in Chapter 5 could have been accomplished.

I am thankful to Prof. Stefan Goedecker for taking the duty to chair the PhD exam. The course on Computational Physics given by him also taught me a lot.

During all my stay in Basel I have officially belonged to the lively Condensed Matter Theory (CMT) group. In its theory seminars and journal clubs I have learned a lot of frontier physics outside my direct field of DFT calculations. Being exposed to the state-of-the-art results from the field outside your direct one is not always easy but always beneficial. The CMT group was also the one in which my institute life concentrated and I would like to thank all the people there. First of all, Prof. Daniel Loss whose competence and energy impressed me a lot. And, of course, all the colleagues there, both students and postdocs.

I would like express gratitude to Prof. Christian Schönenberger for organizing the Monday morning meetings, for the opportunity to take part in them, and for getting to know yet another brilliant physicist. As well, many thanks to all the members of the Nano-Electronics group.

The help from the staff of the University Computer Center, and especially Martin Jacquot, was invaluable. Without his technical assistance the work in the Thesis could not have been performed.

Separate chapters of the thesis were proof-read by Stefan Goedecker, Jörg Lehmann, Joël Peguiron, and Bill Coish. Needless to say, I am indebted to all of them.

Last, but not least, I would like to express my gratitude to the head of the Iranian crew in the Institute of Physics, Javad Farahani, a friend and a colleague, with whom a lot of hours outside the Institute were spent. Finally, I thank all the members of the small and ever changing Lithuanian community in Basel which has made my life easier here.

Abreviations

B3LYP	Becke's three-parameter hybrid density functional
CuOEP	Copper octaethylporphyrin
DFT	Density functional theory
EA	Electron affinity
EN	Electronegativity
GGA	Generalized gradient approximation
HOMO	Highest occupied molecular orbital
IP	Ionization potential
LDA	Local density approximation
LEED	Low energy electron diffraction
LUMO	Lowest unoccupied molecular orbital
NEXAFS	Near-edge X-ray absorption fine structure
NTCDA	1,4,5,8-naphthalene tetracarboxylic acid dianhydride
NTCDI	1,4,5,8-naphthalene tetracarboxylic acid diimide
PP	Pseudopotential
PBE	Perdew-Burke-Ernzerhof GGA functional
PTCDA	3,4,9,10-perylene tetracarboxylic acid dianhydride
PTCDI	3,4,9,10-perylene tetracarboxylic acid diimide
STM	Scanning tunneling microcope
STS	Scanning tunneling spectroscopy
TPDS	Temperature programmed desorption spectroscopy
UPS	Ultraviolet photoelectron spectroscopy
XPS	X-ray photoelectron spectroscopy

List of symbols

$\mathcal{D}(E)$ Density of states

$\Delta\mathcal{D}(E)$ Change in density of states

E_{ad} Adsorption energy

E_S Surface energy

$\mathcal{E}$ Electric field

$n(\mathbf{r})$ Electron density

$\Delta n(\mathbf{r})$ Density difference function

Φ Work function of the surface

V_{KS} Kohn-Sham potential

H_{KS} Kohn-Sham Hamiltonian

ε_F^v Position of HOMO of the molecule with respect to the Fermi energy in the metal

ε_F^c Position of LUMO of the molecule with respect to the Fermi energy in the metal

Δ Work function change

$S_D,\ S_B$ Interface slope parameters

A_{xy} Area of the surface unit cell

μ Chemical potential, electric dipole moment

θ Coverage

Contents

Chapter 1

Introduction

1.1   Molecular nanoscience and organic electronics

From the early days of civilized humanity, and especially in the past few centuries, the world of science and technology has witnessed numerous occasions when fundamental scientific ideas turn into commercial devices and gadgets. In the era of information technologies this ancient collaboration between fundamental science and industry continues to be fruitful. To fulfill the constant need for faster operation, denser information storage and shorter communication times of electronic devices, the scientific community has always to search for alternative ways to perform these basic operations. However, there are fundamental limits to all of these processes. These limits are set by nature, and in particular by the size of usual everyday matter - atoms and molecules. It is difficult to imagine a smaller bit of information than a single atom; communication times shorter than the time it takes a photon to travel a distance of atomic size is also difficult to conceive. In addition, no smaller conductor than an atom or a small molecule exists. Thoughts like these have given birth to a new area of science - molecular nanotechnology, which represents the bottom-up branch of the field of nanoscience. Together with its top-down counterpart, semiconductor nanotechnology, it forms the fast-growing and ever-wider field of nanoscience and nanotechnology.

If a molecule or an atom should one day become a working electronic device, they will do so only when in contact with a solid - a metal or a semiconductor. The device is not useful if information cannot be written to it, a current passed through it, or a voltage-drop measured. In addition, useful molecular machines, which will behave like atomistic equivalents of macroscopic machines, would not hang in air or in vacuum, but rather reside on a solid substrate. Thus molecules on solid substrates are of big importance for the entire field of nanoscience.

The field of molecular electronics [1, 2, 3, 4, 5, 6] is just a part of molecular nanoscience [7, 8, 9], but a very important one. The idea is to explore the transport characteristics of a single molecule attached to two or more electrodes. This area of science is indeed multidisciplinary, and people with different backgrounds not only study this fundamental problem by different means, but also look at it from different angles. Experimental solid state physicists, who always obtained the lion's share of information about their samples

from transport measurements, understood quite quickly that the smallest conductor is just a single atom or a single molecule. The problem they are facing is exactly what they were looking for: this conductor indeed *is so small*, that attaching it to the metallic electrodes is far from easy or, once done, not easily reproducible. Chemists have a vast knowledge and intuition about the electronic structure of molecules, their oxidation and reduction states, and recipes for synthesizing new molecules. They also, however, have to deal with the fact that it is not easy to have only one molecule in the junction. The situation is not any clearer on the theory side. Solid-state theorists from the mesoscopic physics community look at molecules as small quantum dots and apply their well-developed theoretical machinery to these smallest dots. Their worry, however, is that a great deal of parameters characterizing metal-molecule contacts are unknown and cannot be deduced from a phenomenological theory. This includes charge transfer between the subsystems, the broadening of molecular electronic states, their position with respect to the Fermi level of the metal, phonon spectrum of the combined system, electron-phonon coupling in the junction, etc. All of these properties are accessible to solid-state physicists from the electronic structure community, which have created reliable tools to predict such properties, density functional theory, for instance. Their *"Achilles' heel"* is electron transport itself, theories of which, within the electronic structure framework, are still in their infancy. A special role in this area of research is played by surface scientists. They have almost a century of experience investigating interactions of such different partners - a molecule with discrete energy levels, and a metal with a continuum of states. In addition, they have at their disposal suitable and ever-improving tools for the characterization of molecules on surfaces, like X-ray photoelectron spectroscopy (XPS), ultraviolet photoelectron spectroscopy (UPS), X-ray absorption spectroscopy (XAS), two photon spectroscopy (2PPES) [10], scanning tunneling microscopy (STM) [11,12] and atomic force microscopy (AFM). To use surface science techniques, one usually must work in ultra-high vacuum and there are strict requirements for the quality of the substrate. Thus, information about other environments, such as high pressures and room temperature, is not always accessible with such surface science tools.

The weaknesses of each scientific discipline are mentioned on purpose in the previous paragraph, with the intention to show that many problems remain unsolved, both in theory and experiment. In fact, what matters are the *strengths* of each branch of science, because their different way of looking at things is a great advantage.

Let us look at the main problem more closely. Figure 1.1 summarizes in brief the idea of **molecular electronics**. In Fig. 1.1a the molecule is between two gold contacts (leads) in a suspended geometry, while in Fig. 1.1b an artist's view of a more practical in-plane geometry is shown. In the latter case the molecule and electrodes are on the solid support, for instance, an insulator surface. Here a third additional electrode (called gate electrode) which can control the position of the molecular levels with respect to the Fermi energy in the metal, is also drawn. In both of these geometries, suspended and in-plane, the properties of the molecule-metal junction are crucial. In Fig. 1.1c the energy-level diagram of the device is sketched. Coupling of the molecular orbitals to the metal states leads to their broadening, i.e. a smearing of energy levels. Under an applied bias V there is an electron flow from the left electrode to the right one. In the linear regime, for non-interacting electrons or electrons moving in a self-consistent potential, the conductance
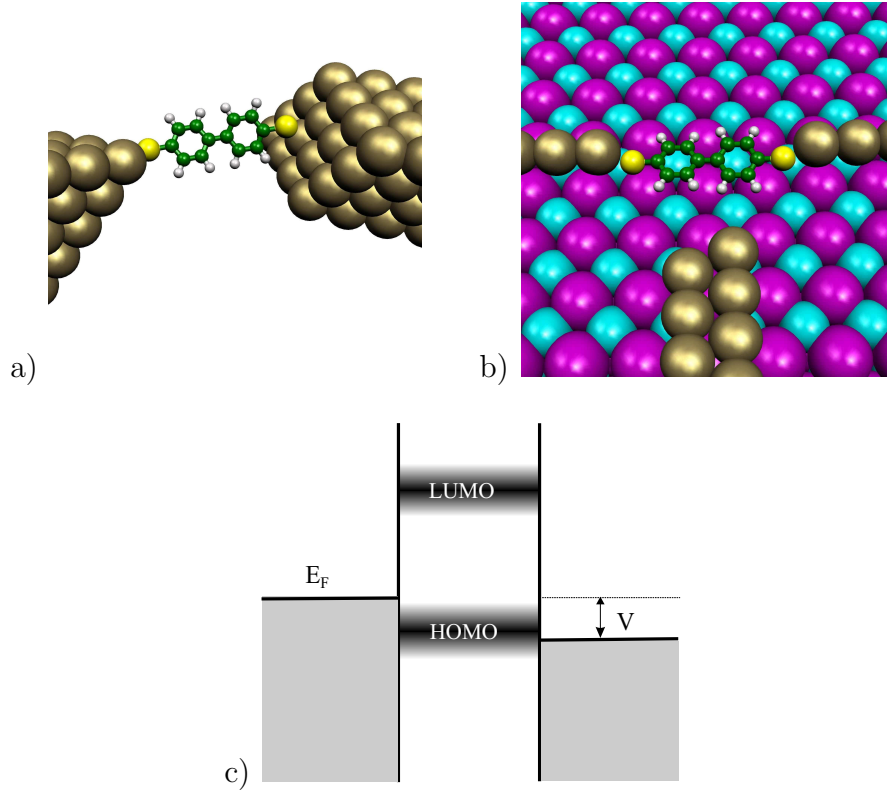
Figure 1.1: Molecular electronics: artist's view of the device in a) suspended geometry, b) in-plane geometry; c) the schematic energy level diagram. E_F is Fermi level of the metal, V is applied bias voltage, HOMO is the highest occupied molecular orbital, and LUMO is the lowest unoccupied molecular orbital.

of the device is given in terms of the famous Landauer formula [13]:

$$G = \frac{2e^2}{h} \Gamma_L \Gamma_R \left| G_C^R \right|^2 . \tag{1.1}$$

We assume that only one molecular level is relevant for transport. In Eq. (1.1), $G_0 = 2e^2/h$ is a conductance quantum, Γ_R and Γ_L are the imaginary parts of the self energies of the molecular state due to the coupling to the left and right electrode, respectively $(\Gamma = i \left(\Sigma^R - \Sigma^A \right))$. These quantities are measures of the escape rates of the electron from the molecular state to the metallic electrodes. G_C^R is the retarded Green's function of the molecular state, which, aside from information about self energies Σ, also contains information about the position of the molecular state with respect to the electronic states in the metal. Equation (1.1) is very instructive and the physical quantities that appear in it are of principle significance in this Thesis. It is important to stress that these quantities (Γs and G_C^R) describe the electronic structure of the metal-molecule contact, rather than a metal, or a molecule, alone. Therefore, the relevance of theoretical studies of metal-molecule contacts to the field of molecular electronics is unquestionable.

Both Γ, the coupling strength, and Green's function G_C^R, which contain information
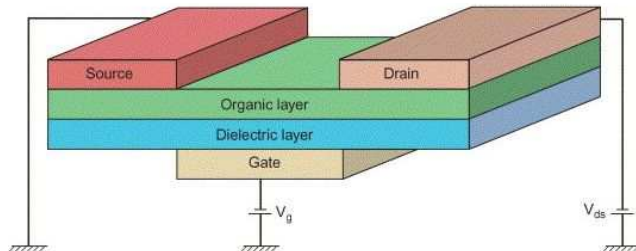
Figure 1.2: Schematic diagram of the organic field-effect transistor. The contact properties of the metallic electrodes (source and drain) with the organic semiconductor determine the characteristics of the device. From Ref. [16].
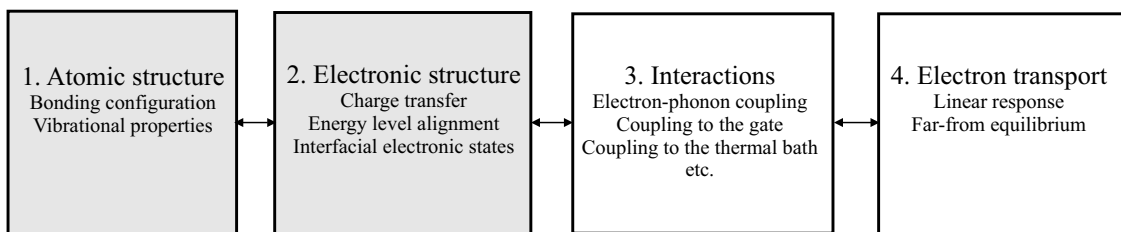
Figure 1.3: Four ingredients of the microscopic theory of molecular electronics: 1) Atomic structure of the metal-molecule contact; 2) Electronic ground state structure of the metal-molecule contact; 3) Interactions between different degrees of freedom and with the environment: electron-phonon coupling, and coupling to the thermal bath, gate electrodes, etc.; 4) Electron transport. The first two blocks represent ground state properties of metal-molecule contact and can be modelled with electronic structure methods.

about molecular levels, also depend strongly on the atomic structure of the contacts, such as bonding geometry, conformation and distortion of the molecule, deformation of the metal, etc. The atomic and electronic structure of the molecule - metal contact determines also mechanical properties of the system, which are explored in another sub-branch of molecular nanoscience - the field of **molecular machines**. Here, the idea is to build microscopic machines which would mimic macroscopic machines and would perform the desired task. Current research in this area is exemplified by beautiful experiments involving manipulation of organic molecules on noble metal surfaces [14, 15].

Contacts between organic components and metals are also important in the field of **organic electronics**. In this field, electronic transport in bulk organic materials, rather than through single molecules, is employed. Organic electronics is much more mature than molecular electronics, and several commercial devices are on the market already. The common feature of both molecular and organic electronics is the crucial role played by the metal-molecule contacts. Figure 1.2 shows the schematic diagram of the organic field-effect transistor (OFET) [16].

This Thesis presents theoretical work on several aspects of metal-molecule contacts, mainly local adsorption properties and energy-level alignment. Only the ground-state

atomic and electronic structure of organic molecules on metals will be discussed. One can then ask what is the relevance of the ground-state information to electron transport, which is *not* a ground-state phenomenon. In Fig. 1.3 four ingredients of the microscopic theory of molecular electronics are shown. These are the building-blocks of the theory, in which the subsequent block depends on the previous ones. To fully understand transport through the molecule, one has to know: 1) the atomic structure of the device; 2) the electronic structure of the device in equilibrium; 3) coupling between different degrees of freedom and to the environment. Only knowledge of all these constituents can lay the ground for 4) modelling of electron transport at the atomic scale under non-equilibrium conditions. In particular, blocks 1) and 2) form a starting point for such a theoretical investigation. They represent ground-state properties of the system and can be understood with electronic structure methods. All the problems which are investigated in this Thesis belong to the first two blocks in Fig. 1.3. Hence their relevance to molecular electronics and molecular nanoscience in general.

1.2 Review of theoretical modelling

Due to the fast development of computers and algorithms, computational science started has begun play an increasing role, comparable to that of theory and experiment. Electronic structure calculations, which deal with usual electronic matter and its interaction with various environments, now constitute probably what is the largest branch of computational physics and chemistry. Questions asked both in treating molecules and solids are very similar: the ground-state electronic structure of the system, the change of the total energy as a function of nuclear coordinates, phonon spectrum, electron-phonon coupling, static and dynamic polarizabilities, electronic excitations, etc. The methods used are different, however. Molecules are relatively small objects and modern-day computers allow for a very accurate treatment of such systems by techniques which are usually called *quantum chemistry* methods. Examples of these are configuration interaction (CI), Møller-Plesset perturbation theory, or coupled clusters [17]. These methods are use the Hartree-Fock wavefunction as a zeroth-order approximation to the total wavefunction, and *systematically* improve upon it by including the effects of electron correlation. The computational cost of such schemes grows extremely fast with the system size, but for small chemical systems the accuracy that is achieved is unrivaled.

The situation is very different in solid state physics. Here, one deals with a very large number of electrons. It is impossible (and not even useful) try to describe the entire system by a single wavefunction. However, if a many-electron problem can be cast into a single-electron problem (for instance, in the self-consistent field approach), the computational cost is drastically smaller, because now the problem is reduced to only one unit cell of the periodic lattice. The density functional theory of Kohn and Sham, being in principle an exact reformulation of ground-state quantum mechanics in terms of single-particle self-consistent field equations, is thus very suitable for solid state systems, as well as other extended systems, such as liquids and glasses. It is no wonder, therefore, that density functional theory (DFT) has become the most popular electronic structure theory in computational solid state physics [18, 19, 20]. It is usually DFT that physicists have in

mind when they speak about *ab initio* (first principles) calculations. DFT is used much less in chemistry (its death was even announced by a famous quantum chemist P.M.W. Gill [21]) and by *ab initio* chemists usually mean Hartree-Fock and post-Hartree-Fock methods mentioned above rather than DFT.

Density functional theory is the main theoretical tool used in this work, and therefore Chapter 2 is devoted to the description of this theory and its practical implementations. DFT was also the main subject of learning during the PhD studies of the author, and this also justifies a not-so-short description of the theory in Chapter 2. We discuss the theorems which provide the basis to use density as a basic variable in electronic structure. The most popular approximations to the exact exchange-correlation potential are discussed, too. Practical DFT calculations would not be feasible without the numerous technical developments which have occurred in the past several decades. These include, for instance, the development of soft norm-conserving *ab initio* pseudopotentials, efficient iterative diagonalization methods for metallic systems and efficient ways to approach self-consistency, accurate Brillouin zone integration schemes, improvements of geometry optimizers, etc. Mastery of all these tools is necessary to obtain reliable results in a meaningful time in any electronic structure calculation. All of these topics are areas of scientific research on their own (because their range of applicability sometimes is much broader than just DFT) and different implementation alternatives exist for each of them. Chapter 2 discusses specific implementations of these tools which are used to calculate the properties of metallic systems, in which we are most interested.

In Chapter 3 of this Thesis a simple physical system, chlorine adsorbed on the Ag(111) surface at sub-monolayer coverage, is studied. Our main goal in performing these calculations was to gain experience in different techniques that are specific to surface science problems, such as slab and supercell methods, as well as to become familiar with general computational tools. Post-processing of total energy calculations is also discussed. For instance, density difference functions, as instructive tools to gain insight into the physics of surface chemical bonds, are introduced. Also, calculations of the work functions of the adsorbate-covered surfaces are explained.

1.3 Adsorption of large aromatic molecules on noble metals

For self-assembly of organic molecules on solid surfaces to take place, several criteria should be fulfilled. Firstly, interaction of the molecule with the surface should be not too strong such that the molecule is still quite mobile on the surface. Transition metals with partially filled d-states are rather reactive and molecules stick to the surface during deposition and become immobile. Such a situation occurs even for near-noble metals Ni, Pd or Pt (electronic configuration in the solid state $(n-1)\,d^9 ns^1$). Similarly, molecules interact very strongly with the surfaces of elemental semiconductors (Si and Ge) or III-V semiconductors (GaAs).

On the other hand, the interaction of the molecule with a surface should also be not too weak. If the interaction is too weak, the molecules are too mobile at room
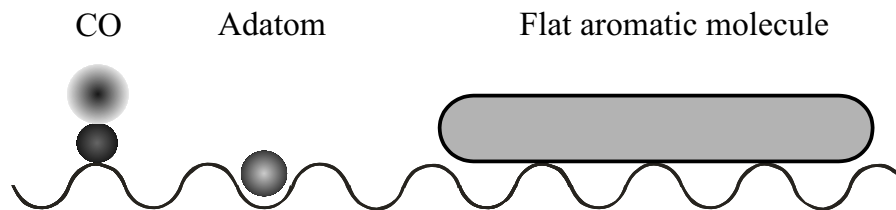
Figure 1.4: A sketch of (left) a C=O molecule, (middle) an adatom and (right) a large flat-lying π-conjugated molecule adsorbed on a metal surface.

temperature. The surfaces of noble metals Cu, Ag and Au (electronic configuration in the solid state $(n-1)\,d^{10}ns^1$) with filled d-states show intermediate reactivity, and therefore the majority of investigations of self-assembly of large organic molecules were performed on these surfaces. Another important requirement is that the interaction among the molecules themselves should be strong enough to allow the formation of stable islands. The interaction between molecules is usually of the van-der-Waals type and can be described with model potentials. Molecule-molecule interactions will *not* be discussed in detail in this Thesis. On the other hand, the nature of the interaction of large organic molecules with metal surfaces will be one of the central topics in this work. Three very important questions arise in this context.

1. Local adsorption site. Let us look at Fig. 1.4. There, a sketch of the metallic surface, represented by a periodically varying potential energy landscape, along with three different adsorbates is shown. Drawn on the left is a small molecule, CO, which binds via its carbon end to the metal. Since only one atom binds directly to the surface, the corrugation, that is, lateral variation of the adsorption energy, can be associated with a variation of the number of substrate atoms with which there is a direct contact (coordination number). Carbon monoxide CO usually prefers low-coordination sites, e.g., on-top bonding positions (see, for example, Fig. 3.3 in Chapter 3). Shown in the middle in Fig. 1.4 is a small adatom, for which the situation is similarly simple. Also in this case the corrugation can be rationalized by a variation of the local coordination. However, the situation is not so obvious when one considers flat-lying large aromatic molecules (on the right in Fig. 1.4). If the molecule covers several or several tens of substrate atoms, the corrugation, determined by local coordination, averages over the area of the molecule. Diffusion experiments, on the other hand, show that diffusion barriers, or the height of the corrugation potential, can be as high as 1 eV [22]. The questions that arise are: Why can the corrugation potential for flat-lying aromatic molecules be so large? Or: What determines the site-selectivity of adsorption?

Fig. 1.4 is simplified and neglects the atomic structure of the molecule itself, but clearly illustrates the problem. Experimentally, it is not an easy task to determine the exact local adsorption configuration of a large organic molecule. To date, such information is available only for few systems of interest. One elegant technique is lateral manipulation of the molecule or host atoms with an STM tip. Meyer *et al.* [23] have demonstrated this by exact determination of the C_2H_2 registry on the Cu(211) surface.

Böhringer *et al.* [24] have made use of the known adsorption site of the Ag adatom on the Ag(110) surface to determine the bonding geometry of PTCDA on Ag(110). Recently, manipulations of pentacene $C_{22}H_{12}$ on the Cu(111) surface [25] have also allowed definite conclusions to be drawn about adsorption geometry of this molecule and even to quantify the corrugation potential along high-symmetry directions. Manipulation experiments require low-temperature STM, which is not as widely accessible and widely used as room-temperature STM. In the near future, more results of this type will appear and local adsorption configurations of a larger number of molecules will be investigated.

2. Distortion of the molecule upon adsorption. The adsorption of atoms and molecules on metal surfaces leads to structural changes such as substrate relaxation and, in some cases, reconstruction. Molecules also have internal degrees of freedom, and changes in the geometries of the molecules themselves are also to be expected. For small adsorbates, like carbon monoxide, this is a well-known phenomenon. A direct proof that similar, and even more drastic, changes occur for large organic molecules, was given recently by Hauschild *et al.* [26]. A synchrotron X-ray source was used in the X-ray standing wave (XSW) experiment, a method which allows one to measure the distance of a specific atom (or a group of chemically identical atoms) from the topmost metal plane. It was shown that in the case of PTCDA on the Ag(111) surface the anhydride side groups of the molecule are closer to the substrate than the aromatic perylene core. Later, Gerlach *et al.* [27] studied the adsorption of perfluorinated copper phthalocyanine $F_{16}CuPc$ on the Cu(111) and Ag(111) surfaces and clearly showed that the peripheral fluorines are further away from the surface than the phthalocyanine center. Many more successful experiments of this kind will be performed in the near future.

3. Physical origin of site-selective adsorption. The third question to answer is: What causes the above mentioned site-selective adsorption and the change in geometry? In other words, what are the *physics* and *chemistry* of the interaction between the molecule and the surface [28]? In surface science, many useful models are known which explain the electronic structure of adsorbates on metals, e.g., the well-known Blyholder model of adsorption of carbon monoxide on metal surfaces [29, 30, 31, 32]. CO has a small number of electronic states, the most important of which are the C-derived 5σ bonding and $2\pi^*$ antibonding states. Electron spectroscopy suggests that upon adsorption there is charge donation from the metal to the $2\pi^*$ LUMO and back-donation from the 5σ HOMO to the metal. Such charge rearrangement should weaken the C=O bond. This conclusion is confirmed by vibrational spectroscopy which clearly shows that the frequency of the C=O stretch vibration decreases. Blyholder's picture of CO bonding can explain all the related phenomena - qualitative changes in the ultraviolet photoelectron spectra, softening of the C=O stretching vibration frequency and can account for a fact that adsorption is via the carbon end of the molecule. Thus, it is a very useful model. Similar models exist for other small molecules, like ethylene C_2H_4 [32] or benzene C_6H_6 [33, 34, 35]. In the latter case, for instance, the interaction of the molecule with the Pt(111) surface can be described as electron donation from the π molecular HOMO to the metal $d_{xy} + d_{yz}$ states and back-donation from the metal d_{z^2} states to the antibonding π^* molecular LUMO. As in the case of CO, many conclusions that are consistent with experiments follow from this model.

Numerous complications arise when one tries to develop such useful models for larger

organic molecules. First, big molecules have more degrees of freedom, and the adsorption energy landscape is much more complicated. Second, they possess a much larger number of electronic states and therefore more orbitals are affected by the interaction with the surface. Organic molecules used in self-assembly studies are closed-shell molecules, which interact relatively weakly with noble metal surfaces, and two questions arise: How useful is the description of the molecule-surface interactions in terms of the chemical bond; What is the relative significance of the dispersion forces [36]? These are very important questions and one can hope that such models will soon be developed for a number of interesting molecules. In Chapter 4 of this Thesis we propose such a model for 1,4,5,8-naphthalene tetracarboxylic dianhydride (NTCDA) adsorption on the Ag(110) surface. This model is based on large-scale density functional theory calculations and is able to explain a number of experimental results, such as charge transfer, local adsorption geometry, or distortion of the molecule and the substrate.

1.4 Energy level alignment

Energy level alignment is the last topic to be considered in this thesis (Chapter 5). Whether we speak about molecular electronics (Fig. 1.1) or organic electronics (Fig. 1.2), the positioning of molecular levels with respect to the Fermi energy in the metallic contacts determines the charge-carrier injection properties from the metal to the organic system (and vice versa) [37, 38, 39]. In Chapter 5 we will focus on organic films rather than single molecules. We will discuss contact properties between two bulk materials - metal and organic semiconductor. Knowledge of these properties can be useful to understand contacts between single molecules and metals, too. Another advantage of thin films versus single molecules is that numerous well-developed spectroscopic techniques, such as ultraviolet photoelectron spectroscopy (UPS), X-ray photoelectron spectroscopy (XPS) or X-ray absorption spectroscopy (XAS) can be applied to extract information about electronic structure of thin films. Those techniques cannot be used for single molecules, but rather require macroscopic samples. On the other hand, local probe methods like scanning tunneling spectroscopy (STS) can be employed to study the local electronic structure of single molecules or monolayers of molecules. Concerning the electronic structure at the interface, usually there is good agreement between the STS data and the UPS data.

Fig. 1.5 shows the two possible variants of energy level alignment at the metal-organic semiconductor interface. We use the following notations: Φ_m and E_F are the work function and Fermi energy of the metal, IP and EA are the ionization potential and electron affinity of the molecular solid, ϵ_F^v is the distance of the molecular HOMO state from the Fermi level, and ϵ_F^c is the distance of the molecular LUMO state from the Fermi level. The last two parameters are related to the hole and electron injection barriers, respectively, which can be determined in transport measurements. There is one additional parameter, however, the importance of which for the metal-organic interfaces has only realized been recently [40, 41, 42, 43, 44].

It has been known for a long time that at the interface between two solids or at the surface of a solid (in other words, at the interface between a solid and vacuum) a charge rearrangement occurs. This means, for instance, that when two solids are in contact with
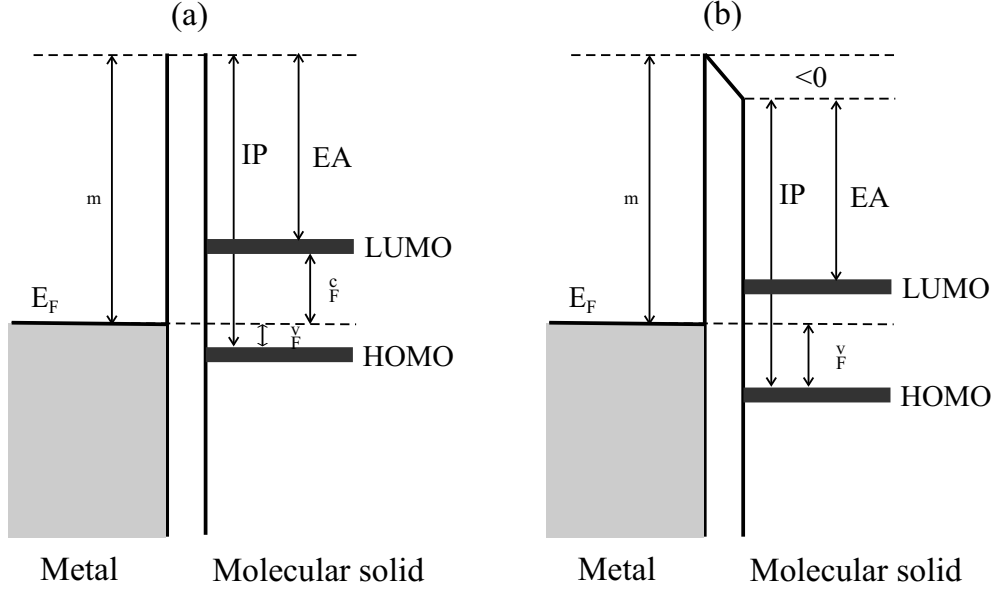
Figure 1.5: Energy level diagram at the metal-organic semiconductor interfaces: (a) without interface dipole; (b) with interface dipole. Φ_m and E_F are the work function and Fermi energy of the metal, IP and EA are the ionization potential and electron affinity of the molecular solid, ϵ_F^v is the distance of the molecular HOMO state from the Fermi level, ϵ_F^c is the distance of the molecular LUMO state from the Fermi level.

each other, the total electron charge is not just the superposition of the charges of the two subsystems. In the description of different systems this charge rearrangement has different names, for example, contact potential in the theory of metal-metal interfaces, Fermi level alignment in the theory of semiconductor p-n junctions, etc. Interface charges also control the properties of the metal - inorganic semiconductor junctions [45]. However, no charge rearrangement was previously thought to occur at metal-organic semiconductor interfaces because of weak interaction between the two solids. This means that vacuum levels of metals and organic semiconductors can be aligned when constructing the energy level diagram, as in Fig. 1.5a. It turns out that it is not the case for the majority of metal-organic interfaces [40,41,42]. There exist several physical phenomena which lead to microscopic charge rearrangement [46]. This charge rearrangement $\Delta n\,(z)$ is related to an electrostatic potential difference Δ across the interface, or a change of the work function, if we deal with thin films [47]:

$$\Delta = \frac{1}{\varepsilon_0 A_{xy}} \int_{-\infty}^{+\infty} z \Delta n\,(z)\,dz = \frac{\Delta\mu}{\varepsilon_0 A_{xy}}, \tag{1.2}$$

where $\Delta n\,(z)$ is the xy-integrated density difference, z is the coordinate perpendicular to the interface, A_{xy} is the area of the surface unit cell, and $\Delta\mu$ is the vertical interaction-induced electrostatic dipole moment per surface unit cell. The electrostatic potential difference Δ affects the position of the molecular levels with respect to the Fermi level of the metal (compare Fig. 1.5a and Fig. 1.5b), and therefore is a very important parameter.

Assuming that the IP and EA of the molecular solid do not change because of the charge transfer (even though it is different than in the isolated molecule), we have:

$$\epsilon_F^v = \text{IP} - \Phi_m - \Delta, \tag{1.3}$$

$$\epsilon_F^c = \Phi_m + \Delta - \text{EA}. \tag{1.4}$$

The ionization potential of the molecular solid, Φ_m, as well as ϵ_F^v and Δ can be measured by ultraviolet photoelectron spectroscopy, a method which is used to probe occupied states. The electron affinity of the molecular solid and hence ϵ_F^c are not accessible with this technique, but more complicated experimental methods, like inverse photo-emission spectroscopy (IPS), must be used to extract information about unoccupied states.

   Chapter 5 presents the UPS results of copper octaethylporphyrin (CuOEP, for short) on three noble metal surfaces - Ag(001), Ag(111) and Cu(111). The above-mentioned parameters, characterizing the molecule-metal interface (Fig. 1.5b) are determined. Since the field of metal-organic interfaces is quite new, an extended summary of the main physical phenomena that lead to the formation of the interface dipole in such systems is presented and critically analyzed. Different contributions to the interface dipole for the CuOEP/metal interface are then evaluated in the light of this analysis.

1.5   Outline

In this final section of the introductory chapter we summarize the Thesis:

- In **Chapter 2** we describe the theoretical basis of density functional theory, its practical implementation tools for a plane-wave basis set, and present results of test calculations (bare noble metal surfaces, for example), which are used in the following chapters.

- In **Chapter 3** a model surface science system, Cl adsorbed on the Ag(111) surface, is studied at several coverages of the adsorbate. Work function shifts and charge transfer are discussed. Classical models are applied to interpret the results.

- **Chapter 4** deals with the site-selective adsorption of a large π-conjugated organic molecule, 1,4,5,8-naphthalene tetracarboxylic dianhydride (NTCDA), on the Ag(110) surface. First, the most important experimental results are presented, and important, but yet unanswered, questions are raised. Then, large-scale density functional theory calculations are presented. The role of charge transfer and of local electrostatic interactions is discussed, and the model of site-selective adsorption is proposed.

- The central topic of **Chapter 5** is the alignment of energy levels of organic molecules to the Fermi level of the metal. First, we critically review different mechanisms that lead to the formation of an interface dipole and a deviation from the vacuum level alignment, or Schottky-Mott, rule. Then, density functional theory calculations of our system, copper-octaethylporphyrin (CuOEP), are summarized. The principles

of ultraviolet photoelectron spectroscopy (UPS) are sketched and the experimental UPS results for CuOEP on Ag(111), Ag(001) and Cu(111) are presented. This is followed by the discussion of the physical mechanisms that explain the experimental findings and evaluation of different terms that lead to a formation of the interface dipole.

- In **Chapter 6** our main results and open questions are summarized.

Bibliography

[1] A. Aviram and M.A. Ratner, *Molecular Rectifiers*, Chem. Phys. Lett. **29**, 277 (1974).

[2] M.A. Reed, C. Zhou, C.J. Muller, T.P. Burgin, and J.M. Tour, *Conductance of a molecular junction*, Science **278**, 252 (1997).

[3] A. Nitzan and M.A Ratner, *Electron transport in molecular wire junctions*, Science **300**, 1384 (2003).

[4] R.H.M. Smit, Y. Noat, C. Untiedt, N.D. Lang, M. C. van Hemert, and J.M. van Ruitenbeek, *Measurement of the conductance of a hydrogen molecule*, Nature **419**, 906 (2002).

[5] C. Stipe, M.A. Rezaei, and W. Ho, *Single-molecule vibrational spectroscopy and microscopy*, Science **280**, 1732 (1998).

[6] H. Park, J. Park, A.K.L. Lim, E.H. Anderson, A.P. Alivisatos, and P.L. McEuen, *Nanomechanical oscillation in a single-C_{60} transistor*, Nature **407**, 57 (2000).

[7] J.V. Barth, J. Weckesser, N. Lin, A. Dmitriev, and K. Kern, *Supramolecular architectures and nanostructures at metal surfaces*, Appl. Phys. A **76**, 645 (2003).

[8] J.V. Barth, G. Costantini, and K. Kern, *Engineering atomic and molecular nanostructures at surfaces*, Nature **437**, 671 (2005).

[9] N. Lorente, R. Rurali, and H. Tang, *Single-molecule manipulation and chemistry with the STM*, J. Phys.: Cond. Mat. **17**, S1049 (2005).

[10] X.-U. Zhu, *Electronic structure and electron dynamics at molecule-metal interfaces: implications for molecule-based electronics*, Surf. Sci. Rep. **56**, 1 (2004).

[11] G. Binnig, H. Rohrer, Ch. Gerber, and E. Weibel, *Surface studies by scanning tunneling microscopy*, Phys. Rev. Lett. **49**, 57 (1982)

[12] R. Wiesendanger, *Scanning probe miscroscopy and spectroscopy. Methods and applications* (Cambridge University Press, 1994).

[13] S. Datta, *Electronic transport in mesoscopic systems* (Cambridge University Press, 1995).

[14] F. Rosei, M. Shunack, Y. Naitoh, P. Jiang, A. Gourdon, E. Laegsgaard, I. Stensgaard, C. Joachim, and F. Besenbacher, *Properties of large organic molecules on metal surfaces*, Prog. Surf. Sci. **71**, 95 (2003).

[15] F. Moresco, *Manipulation of large organic molecules by low-temperature STM: model systems for molecular electronics*, Phys. Rep. **399**, 175 (2004).

[16] C. Reese, M. Roberts, M.-m. Ling, and Z. Bao, *Organic thin film transistors*, Materials Today, September, 20 (2004).

[17] F. Jensen, *Introduction to computational chemistry* (Wiley, Chichester, 1999).

[18] A. Gross, *Theoretical surface science - a microscopic perspective,* (Springer, Berlin, 2003).

[19] M. Scheffler and C. Stampfl, *Theory of Adsorption on metal surfaces*, in *Electronic Structure*, Vol. 2 of *Handbook of Surface Science*, edited by K. Horn and M. Scheffler (Elsevier, Amsterdam, 1999).

[20] R.M. Martin, *Electronic structure. Theory and practical methods* (Cambridge University Press, 2004).

[21] P.M.W. Gill, *Obituary: Density Functional Theory (1927-1993),* Aust. J. Chem. **54**, 661-662 (2001).

[22] J.V. Barth, *Transport of adsorbates at metal surfaces: from thermal migration to hot precursors*, Surf. Sci. Rep. **40**, 75 (2000).

[23] G. Meyer, S. Zophel, and K.-H. Rieder, *Scanning tunneling microscopy manipulation of native substrate atoms: a new way to obtain registry information on foreign adsorbates*, Phys. Rev. Lett. **77**, 2113 (1996).

[24] M. Böhringer, W.-D. Schneider, K. Glöckler, E. Umbach and R. Berndt, *Adsorption site determination of PTCDA on Ag(110) by manipulation of adatoms*, Surf. Sci. **419**, L95 (1998).

[25] J. Lagoute, K. Kanisawa, and S. Fölsch, *Manipulation and adsorption-site mapping of single pentacene molecules on Cu(111)*, Phys. Rev. B **70**, 245415 (2004).

[26] A. Hauschild, K. Karki, B.C.C. Cowie, M. Rohlfing, F.S. Tautz, and M. Sokolowski, *Molecular distortions and chemical bonding of a large π-conjugated molecule on a metal surface*, Phys. Rev. Lett. **94**, 036106 (2005).

[27] A. Gerlach, F. Schreiber, S. Sellner, H. Dosch, I.A. Vartanyants, B.C.C. Cowie, T.-L. Lee, and J. Zegenhagen, *Adsorption-induced distortion of $F_{16}CuPc$ on Cu(111) and Ag(111): an X-ray standing wave study*, Phys. Rev. B **71**, 205425 (2005).

[28] W.A. Harrison, *Electronic structure and the properties of solids. The physics of the chemical bond* (Dover Publications, New York, 1988).

[29] G. Blyholder, *Molecular orbital view of chemisorbed carbon monoxide*, J. Phys. Chem **68**, 2772 (1964).

[30] B. Hammer, Y. Morikawa, and J.K. Nørskov, *CO chemisorption at metal surfaces and overlayers*, Phys. Rev. Lett. **76**, 2141 (1996).

[31] A. Zangwill, *Physics at surfaces* (Cambridge University Press, 1988).

[32] R. Hoffmann, *A chemical and theoretical view to look at bonding on surfaces*, Rev. Mod. Phys. **60**, 601 (1988).

[33] C. Morin, D. Simon, and P. Sautet, *Density-functional study of the adsorption and vibration spectra of benzene molecules on Pt(111)*, J. Phys. Chem. B **107**, 2995 (2003).

[34] C. Morin, D. Simon, and P. Sautet, *Trends in the chemisorption of aromatic molecules on a Pt(111) surface: benzene, naphthalene, and anthracene from first principles calculations*, J. Phys. Chem. B **108**, 12084 (2004).

[35] C. Morin, D. Simon, and P. Sautet, *Chemisorption of benzene on Pt(111), Pd(111), and Rh(111) metal surfaces: a structural and vibrational comparison from first principles*, J. Phys. Chem. B **108**, 5653 (2004).

[36] G.P. Brivio and M.I. Trioni, *The adiabatic molecule-surface interaction: theoretical approaches*, Rev. Mod. Phys. **71**, 231 (1999).

[37] D.M. Adams *et al.*, *Charge transfer on the nanoscale: current status,* J. Phys. Chem. B **107**, 6668 (2003).

[38] Y. Xue and M.A. Ratner, *Microscopic study of transport through individual molecules with metallic contacts I. Band lineup, voltage drop, and high-field transport*, Phys. Rev. B **68**, 115406 (2003).

[39] D. Cahen, A. Kahn, and E. Umbach, *Energetics of molecular interfaces*, Materials Today, July/August, 32 (2005).

[40] S. Narioka, H. Ishii, D. Yoshimura, M. Sei, Y. Ouchi, K. Seki, S. Hasegawa, T. Miyazaki, Y. Harima, and K. Yamashita, *The electronic structure and energy level alignment of porphyrin/metal interfaces studied by ultraviolet photoelectron spectroscopy*, Appl. Phys. Lett. **67**, 1899 (1995).

[41] I.G. Hill, A. Rajagopal, A. Kahn, and Y. Hu, *Molecular level alignment at organic semiconductor-metal interfaces*, Appl. Phys. Lett. **73**, 662 (1998).

[42] H. Peisert, M. Knupfer, and J. Fink, *Energy level alignment at organic-metal interfaces: dipole and ionization potential*, Appl. Phys. Lett. **81**, 2400 (2002).

[43] X. Crispin, V. Geskin, A. Crispin, J. Cornil, R. Lazzaroni, W.R. Salaneck, and J.-L. Brédas, *Characterization of the interface dipole at organic/metal interfaces*, J. Am. Chem. Soc. **124**, 9161 (2002).

[44] M. Knupfer and H. Peisert, *Electronic properties of interfaces between model organic semiconductors and metals*, phys. stat. sol. (a) **201**, 1055 (2004).

[45] C. Tejedor, F. Flores, and E. Louis, *The metal-semiconductor interface: Si(111) and zincblende(110) junctions*, J. Phys. C: Solid State Phys. **10**, 2163 (1977).

[46] M. Knupfer and G. Paasch, *Origin of the interface dipole at the interfaces between undoped organic semiconductors and metals*, J. Vac. Sci. Technol. A **23**(4), 1072 (2005).

[47] L.D. Landau and E.M. Lifshitz, *Electrodynamics of continuous media* (Pergamon Press).

Chapter 2

Density functional theory

This chapter describes density functional theory, the main theoretical tool of this thesis. First, the founding theorems are presented. Then, the techniques that are used in the plane wave implementation of DFT are reviewed. Afterwards, test calculations are presented.

2.1 Foundations

Modern density functional theory (DFT) was born after the seminal works of P. Hohenberg, W. Kohn and L.J. Sham, in which a fundamental theorem, the Hohenberg-Kohn theorem, was proved [1] and a practical method, the Kohn-Sham method, of DFT was proposed [2]. Hohenberg and Kohn proved that if one knows the total density of the inhomogeneous interacting electron gas $n\left(\mathbf{r}\right)$, such a density can arise from one and only one (up to an additive constant) external potential $v_{ext}\left(\mathbf{r}\right)$. In the most important cases for physics and chemistry this external potential is the potential of ions (these we consider to be fixed in space) exerted on electrons. Since the Hamiltonian of the system is then uniquely defined, so is the all-electron wavefunction and as well all ground state observables, most importantly, the total energy. This means that the total energy of the system in its ground state is a function of the ground state electron density only:

$$E = E\left[n\right],\tag{2.1}$$

The functional $E\left[n\right]$ is universal. The electron density can then be found employing a variational principle, which leads to an Euler equation:

$$\frac{\delta E}{\delta n} = \mu,\tag{2.2}$$

where μ is the chemical potential, which appears in the expression because of the constraint that the number of electrons is fixed.

Kohn and Sham [2] proposed a practical way to cast the interacting electron problem

into a non-interacting one. The idea is to write the total functional in Eq. (2.1) as:

$$E[n] = \underbrace{\int v_{ext}\left(\mathbf{r}\right) n\left(\mathbf{r}\right) d\mathbf{r}}_{\text{Potential}} + \underbrace{\frac{1}{2} \int \int \frac{n\left(\mathbf{r}\right) n\left(\mathbf{r}'\right)}{\left|\mathbf{r} - \mathbf{r}'\right|} d\mathbf{r} d\mathbf{r}'}_{\text{Hartree}} + \underbrace{T_s\left[n\right]}_{\text{Kinetic}} + \underbrace{E_{XC}\left[n\right]}_{\text{XC}}. \tag{2.3}$$

Here, $T_s\left[n\right]$ is the kinetic energy of a system of *non-interacting* electrons moving under the influence of an effective potential $V_{KS}\left(\mathbf{r}\right)$, which has the same electron density as the real system of *interacting* electrons moving under the influence of the real potential $v_{ext}\left(\mathbf{r}\right)$. This fictitious system of electrons is usually called the Kohn-Sham electron system. $E_{XC}\left[n\right]$ in Eq. (2.3) is the exchange-correlation (XC) energy of the real interacting system, $\mathcal{E}_{XC}$, plus the difference of the kinetic energies of interacting and non-interacting electrons:

$$E_{XC}\left[n\right] = \mathcal{E}_{XC}\left[n\right] + T\left[n\right] - T_s\left[n\right]. \tag{2.4}$$

It can be shown then, that the ground state density (as well as the total energy and other ground state observables) can be obtained from the following self-consistent system of single-particle equations, known as the Kohn-Sham equations:

$$\left(-\frac{1}{2}\nabla^2 + V_{KS}\left(\mathbf{r}\right)\right) \psi_i\left(\mathbf{r}\right) = \epsilon_i \psi_i\left(\mathbf{r}\right), \tag{2.5}$$

$$V_{KS}\left(\mathbf{r}\right) = v_{ext}\left(\mathbf{r}\right) + \int \frac{n\left(\mathbf{r}'\right)}{\left|\mathbf{r} - \mathbf{r}'\right|} d\mathbf{r}' + \frac{\delta E_{XC}\left[n\right]}{\delta n}, \tag{2.6}$$

$$n\left(\mathbf{r}\right) = \sum_i f_i \left|\psi_i\left(\mathbf{r}\right)\right|^2. \tag{2.7}$$

f_i are the occupations of the corresponding single electron orbitals ψ_i (Kohn-Sham orbitals). In the Kohn-Sham formulation, the kinetic energy term T_s is treated exactly and the only unknown functional is the exchange-correlation functional E_{XC}, which has to be approximated. This is one of the big advantages of the Kohn-Sham method over the orbital-free DFT methods (Eq. (2.2)). It turns out that in real systems T_s constitutes a very big part of the total kinetic energy T [3], and only the difference of both, which is included in the exchange-correlation energy expression, has to be approximated. Orbital-free DFT methods suffer from a bad description of the kinetic energy part. Another useful aspect of the Kohn-Sham formulation is that single particle eigenenergies and eigenfunctions become available. They are not directly related to excitation energies or wavefunctions of excitations (quasi-particles), but nevertheless are useful. In addition, quantity like density of states, which characterizes the distribution of energy eigenvalues, is accessible within the Kohn-Sham approach. Such information is very helpful for an interpretation of numerical calculations.

2.2   Exchange-correlation functionals

In real applications the unknown density functional $E\left[n\right]$ has to be approximated. All the terms, appearing in the Kohn-Sham energy expression (2.3) are exact, except for the
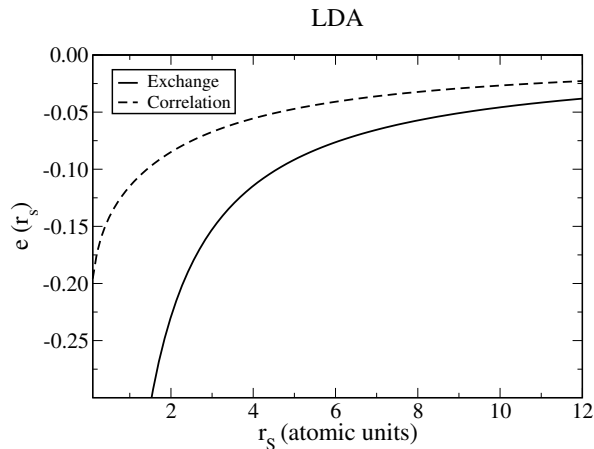
Figure 2.1: Dependence of exchange and correlation energy densities on the Wigner-Seitz radius r_s in the local density approximation.

exchange-correlation functional E_{XC}. This means that only this part has to be approximated.

The first and historically the most important approximation to the exchange-correlation functional is the local density approximation (LDA). The total energy of the system is expressed in LDA as

$$E_{XC}^{LDA}[n] = \int e_{XC}^{LDA}(n(\mathbf{r})) \, n(\mathbf{r}) \, d\mathbf{r}. \tag{2.8}$$

Here e_{XC}^{LDA} is the exchange-correlation energy density, which is a local function of the electron density. e_{XC}^{LDA} is usually split into the exchange part and the correlation part $e_{XC}^{LDA} = e_X^{LDA} + e_C^{LDA}$. It is required that in the limit of the uniform electron gas LDA should reproduce the known results for the exchange and correlation energy density. The exchange energy density of the uniform electron gas is known exactly and is given by [4]:

$$e_X^{LDA}(r_s) = -\frac{3}{4\pi} \frac{(9\pi/4)^{1/3}}{r_s}. \tag{2.9}$$

Here $r_s = (3n/4\pi)^{1/3}$ is the Wigner-Seitz radius. The analytical expression for the correlation energy density is not known. Several alternative parameterizations exist. For example, one good interpolation formula which reproduces certain known limits and quantum Monte Carlo results was proposed by Perdew and Wang [5]:

$$e_C^{LDA}(r_s) = -2c_0(1 + \alpha_1 r_s) \ln\left[1 + \frac{1}{2c_0\left(\beta_1 r_s^{1/2} + \beta_2 r_s + \beta_3 r_s^{3/2} + \beta_4 r_s^2\right)}\right], \tag{2.10}$$

parameters of which can be found in Ref. [5]. Figure 2.1 depicts the dependence of the exchange and correlation energy densities on r_s.

In many cases, especially for solid state systems, LDA performs rather well. However, it was soon realized that LDA suffers from many deficiencies [6]. In particular, the

chemical bonds of molecules are predicted to be too strong and bond lengths too short. The generalized gradient approximation, or GGA for short, generally improves upon these quantities [7]. The energy expression in GGA is:

$$E_{XC}^{GGA}[n] = \int e_{XC}^{LDA}(\mathbf{r}) f(n(\mathbf{r}),|\nabla n(\mathbf{r})|) n(\mathbf{r}) d\mathbf{r}. \tag{2.11}$$

Here $f(n(\mathbf{r}),|\nabla n(\mathbf{r})|)$ is the so-called enhancement factor which depends both on the electron density and the density gradient at the certain point $\mathbf{r}$. The functional we will be mainly using in this work is the Perdew-Burke-Ernzerhof (PBE) functional [8], named 'GGA made simple' by the authors themselves because of its analytical simplicity. This functional fulfills many exact constraints. The correlation functional in PBE is expressed as

$$E_{C}^{PBE}[n_\uparrow, n_\downarrow] = \int \left[e_{C}^{LDA}(r_s, \xi) + H(r_s, \xi, t) \right] n(\mathbf{r}) d\mathbf{r}, \tag{2.12}$$

and the exchange functional as

$$E_{X}^{PBE}[n] = \int e_{X}^{LDA}(r_s) F_X(r_s, s) n(\mathbf{r}) d\mathbf{r}. \tag{2.13}$$

In the expressions (2.12) and (2.13) two dimensionless gradients were used:

$$s = \frac{|\nabla n|}{2k_F n} = \frac{3}{2} \left(\frac{4}{9\pi} \right)^{1/3} |\nabla r_s| \tag{2.14}$$

and

$$t = \frac{|\nabla n|}{2k_S n} = \left(\frac{\pi}{4} \right)^{1/2} \left(\frac{4}{9\pi} \right)^{1/3} \frac{s}{r_s^{1/2}}. \tag{2.15}$$

The first one is more convenient to describe exchange, the second is more convenient to describe the dependence of the correlation energy density on electron density gradient. Above, k_F and k_S are the Fermi wavevector and the inverse of the Thomas-Fermi screening length of an electron gas with density n. The quantity ξ, appearing in Eq. (2.9), is spin polarization:

$$\xi = \frac{n_\uparrow - n_\downarrow}{n_\uparrow + n_\downarrow}. \tag{2.16}$$

We will deal with spin-unpolarized systems is our work, which means $\xi = 0$.

The performance of PBE for the systems of our interest is addressed at the end of this chapter, where the test calculations will be presented.

2.3   Technical details

2.3.1   Plane waves

To solve the Kohn-Sham equations one can employ different basis sets. Plane waves is the most popular choice in solid state physics [9]. We will deal with metallic systems in

this thesis, for which iterative diagonalization methods rather than minimization methods are used to find the ground state density and the total energy of the system. Therefore we will need the expression of the Kohn-Sham Hamiltonian in the plane-wave basis set. This section describes how different terms of the Hamiltonian are calculated in the actual computation. For the n-th eigenfunction ψ_n at some specific k-point (see below for a description of these) the Kohn-Sham equation reads (we will assume here that the Kohn-Sham potential is local):

$$\hat{H}_{KS}(\mathbf{r})\psi_n(\mathbf{r}) = \left(-\frac{1}{2}\nabla^2 + V_{KS}(\mathbf{r})\right)\psi_n(\mathbf{r}) = \epsilon_n\psi_n(\mathbf{r}). \tag{2.17}$$

The Kohn-Sham potential can be written as Fourier series:

$$V_{KS}(\mathbf{r}) = \sum_{\mathbf{G}} V_{KS}(\mathbf{G})e^{i\mathbf{Gr}}, \tag{2.18}$$

and $\mathbf{G}$ runs over the vectors of the reciprocal lattice. A normalized single electron wave function at the certain k-point can be expressed in the Bloch form

$$\psi_{n,\mathbf{k}} = \frac{1}{\sqrt{\Omega}}e^{i\mathbf{kr}}\chi_n(\mathbf{r}) = \frac{1}{\sqrt{\Omega}}e^{i\mathbf{kr}}\sum_{\mathbf{G}} c_n(\mathbf{G})e^{i\mathbf{Gr}}, \tag{2.19}$$

where the periodic function χ_n was expanded in the plane-wave basis set, and Ω is the volume of the unit cell. Substituting the wave function expression from (2.19) into (2.17) we get:

$$\frac{1}{\sqrt{\Omega}}\sum_{\mathbf{G}}\left(-\frac{1}{2}\nabla^2 + V_{KS}(\mathbf{r})\right)c_n(\mathbf{G})e^{i(\mathbf{k}+\mathbf{G})\mathbf{r}} = \frac{1}{\sqrt{\Omega}}\epsilon_n\sum_{\mathbf{G}} c_n(\mathbf{G})e^{i(\mathbf{k}+\mathbf{G})\mathbf{r}}. \tag{2.20}$$

Multiplying the last equation by $e^{-i(\mathbf{k}+\mathbf{G}')\mathbf{r}}/\sqrt{\Omega}$ and integrating over the unit cell we arrive at:

$$\sum_{\mathbf{G}} \underbrace{\left(\frac{1}{2}(\mathbf{k}+\mathbf{G})^2\delta_{\mathbf{G},\mathbf{G}'} + V_{KS}(\mathbf{G}-\mathbf{G}')\right)}_{H_{KS}(\mathbf{G},\mathbf{G}')} c_n(\mathbf{G}) = \epsilon_n c_n(\mathbf{G}'). \tag{2.21}$$

Here $H_{KS}(\mathbf{G},\mathbf{G}')$ is the expression of the Kohn-Sham Hamiltonian in the plane wave representation:

$$H_{KS}(\mathbf{G},\mathbf{G}') = \frac{1}{2}|\mathbf{k}+\mathbf{G}|^2\delta_{\mathbf{G},\mathbf{G}'} + V_{KS}(\mathbf{G}-\mathbf{G}'). \tag{2.22}$$

We see that the kinetic energy part is diagonal in $\mathbf{G}$ and the potential energy part has a very simple form. Now we briefly discuss how the Fourier transform of the Kohn-Sham potential is calculated.

The total Kohn-Sham potential, appearing in Eq. (2.17) is a sum of the ionic, Hartree and the exchange-correlation contributions:

$$V_{KS}(\mathbf{G}) = V_{ion}(\mathbf{G}) + V_{Hartree}(\mathbf{G}) + V_{XC}(\mathbf{G}). \tag{2.23}$$

The first term, $V_{ion}(\mathbf{G})$, is the Fourier transform of the ionic potential, which in real space can be written as

$$V_{ion}(\mathbf{r}) = \sum_{\mu=1}^{\mathcal{N}_{species}} \sum_{j=1}^{\mathcal{N}_{\mu}} \sum_{\mathbf{T}} V^{\mu}(\mathbf{r} - \mathbf{R}_{\mu,j} - \mathbf{T}), \qquad (2.24)$$

where the sum is over different atom species μ ($\mu = 1...\mathcal{N}_{species}$), all the atoms of each species j ($j = 1...\mathcal{N}_{\mu}$) and all the periodic images described by the translation vectors $\mathbf{T}$. $\mathbf{R}_{\mu,j}$ in Eq. (2.24) is the position of the j-th atom of the type μ. It may seem that the calculation of $V_{ion}(\mathbf{G})$ is expensive, since the ionic potential depends on the position of atoms, and, therefore, its Fourier transform has to be recalculated for each different position of the atoms (during the geometry optimization, for instance). However, it turns out, that the Fourier transform of $V_{ion}(\mathbf{r})$ can be written as:

$$V_{ion}(\mathbf{G}) = \frac{1}{\Omega} \int_{\Omega} V_{ion}(\mathbf{r}) e^{-i\mathbf{G}\mathbf{r}} d\mathbf{r} = \sum_{\mu=1}^{\mathcal{N}_{species}} S^{\mu}(\mathbf{G}) V^{\mu}(\mathbf{G}). \qquad (2.25)$$

$S^{\mu}(\mathbf{G})$ is the structure-factor for the μ-th species of atoms and contains all the information about the coordinates of all the atoms:

$$S^{\mu}(\mathbf{G}) = \sum_{j=1}^{\mathcal{N}_{\mu}} e^{-i\mathbf{G}\mathbf{R}_{\mu,j}}, \qquad (2.26)$$

and $V^{\mu}(\mathbf{G})$ is the form factor, which characterizes each ionic potential of the type μ:

$$V^{\mu}(\mathbf{G}) = \int_{\text{all space}} \mathbf{V}^{\mu}(\mathbf{r}) e^{-i\mathbf{G}\mathbf{r}} d\mathbf{r}. \qquad (2.27)$$

In the last equation, integration is carried over all space. Ionic potentials (or pseudopotentials, as they are called) behave like $-Z_{\mu}/r$ at large distances (see Fig. 2.4), where Z_{μ} is the core charge (11 for silver and copper, for instance). To remove divergences, a long range part is subtracted from the ionic potential by the following procedure. Let us put a negative charge with a Gaussian charge distribution at the position of each ion:

$$n_{core}^{\mu}(\mathbf{r}) = -\frac{Z_{\mu}}{\pi^{3/2}(R_{\mu})^3} \exp\left[-\left(\frac{r}{R_{\mu}}\right)^2\right], \qquad (2.28)$$

and R_{μ} characterizes the decay of the Gaussian charge distribution. This negative charge creates an electrostatic potential

$$V_{core}^{\mu}(\mathbf{r}) = +\frac{Z_{\mu}}{r} \text{Erfc}\left[\frac{r}{R_{\mu}}\right], \qquad (2.29)$$

(Erfc being the complementary error function) which is added to the ionic pseudopotential to produce a short-ranged potential:

$$U^{\mu}(\mathbf{r}) = V^{\mu}(\mathbf{r}) + V_{core}^{\mu}(\mathbf{r}). \qquad (2.30)$$

1. FFT to real space
$\psi_{n,\mathbf{k}}(\mathbf{r}) = \text{FFT}[\psi_{n,\mathbf{k}}(\mathbf{G})]$
$\downarrow$

2. Partial densities
$n_{n,\mathbf{k}}(r) = |\psi_{n,\mathbf{k}}(\mathbf{r})|^2$
$\downarrow$

3. Sum over states and k-points
$n(\mathbf{r}) = \sum_{\mathbf{k}} w_{\mathbf{k}} \sum_n f(\epsilon_{n,\mathbf{k}}) n_{n,\mathbf{k}}(r)$
$\downarrow$

4. Inv. FFT to reciprocal space
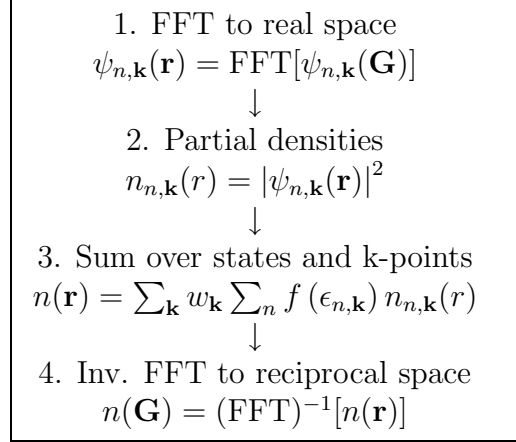$n(\mathbf{G}) = (\text{FFT})^{-1}[n(\mathbf{r})]$

Figure 2.2: Flow chart of the electron density calculation using plane wave basis set.

The compensating positive charge having the same Gaussian distribution around each atom is added to the total electron charge. Thus, the total charge of the system, used to calculate the Hartree potential, is

$$n_{tot}(\mathbf{r}) = n(\mathbf{r}) - \sum_{\mu=1}^{\mathcal{N}_{species}} \sum_{j=1}^{\mathcal{N}_\mu} n_{core}^\mu (\mathbf{r} - \mathbf{R}_{\mu,j}). \tag{2.31}$$

So-defined n_{tot} integrates to 0. The Poisson equation is easily solved with periodic boundary conditions, and the Fourier transform of the Hartree potential is given by:

$$V_{Hartree}(\mathbf{G}) = \frac{4\pi}{G^2} n_{tot}(\mathbf{G}). \tag{2.32}$$

The term $n_{tot}(0)$ is the total charge of the system, which by construction is zero, and thus the term $V_{Hartree}(0)$ is no longer infinite. While evaluating the total energy, the above procedure (which is called the Ewald summation), which introduces negative auxiliary charge for the calculation of V_{ion} and positive additional charge in the calculation of $V_{Hartree}$, gives an additional term, which reflects a self-interaction energy of a positive charge background. It has, however, a simple expression (which depends on R_μ only) and is easily evaluated.

The exchange-correlation potential V_{XC} is calculated by simply Fourier transforming the exchange-correlation potential in real space:

$$V_{XC}(\mathbf{G}) = (\text{FFT})^{-1}[V_{XC}(n(\mathbf{r}))]. \tag{2.33}$$

We have seen that calculating various terms the expressions of the electron density both in real space (as in Eq. (2.33)) and reciprocal space (as in Eq. (2.32)) is needed. The flow-chart of calculating both $n(\mathbf{G})$ and $n(\mathbf{r})$ from Kohn-Sham wavefunction $\psi_{\mathbf{k},n}(\mathbf{r})$ is shown in Fig. 2.2.

2.3.2   Pseudopotentials

The low energy physics and chemistry of molecules and solids are governed by the be-
haviour of chemically active valence electrons. One frequently finds that the remaining
strongly-bound core electrons are almost unaffected by small changes in the valence re-
gion. Thus in the majority of cases it is reasonable to keep the core degrees of freedom
frozen (frozen core approximation). However, the core electrons are still present in such a
formulation since valence wave functions should be always orthogonal to core wave func-
tions. When using plane waves for the expansion of Kohn-Sham orbitals, this causes a
problem. For elements heavier than H and He, the valence wavefunctions have nodal
planes and therefore one needs a very large plane wave basis set for an expansion of such
rapidly oscillating functions. For heavy elements the computational problem becomes in-
tractable. Fortunately it turns out, that it is possible to get rid of the explicit treatment
of core states by replacing the core potential by a smooth pseudopotential, for which va-
lence pseudo-wavefunctions are *nodeless* and *smooth* eigenstates. A good transferability
to other chemical environments is achieved by the so-called norm conservation condi-
tion [10], which requires that the norms of the pseudo wavefunction and the all-electron
wavefunction of an atom are equal beyond a certain chosen core radius r_c:

$$\int_0^{r'} \psi^{AE} r^2 dr = \int_0^{r'} \psi^{ps} r^2 dr, \ r > r_c.$$

Norm conservation guarantees that logarithmic derivatives of the all-electron wave func-
tion and the pseudo wavefunction agree at the reference energy (atomic eigenvalue):

$$\frac{d}{d\epsilon} \left\{ \frac{d}{dr} \ln \psi^{AE}(\epsilon, r) \right\} \Bigg|_{\substack{r = r^c \\ \epsilon = \epsilon'}} = \frac{d}{d\epsilon} \left\{ \frac{d}{dr} \ln \psi^{ps}(\epsilon, r) \right\} \Bigg|_{\substack{r = r^c \\ \epsilon = \epsilon'}}.$$

To generate norm-conserving pseudopotentials, one needs these steps:

  a) *Atomic all-electron calculation.* All-electron Kohn-Sham orbitals $u_{nl}(\epsilon_{nl}; r)$ and
eigenvalues ϵ_{nl} are obtained by solving the scalar-relativistic radial Schrödinger equation:

$$\left[\frac{1}{2M(r)} \left(-\frac{d^2}{dr^2} - \frac{1}{2M(r)c^2} \frac{dV(r)}{dr} r \frac{d}{dr} \frac{1}{r} + \frac{l(l+1)}{r^2} \right) + V(r) - \epsilon_{nl} \right] u_{nl}(\epsilon_{nl}; r) = 0,$$

where $M(r) = 1 + (\epsilon_{nl} - V(r))/2c^2$. It is necessary to include the relativistic terms for
heavier elements, noble metals, for instance.

  b) *Construction of pseudo-valence orbitals.* Nodeless and smooth atomic pseudo-
orbitals are then constructed by a suitable procedure (Hamann scheme [10], Troullier-
Martins scheme [11], etc.), ensuring that norm-conservation condition is fulfilled. Smooth-
ness of the pseudo-orbitals is achieved by additional procedure-dependent requirements
(see below for the Troullier-Martins scheme).

  c) *Obtaining screened pseudopotentials.* Atomic pseudo-orbitals are solutions to the
non-relativistic Schrödinger equation with an l-dependent potential $U_l^{ps}(r)$:

$$\left[-\frac{1}{2} \frac{d^2}{dr^2} + \frac{l(l+1)}{2r^2} + U_l^{ps}(r) - \epsilon_l^{ps}(r) \right] u_l^{ps}(\epsilon_l^{ps}; r) = 0.$$

This potential $U_l^{ps}(r)$, which is called screened pseudopotential, is obtained by a simple inversion of the Schrödinger equation:

$$U_l^{ps}(r) = \epsilon_l^{ps} - \frac{l(l+1)}{2r^2} + \frac{1}{2u_l^{ps}(\epsilon_l^{ps};r)} \frac{d^2}{dr^2} u_l^{ps}(\epsilon_l^{ps};r)$$

(u_l^{ps} are known from the construction procedure - step b).

d) *Obtaining ionic pseudopotential.* Ionic pseudopotentials are obtained by an unscreening procedure. The Hartree and exchange-correlation potentials of the valence pseudo-electrons are subtracted from the screened pseudopotential $U_l^{ps}(r)$ to obtain a transferable ionic pseudopotential $V_{ion}^l(r)$. These ionic pseudopotentials are different for different components of the angular momentum, and thus in practice they are used as semi-local potentials:

$$\hat{V}^{ps}(r) = V^{loc}(r) + \sum_{l=0}^{l_{max}} \sum_{m=-l}^{l} |Y_{lm}\rangle \Delta V_l^{ps}(r) \langle Y_{lm}|. \tag{2.34}$$

$V^{loc}(r)$ is the local part of the pseudopotential, and $\Delta V_l^{ps}(r)$ are the non-local components. In plane wave implementation, the semilocal form is quite expensive, and therefore a much more convenient non-local form of Kleinman and Bylander [12] is used instead:

$$\hat{V}^{ps} = V^{loc}(r) + \sum_{l=0}^{l_{max}} \sum_{m=-l}^{l} |u_{lm}^{ps}\rangle E_l^{KB} \langle u_{lm}^{ps}|. \tag{2.35}$$

Here, $u_{lm}^{ps}(\mathbf{r}) = u_{lm}^{ps}(r)Y(\theta,\phi)$. Sometimes additional problems arise when using this non-local form, for example, the appearance of the ghost states [13, 14], but we will mention these problems when dealing with a a particular system. Below we describe the construction of pseudo-orbitals in the Troullier-Martins scheme.

Troullier-Martins scheme [11]. The pseudo-orbitals in the Troullier-Martins scheme have the following form:

$$u_l^{ps}(r) = \begin{cases} u_l^{AE}(r), & r > r_{cl} \\ r^l \exp[p(r)], & r < r_{cl} \end{cases} \tag{2.36}$$

where $p(r)$ is a sixth-order polynomial in r^2 : $p(r) = c_0 + c_2 r^2 + c_4 r^4 + c_6 r^6 + c_8 r^6 + c_{10}r^{10} + c_{12}r^{12}$. The seven coefficients in this expansion are determined by imposing seven conditions: (i) Norm conservation of charge within the core region. This condition is common to all norm-conserving pseudopotentials. (ii)-(vi) The continuity of pseudo-wavefunction and its first four derivatives at the core radius r_c. While the first condition is general for all norm-conserving pseudopotentials, the last are specific to Troullier-Martins PPs and ensure the continuity of the first two derivatives of the screened pseudopotential. (vii) Zero curvature of the screened pseudopotential at the origin, i.e. $(U_l^{ps})''_{r_c} = 0$.

The advantage of the Troullier-Martins scheme is that the resulting equations for the coefficients c_i are quite simple (linear for conditions (ii)-(vi), for instance), and condition (vii) guarantees the smoothness of the resulting pseudopotential. In Fig. 2.3 all-electron and Troullier-Martins pseudo-orbitals are plotted for silver and copper. The corresponding
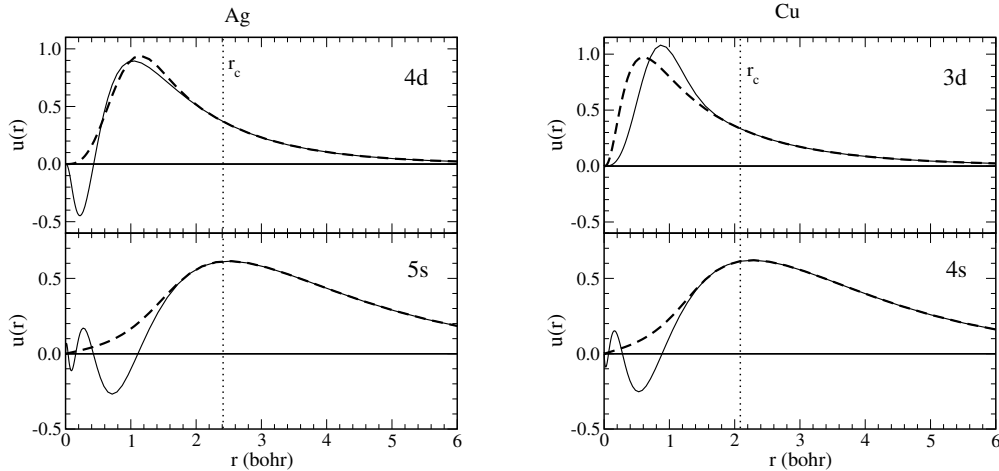
Figure 2.3: All electron wave functions (solid lines) and pseudo wave functions (dashed lines) for Ag (left) and Cu (right). The core radii ($r_c = 2.19$Å for Ag and $r_c = 2.01$Å for Cu) are shown by a vertical dashed line.

ionic pseudopotentials are shown in Fig. 2.4. At large distances, the pseudopotentials have an asymptotic $-Z/r$ behaviour, as discussed above ($Z = 11$ for Ag and Cu). The Troullier-Martins pseudopotentials shown in Fig. 2.4 were generated using a well tested fhi98PP program package from Fritz Haber Institut, Berlin [15] and were used for all the calculations involving these metals in this Thesis. Fig. 2.3 also tells us that the resulting 3d pseudo-orbital for copper is no smoother than the original AE orbital. The consequence of this is that a rather large plane wave kinetic energy cutoff is needed to converge the total energy of the systems which include copper atoms (see below for the convergence tests). It is important to stress that Troullier-Martins pseudopotentials are numeric pseudopotentials. Since the pseudo-orbital in the core region is written in a simple analytical form and matches the numerical AE wavefunction at the core radius, the inversion of the Schrödinger equation and the unscreening procedure produces a numeric pseudopotential.

   Convergence tests. Once a pseudopotential is generated, it is important to test it for known systems. Calculations of isolated atoms and bulk materials can give an indication of the kinetic energy cutoff needed to converge the total energy. Two plots in Fig. 2.5 show the dependence of the total energy of bulk fcc silver (left) and copper (right) on the kinetic energy cutoff using the above generated PPs. 50Ry cutoff is needed to converge the total energy of bulk silver, while as high as a 80Ry cutoff is needed for bulk copper. For isolated atoms and surfaces of silver and copper total energies are converged using the same cutoffs.

2.3.3   Brillouin zone integration

In DFT calculations of periodic solids one often has to carry out integrations over the Brillouin zone (BZ). The most important example is the determination of the total electron
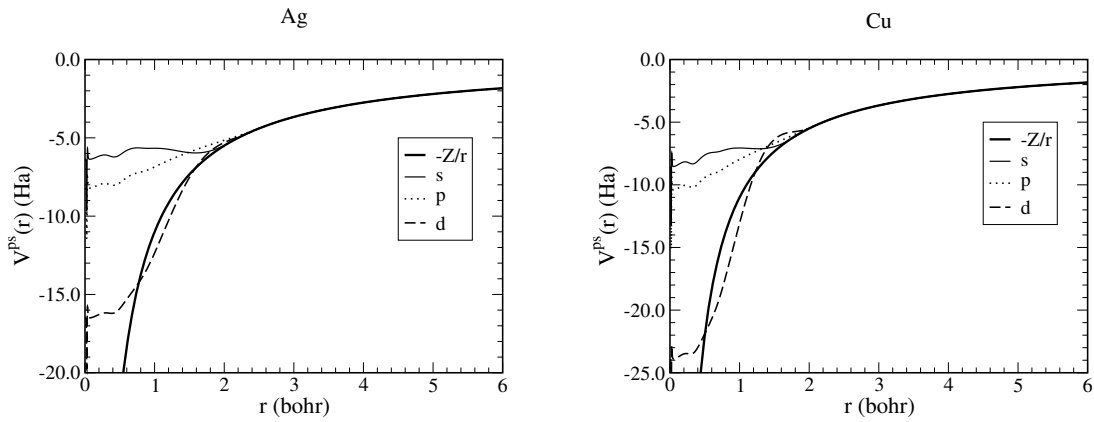
Figure 2.4: Troullier-Martins pseudopotentials for Ag (left) and Cu (right). Note that the Cu d-component is much more attractive than that of silver.
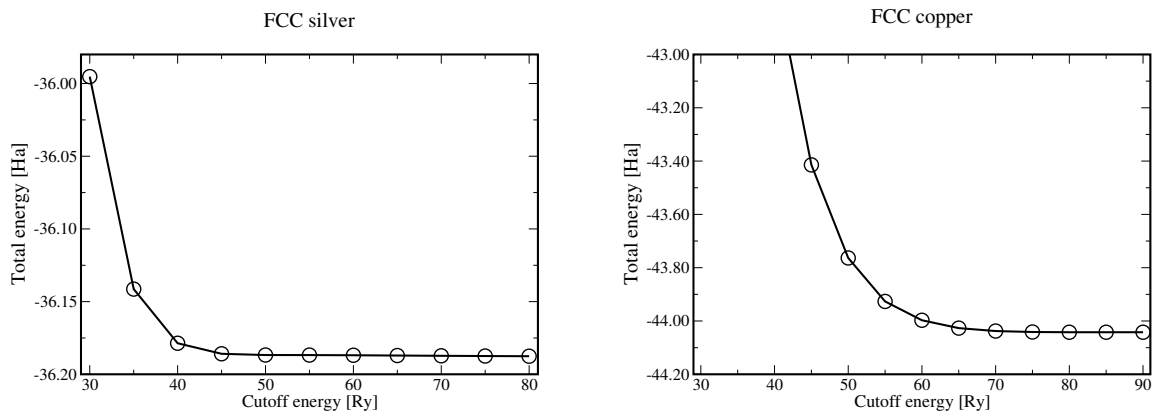

Figure 2.5: Total energy of fcc bulk Ag (left) and fcc bulk Cu (right) as a function of the plane-wave kinetic energy cutoff. Total energy of Ag is converged at 50Ry, whereas 80Ry are needed for Cu.

density of the solid, as in Fig. 2.2, step 3. Let $g(\mathbf{k})$ be the integrated function. In practice, the integration is replaced by a summation over the discrete set of points in the BZ, so-called k-points:

$$\frac{1}{(2\pi)^3} \int_{\text{BZ}} g(\mathbf{k}) \, d\mathbf{k} = \frac{1}{N\Omega} \sum_{i=1}^{N} g(\mathbf{k}_i). \tag{2.37}$$

Often because of some special symmetry this sum can be carried only over symmetry-inequivalent k-points, or special k-points:

$$\frac{1}{N\Omega} \sum_{i=1}^{N} g(\mathbf{k}_i) = \frac{1}{\Omega} \sum_{\mathbf{k}} w_{\mathbf{k}} g(\mathbf{k}), \tag{2.38}$$

$w_{\mathbf{k}}$ being the weight of the special k-points. All weights must add up to 1:

$$\sum_{\mathbf{k}} w_{\mathbf{k}} = 1.$$

In metals the occupation numbers of bands which cross the Fermi level are discontinuous as a function of the wavevector $\mathbf{k}$, and k-point integration converges extremely slow. One way out of this problem is to use the finite temperature smearing techniques [16]. Here, the occupations of bands are not discontinuous but are rather governed by the finite temperature Fermi-Dirac distribution:

$$f(\epsilon_{n,\mathbf{k}}) = \frac{1}{1 + e^{((\epsilon_{n,\mathbf{k}} - \mu)/T)}}. \tag{2.39}$$

It turns out, however, that the total energy is no longer a variational functional, that means that the ground state density is no longer the density which minimizes $E[n]$. To obtain a variational functional, the total energy must be replaced by the generalized free energy:

$$F[n] = E[n] - T \sum_{n} S(f_n), \tag{2.40}$$

T being the temperature, f_n being the occupation numbers from Eq. (2.39), and $S(f_n)$ being an entropy term, which in the case of the Fermi-Dirac distribution is:

$$S(f_n) = -f_n \ln f_n + (1 - f_n) \ln (1 - f_n). \tag{2.41}$$

The ground state density is the one which minimizes $F[n]$. As long as the temperature T is small, the ground state density is almost equal to the real density, which minimizes $E[n]$ when $T = 0$. It should be emphasized that temperature smearing technique is just a method to speed up the convergence of the k-point summation for metallic systems, and therefore temperature T does not have to be 'real' temperature. In practice, temperatures much higher than experimentally meaningful temperatures are used. A very important point to stress is that free energy and total energy themselves depend on temperature much more than electron density. For a metallic systems, the low-temperature behaviour of the free energy is [16, 17]:
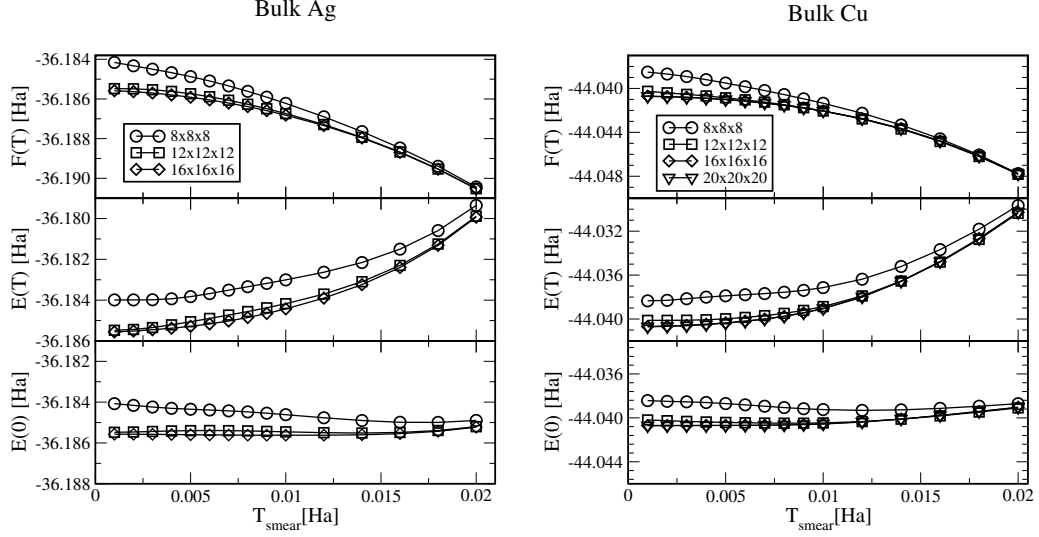
Figure 2.6: Dependence of the free energy (top plot), total energy (middle plot) and extrapolated zero-temperature total energy (bottom plot) for bulk fcc silver and bulk fcc copper as a function of Fermi smearing temperature for different Monkhorst-Pack k-point meshes: $8 \times 8 \times 8$ (open circles), $12 \times 12 \times 12$ (open squares), $16 \times 16 \times 16$ (open diamonds), and $20 \times 20 \times 20$ (open triangles).

$$F(T) = E(0) + \gamma T^2 + \mathcal{O}(T^4), \tag{2.42}$$

$E(0)$ being the total energy at zero temperature, which is the relevant quantity to find. The behaviour of the total energy is:

$$E(T) = E(0) - \gamma T^2 + \mathcal{O}(T^4). \tag{2.43}$$

In Eqs. (2.42) and (2.43) the coefficient γ in front of the quadratic term is the same. Neglecting the fourth order terms, we can find the extrapolated value $E(0)$:

$$E(0) = \frac{1}{2}(E(T) + F(T)). \tag{2.44}$$

In Fig. 2.6 the plots illustrating these concepts are shown. Bulk silver and copper calculations are performed for different k-point meshes ($8 \times 8 \times 8$, $12 \times 12 \times 12$, $16 \times 16 \times 16$ and (for copper) $20 \times 20 \times 20$), as well as different smearing temperatures T. As in Eqs. (2.42) and (2.43), free energy and total energy are quadratic functions of temperature (Fig. 2.6, top panel and middle panel). However, $E(0)$, extrapolated from Eq. (2.44), is almost independent on temperature (bottom panel). Fig. 2.6 lets us to conclude that $T = 0.01$Ha and k-point mesh $16 \times 16 \times 16$ is optimal for bulk Ag and Cu. We have used the same T and similarly dense k-point meshes also for surface calculations. At the end of this section, we describe one special recipe to generate special k-points.

Monkhorst-Pack scheme [18]. Given the mesh size $N_1 \times N_2 \times N_3$ and the set of reciprocal lattice vectors $\{\mathbf{G}_1, \mathbf{G}_2, \mathbf{G}_3\}$ the Monkhorst-Pack k-point mesh is defined via the equation:
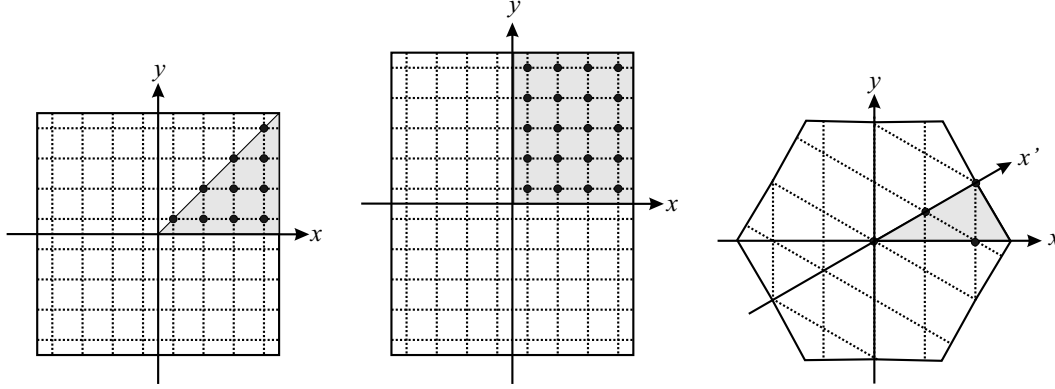
Figure 2.7: Special k-points for the square (left), rectangular (center) and triangular (right) 2D lattices. The irreducible wedges of the Brillouin zones are shaded. Monkhorst-Pack meshes 8×8, 8×10 and 5×5 produce 10, 20 and 4 special k-points, respectively.

$$\mathbf{k}_{n_1 n_2 n_3} = \sum_{i=1}^{3} \frac{2n_i - N_i - 1}{2N_i} \mathbf{G}_i, \tag{2.45}$$

$n_i = 1...N_i$. It is a set of uniformly spaced grid points in the direction of each $\mathbf{G}_i$. Figure 2.7 shows the Brilloun zones for the square, rectangular and triangular lattices and Monkhorst-Pack meshes 8×8, 8×10 and 5×5 (as an example), respectively. The irreducible wedges, that means, symmetry-inequivalent parts, of the BZs are shaded, and the special k-points are marked by small filled circles. The above meshes produce 10, 20 and 4 symmetry-inequivalent k-points.

2.3.4 Iterative diagonalization and charge density mixing

There are two ways to determine the ground state density and the total energy of the given system. One method is that of direct minimization of the total energy functional and was pioneered by Car and Parrinello [19]. This approach employs standard minimization techniques, like damped molecular dynamics or conjugate gradients, for the electronic degrees of freedom. In principle, this is a constrained minimization problem where occupied Kohn-Sham orbitals should remain orthogonal. A second method, which is more suited for metallic systems and systems with a small band gap, is that of diagonalization and charge density mixing. Here, at the i-th self-consistent field iteration one starts from some total electron density n_{in}^i, constructs the Kohn-Sham Hamiltonian and then finds lowest eigenstates of the Hamiltonian ψ_j^i, which produce a new electron density n_{out}^i. A subtle combination of n_{in}^i and n_{out}^i (and sometimes densities from previous iterations) is used to construct electron density $n_{in}^{(i+1)}$ for the next self consistent field (SCF) iteration. Many alternative algorithms for both of these two basic steps exist.

Diagonalization. Once the Hamiltonian is constructed, one has to solve the single particle Schrödinger equation

$$\hat{H}_{KS} |\psi_j\rangle = \epsilon_j |\psi_j\rangle \tag{2.46}$$

for the Kohn-Sham orbitals ψ_j. The ordinary diagonalization techniques scale like N_{plw}^3 (N_{plw} is the size of plane wave basis set), and for large systems such a problem is intractable. One needs however only much smaller number of orbitals N_b - all of the occupied ones and (for metallic systems) also lowest unoccupied ones. Usually $N_b \ll N_{plw}$ and therefore full diagonalization, which determines *all* the orbitals, is a waste. Instead, iterative diagonalization methods can be used [20]. Iterative algorithms construct an expansion set $\{|\phi_l\rangle, \; l = 1...N_a\}$ from which new orbitals are determined by diagonalizing the Kohn-Sham Hamiltonian in the expansion set (sub-space diagonalization). Since $N_a \ll N_{plw}$, the computational cost of such schemes is smaller for large systems if the cost of constructing the sub-space Hamiltonian is still small enough. Let us describe one of the methods to generate expansion set and introduce the notions of residual vectors, error vectors and preconditioning matrices.

Let $|\psi_j\rangle$ be the exact (yet unknown) wavefunctions for a given (and fixed) Kohn-Sham potential, and ϵ_j the exact (also unknown) eigenenergies. At the current iteration let $\left|\tilde{\psi}_j\right\rangle$ be an approximation to the wavefunction. A very important quantity is the Rayleigh quotient:

$$\tilde{\epsilon}_j = \left\langle \tilde{\psi}_j \middle| \hat{H}_{KS} \middle| \tilde{\psi}_j \right\rangle \tag{2.47}$$

(we restrict ourselves to normalized wavefunctions). The residual vector $|R_j\rangle$ is defined as

$$|R_j\rangle = \left(\hat{H}_{KS} - \tilde{\epsilon}_j \right) \left|\tilde{\psi}_j\right\rangle. \tag{2.48}$$

By definition we have:

$$|0\rangle = \left(\hat{H}_{KS} - \epsilon_j \right) |\psi_j\rangle = \left(\hat{H}_{KS} - \tilde{\epsilon}_j \right) |\psi_j\rangle + (\tilde{\epsilon}_j - \epsilon_j) |\psi_j\rangle. \tag{2.49}$$

Subtracting Eq. (2.49) from Eq. (2.48) we obtain:

$$\left(\hat{H}_{KS} - \tilde{\epsilon}_j \right) \underbrace{\left(|\psi_j\rangle - \left|\tilde{\psi}_j\right\rangle \right)}_{|\delta\psi_j\rangle} + (\tilde{\epsilon}_j - \epsilon_j) |\psi_j\rangle = -|R_j\rangle. \tag{2.50}$$

The eigenvalues, being quadratic functions of orbitals, converge much faster than the orbitals themselves, therefore one can discard the second term in (2.50) and obtain an estimate of the error vector:

$$|\delta\psi_j\rangle = |\psi_j\rangle - \left|\tilde{\psi}_j\right\rangle \approx -\frac{1}{\hat{H}_{KS} - \tilde{\epsilon}_j} |R_j\rangle. \tag{2.51}$$

All the terms in Eq. (2.51) are known, but the inversion of $\hat{H}_{KS} - \tilde{\epsilon}_j$ is no easier than the full diagonalization of $\hat{H}_{KS}$ itself. For plane waves, the asymptotic behaviour of the Kohn-Sham Hamiltonian for large $\mathbf{G}$'s is known, because it is dominated by the kinetic energy term (see Eq. (2.21)). Based on that, one can approximate the inverse $-\left(\hat{H}_{KS} - \tilde{\epsilon}_j \right)$ by another matrix, called the preconditioning matrix $\hat{K}$ (or simply precoditiner). The error vector is then given:

$$|\delta\psi_j\rangle = \hat{K} |R_j\rangle. \tag{2.52}$$

Different iterative diagonalization schemes differ by different expansion sets used. The expansion set in the blocked Davidson scheme consists of the error vectors $\{|\delta\psi_j\rangle,\ j = 1\ldots N_b\}$ together with the approximate eigenvectors $\left\{\left|\tilde{\psi}_j\right\rangle,\ j = 1\ldots N_b\right\}$ (sometimes also error vectors from previous iterations are used). The dimension of the expansion set N_a is thus equal to $2N_b$ and the Hamiltonian is diagonalized in the $2N_b \times 2N_b$ sub-space to yield new approximate orbitals $\left|\tilde{\psi}_j\right\rangle$. Usually, only several iterations of diagonalization are needed, because when far from self-consistency, accurate determination of wavefunctions for an approximate potential is a waste. Convergence criteria can become stricter when approaching to self-consistency.

Charge density mixing. When new wavefunctions are determined for a given potential, they yield the new density

$$n_{out} = \sum_j f_j \left|\psi_j\right|^2 \tag{2.53}$$

(f_j are occupation numbers of orbitals, as before). The output wavefunctions are functionals of the input density, and also therefore the output density is a functional of the input density:

$$n_{\text{out}} = n_{\text{out}}\left[n_{\text{in}}\right]. \tag{2.54}$$

The residual density is defined as the difference between output and input densities

$$R\left[n_{\text{in}}\right] = n_{\text{out}}\left[n_{\text{in}}\right] - n_{\text{in}}. \tag{2.55}$$

Simple mixing schemes add a fraction of the residual density to the old density to obtain the new input density:

$$n_{\text{in}}^{i+1} = n_{\text{in}}^i + \alpha R\left[n_{\text{in}}^i\right]. $$

More elaborate schemes, like Pulay mixing, use in addition the information from previous iterations and seek the new density as the linear combination of previous densities (starting from iteration i_0):

$$n_{\text{in}}^{i+1} = \sum_{j=i_0}^{i} \beta_j n_{\text{in}}^j. \tag{2.56}$$

The coefficients β_j in Eq. (2.56) should be such as to minimize the residual density under the constraint

$$\sum_{j=i_0}^{i} \beta_j = 1, \tag{2.57}$$

which ensures the conservation of the total number of electrons. Self-consistency is achieved, when the norm of the residual density is below some small chosen value:

$$\langle R\left[n_{\text{in}}\right] | R\left[n_{\text{in}}\right]\rangle < \varepsilon. \tag{2.58}$$

2.3.5 Supercells

Using the plane waves basis set implies periodic boundary conditions. For instance, the solution of the Poisson equation as in Eq. (2.32) is valid only for periodic systems.
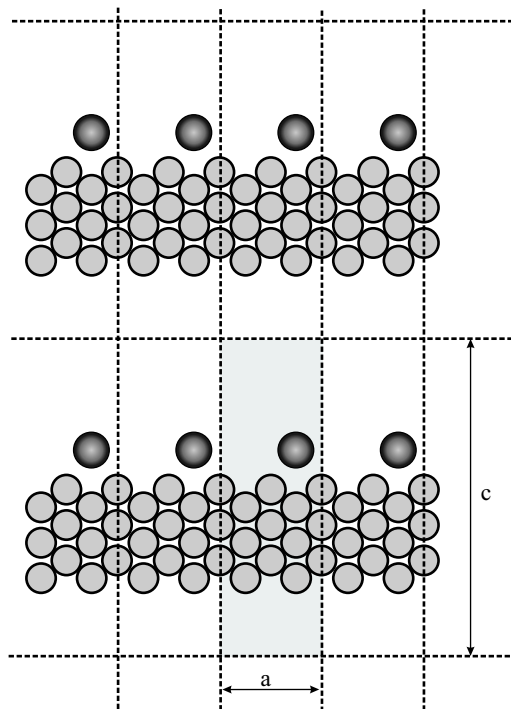
Figure 2.8: Adsorbate covered surface in a slab geometry. a is a lattice constant in the horizontal, c in the vertical direction. Unit cell is shaded.

Periodic boundary conditions is a natural choice for 3D periodic systems, such as solids. However, a 3D-periodicity can be used also for isolated systems, like molecules, or 2D-periodic systems, like surfaces, if one uses a supercell-approach [9]. For molecules this means that the periodic box should be large enough such that interactions of images in different unit cells is negligible. Similarly, for surfaces the periodicity in the vertical direction should be large enough. In Fig. 2.8 the parallel projection of the fcc(110) surface covered with an adsorbate is shown. Dashed lines separate different unit cells, and only the shaded central unit is treated in the calculation explicitly. Lattice constant is a in the horizontal direction, and in c in the vertical direction. There is no interaction between different slabs if c is very large. One has to keep in mind that there are different kinds of interactions that can couple different slabs in the vertical direction. First, overlap of electronic wavefunctions perpendicular to the surface leads to a dispersion of electronic states, and therefore effective interaction. Thus, slabs should be separated far apart such that there is no density overlap between the repeated slabs.

More dramatic effects happen for ionic surfaces, for instance, when the surface is covered by adsorbates, as in Fig. 2.8. Charge transfer from the metal to the adsorbates (or vice versa) leads to the electrostatic potential jump at the interface (very similar to Fig. 1.5b in Chapter 1). This creates an artificial electric field between the slabs, which affects the total energy calculation. A cheap way to avoid this, like in the previous case, is to use large enough c such that the artificial electric field is very small. Another, and more appropriate, possibility is to use the so-called dipole correction, where the electric

field created by the charge transfer is counterbalanced by an external field.

2.4   Performance

In this section we address the performance of GGA-PBE for copper and silver bulk and surfaces. The performance of DFT for molecules will be discussed in Chapters 4 and 5, in which the adsorption of molecules on silver and copper surfaces is studied.

2.4.1   Silver: bulk and surfaces

In this section the test calculations for bulk silver and low-index silver surfaces are presented. For Ag Troullier-Martins pseudopotentials used in this work, the total energies are well converged at 50 Ry kinetic energy cutoff (see Fig. 2.5), and this cutoff was therefore used in all calculation containing only silver atoms. The Brillouin zones of all periodic systems were sampled using special k-points generated according to the Monkhorst-Pack scheme in conjunction with a Fermi smearing of 0.01Ha (0.27eV). Tests were performed to converge the total energies with respect to the k-point mesh (see Fig. 2.6).

For bulk fcc silver, the total energy was calculated for several lattice constants a. The binding energy is defined then as $E_b(a) = E_{bulk}(a) - E_{atom}$, where E_{bulk} and E_{atom} are total energies of bulk fcc silver (per one atom) and of an isolated silver atom, respectively. The total energy of an atom was taken from spin-unpolarized calculation (spin polarization lowers the total energy by 0.18eV). Binding energy vs. lattice constant curve was fitted to the Murnaghan equation of state [21] to extract effective parameters. The Murnaghan equation of state for fcc lattices reads:

$$E_b(a) = E_0 + \frac{Ba^3}{4\alpha}\left[\left(\frac{a_0}{a}\right)^{3\alpha}\frac{1}{\alpha-1}+1\right] - \frac{Ba_0^3}{4}\frac{1}{\alpha-1}. \tag{2.59}$$

Here, a_0 is the equilibrium lattice constant, E_0 is the binding energy at equilibrium (the cohesive energy), B is the bulk modulus, and $\alpha = (\partial B/\partial P)_{V_0}$ is the derivative of bulk modulus with respect to pressure at equilibrium volume. The calculated $E_b(a)$ values and the fit are depicted in Fig. 2.9. The values are listed in Table 2.1 and are compared to the experimental results, as well as other calculations [24, 25]. Compared to experiment, PBE predicts a lattice constant about 3% too large, the cohesive energy 13% too small, and the bulk modulus about 15% too small.

Once the equilibrium lattice constant is found, one can calculate the band structure and density of states $\mathcal{D}(E)$. We have calculated DOS using the formula

$$\mathcal{D}(E) = \sum_{\mathbf{k}}\sum_{n} w_{\mathbf{k}} g_\sigma(E - \epsilon_{n,\mathbf{k}}), \tag{2.60}$$

where $g_\sigma(x)$ is a Gaussian smearing function, and the summation is carried over the special k-points, used in the actual calculation (see Eq. (2.38)). The band structure and DOS are plotted in Fig. 2.10. Silver is a noble metal, and the d states, which are quite localized in real space and show much less dispersion than the sp bands, produce a narrow but high peak in the density of states, and are located 3eV below the Fermi energy.
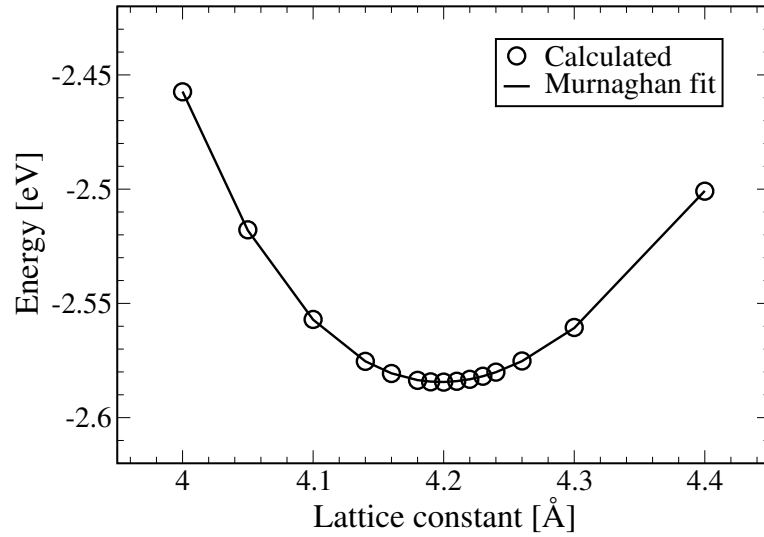
Figure 2.9: Binding energy of bulk fcc Ag as a function of the lattice constant. Open circles are calculated values, solid line is a fit to the Murnaghan equation of state (Eq. 2.59).

	This work	Exp. [22]	Ref. [24]	Ref. [25]
Lattice constant a_0 [Å]	4.20	4.08	4.20	4.16
Cohesive energy E_0 [eV]	2.58	2.95	2.56	2.55
Bulk modulus B [mbar]	0.86	1.01	0.87	0.91
$\alpha = (\partial B/\partial P)_{V_0}$	5.82	-	-	-

Table 2.1: The calculated equilibrium properties of bulk silver: lattice constant a_0, cohesive energy E_0, bulk modulus B and the derivative of bulk modulus with respect to pressure α.

Bulk fcc Ag
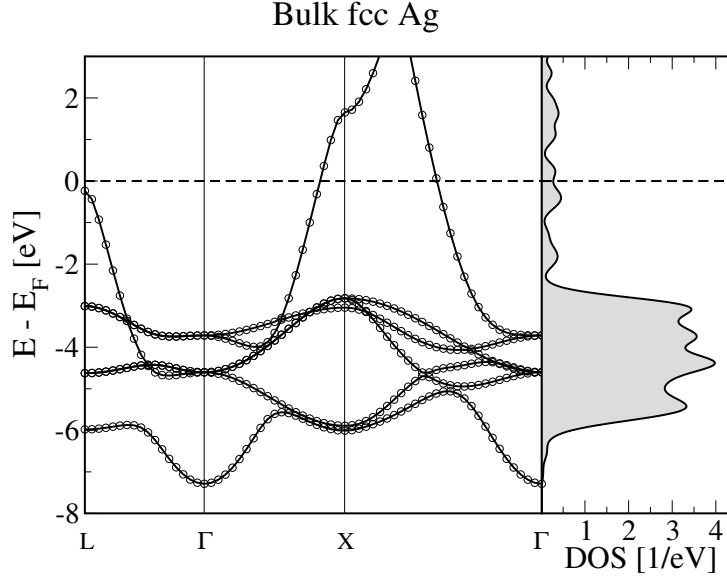
Figure 2.10: Calculated PBE-GGA band structure (left) and total density of states (right) of bulk silver. Fermi energy is set to zero.

Ag(001)	This work	Exp.	Ref. [23]	Ref. [25]
Work function Φ_m [eV]	4.27	4.26	4.33	4.14
Surface energy E [eV/atom]	0.41	0.88	0.43	0.45
Δd_{12} [%]	-1.92	$-$	-1.87	-2.26
Δd_{23} [%]	$+0.35$	$-$	$+0.51$	-0.10
Δd_{34} [%]	$+0.47$	$-$	$+0.36$	$-$

Table 2.2: Energetic and structural parameters of the Ag(001) surface. Δd_{ij} is the expansion/contraction of the interlayer distance between the i-th and the j-th topmost layer.

We have carried out test calculations of low-index silver surfaces Ag(111), Ag(001) and Ag(110). In addition to the surface energy (i.e. half the energy needed to break the bulk into two semi-infinite solids), we have calculated the work function of each surface, as well as the vertical relaxations of the topmost atomic layers. By definition, the work function of the surface is the difference between the electrostatic potential in the vacuum and the Fermi energy of the solid. In Fig. 2.11, the xy-averaged electrostatic potentials are plotted for all three silver surfaces. In accord with the experiment, the work function increases in the sequence (110)<(001)<(111). It is long known in surface science that the work functions of close-packed fcc(111) surfaces are larger than those of open fcc(110) surfaces of the same material. The difference can be explained by an effect, which is called the Smoluchowski smoothening. Surface energies are smaller than the experimental ones. Tables 2.2, 2.3 and 2.4 summarize the calculations of silver surfaces and compare them to the experimental results (when possible) and other calculations from the literature.
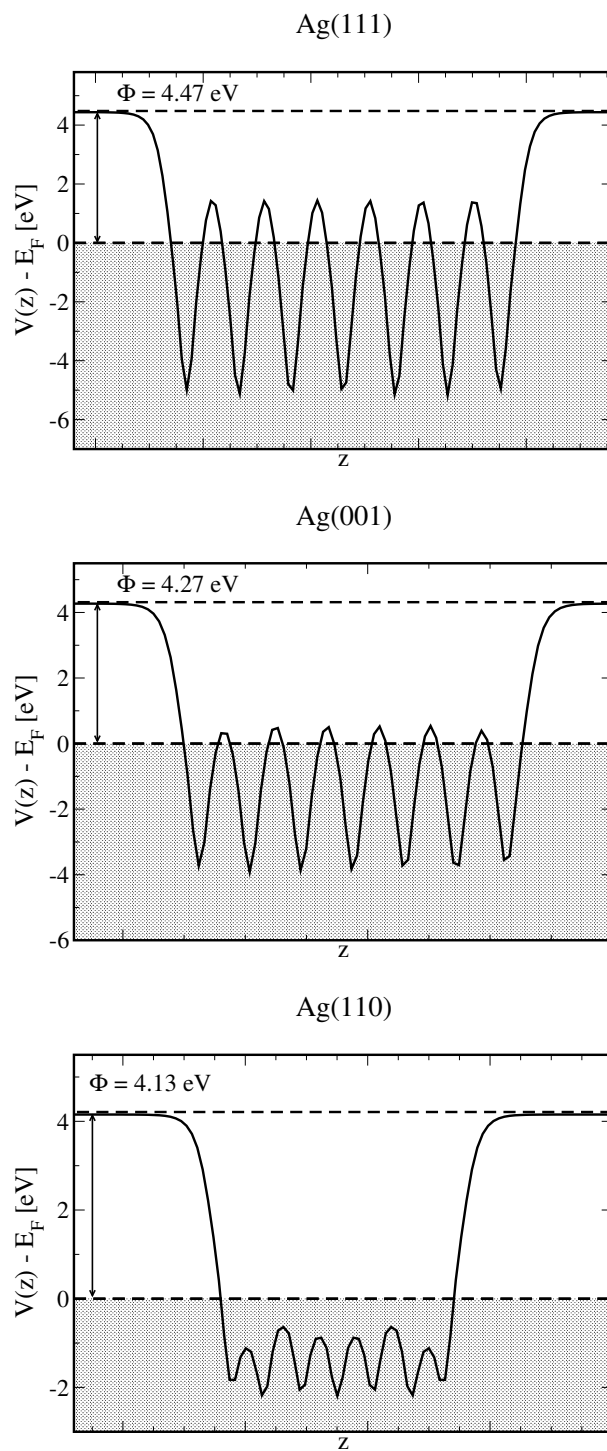
Ag(111)

Ag(001)

Ag(110)

Figure 2.11: xy-averaged electrostatic potentials of the low index silver surfaces. In all cases slabs consisted of seven silver layers. Fermi levels are set to zero and work functions Φ of clean surfaces are indicated.

Ag(110)	This work	Exp.	Ref. [23]
Work function Φ_m [eV]	4.13	4.14	4.30
Surface energy E [eV/atom]	0.62	1.18	0.65
Δd_{12} [%]	-8.20	–	-9.2
Δd_{23} [%]	$+3.10$	–	$+4.1$
Δd_{34} [%]	-1.20	–	-1.5

Table 2.3: Energetic and structural parameters of the Ag(110) surface.

Ag(111)	This work	Exp.	Ref. [23]
Work function Φ_m [eV]	4.47	4.46	4.65
Surface energy E [eV/atom]	0.31	0.55	0.36
Δd_{12} [%]	-0.17	–	-0.3
Δd_{23} [%]	-0.20	–	$+0.04$
Δd_{34} [%]	$+0.20$	–	$+0.16$

Table 2.4: Energetic and structural parameters of the Ag(111) surface.

2.4.2   Copper: bulk and surfaces

Similar calculations were performed for bulk copper and copper surfaces. Fig. 2.12 shows the calculated values of the binding energy as a function of the lattice constant and the Murnaghan fit to the data. Table 2.5 summarizes the results of the fit and compares them to the experimental parameters and other calculations. In Fig. 2.13 the band structure and DOS of bulk copper is presented. The d states of copper are closer to the Fermi energy than those of of silver. Similarly to Fig. 2.11, Fig. 2.14 shows the xy-averaged electrostatic potential, from which the work functions of Cu(001) and Cu(111) can be calculated. Tables 2.6 and 2.7 summarize the results of surface calculations.

	This work	Exp. [22]
Lattice constant a_0 [Å]	3.68	3.61
Cohesive energy E_0 [eV]	3.60	3.50
Bulk modulus B [mbar]	1.33	–
$\alpha = (\partial B/\partial P)_{V_0}$	5.82	–

Table 2.5: Calculated equilibrium properties of bulk copper: lattice constant a_0, cohesive energy E_{coh}, bulk modulus B and the derivative of bulk modulus with respect to pressure α.
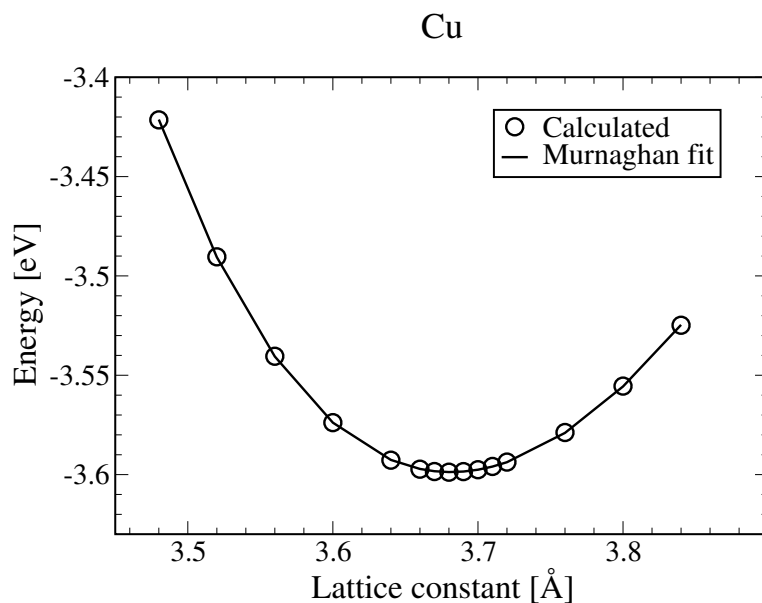
Figure 2.12: Binding energy of bulk fcc Cu as a function of the lattice constant. Open circles are calculated values, solid line is a fit to the Murnaghan equation of state.
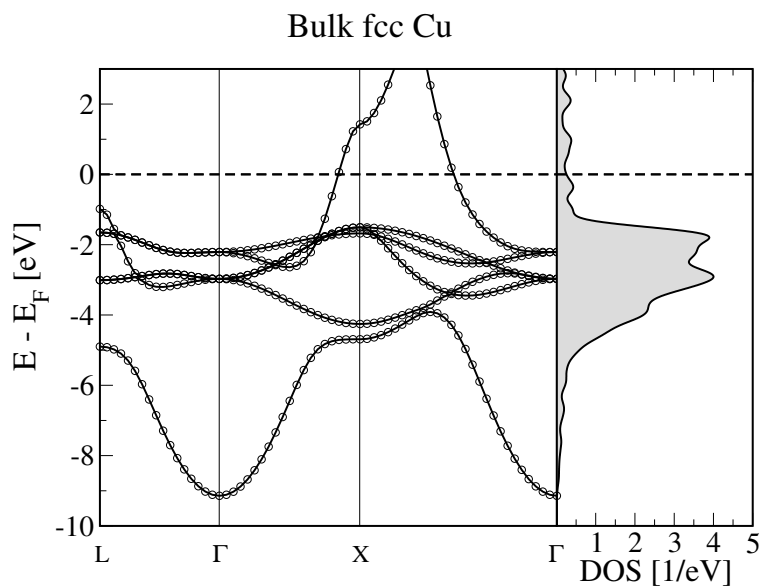

Figure 2.13: Calculated PBE-GGA band structure (left) and total density of states (right) of bulk copper. Fermi energy is set to zero.
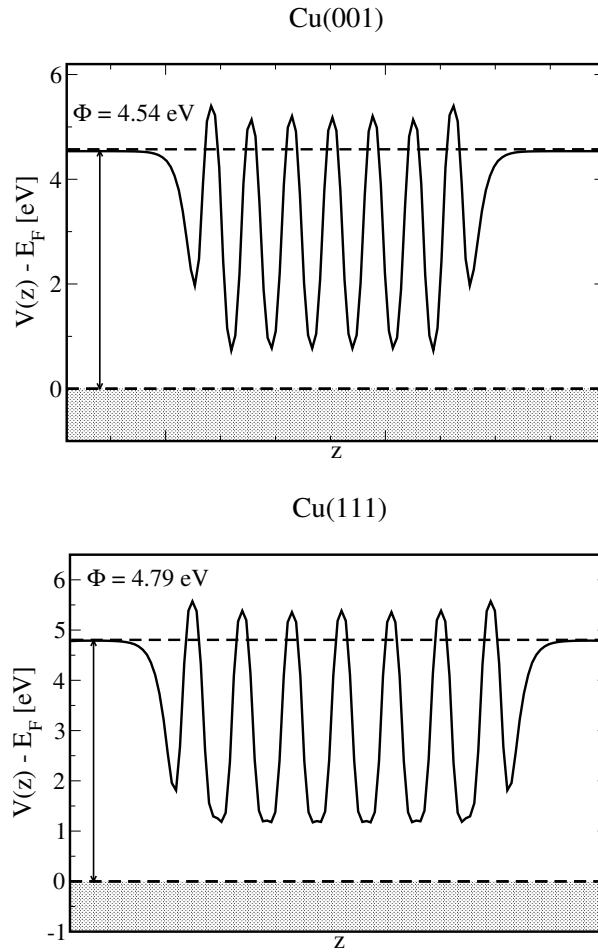
Figure 2.14: xy-averaged electrostatic potentials of low index copper surfaces. In all cases slabs consisted of seven copper layers. Fermi levels are set to zero and work functions Φ of clean surfaces are indicated.

Cu(001)	This work	Exp.
Work function Φ_m [eV]	4.54	$4.59 - 4.65$
Surface energy E [eV/atom]	0.55	0.73

Table 2.6: Energetic parameters of the Cu(001) surface.

Cu(111)	This work	Exp.
Work function Φ_m [eV]	4.79	4.94
Surface energy E [eV/atom]	0.41	0.62

Table 2.7: Energetic parameters of the Cu(111) surface.

2.5 Density difference

In this last section of the current chapter we will introduce a helpful tool to study the formation of chemical bonds. In Chapters 3 and 4 we will speak about surface bonds, but it is more instructive to discuss the concept employing simpler chemical systems. Let A and B be two atoms which react and form a diatomic molecule. A great deal of useful information about the nature of the bond is given by the density difference function. Let n_A be the electron density of the isolated atom A, n_B the electron density of the isolated atom B, and n_{AB} the electron density of the molecule AB. The density difference is defined as:

$$\Delta n = n_{AB} - n_A - n_B. \tag{2.61}$$

Let us look at two simple examples - a covalently bonded H_2 molecule and a He_2 dimer. In the language of molecular orbitals, two $1s$ atomic orbitals form the bonding σ_g and the anti-bonding σ_u molecular orbitals. When the H_2 molecule is formed, two electrons occupy the bonding orbital and one expects a charge accumulation in between the hydrogens, which would reflect the formation of the chemical bond. Indeed, the density difference function in Fig. 2.15, top, shows that there is a charge accumulation in the middle of the H-H bond, and a depletion of charge at the periphery. In the case of the He_2 dimer there is no chemical bond and little changes can be seen in the density difference function at the equilibrium He-He distance. For distances much smaller than the equilibrium distance, the density difference function reveals that there is a electron charge depletion region in between the two atoms, and a charge accumulation region at the periphery. This charge depletion results from the Pauli exclusion principle and is the origin of the resulting He-He repulsion. These two cases are extreme examples, but they show that the density difference function Eq. (2.61) is a useful quantity. In Chapters 3 and 4 we will use an equivalent of this function to interpret our DFT calculations of adsorbate covered surfaces.
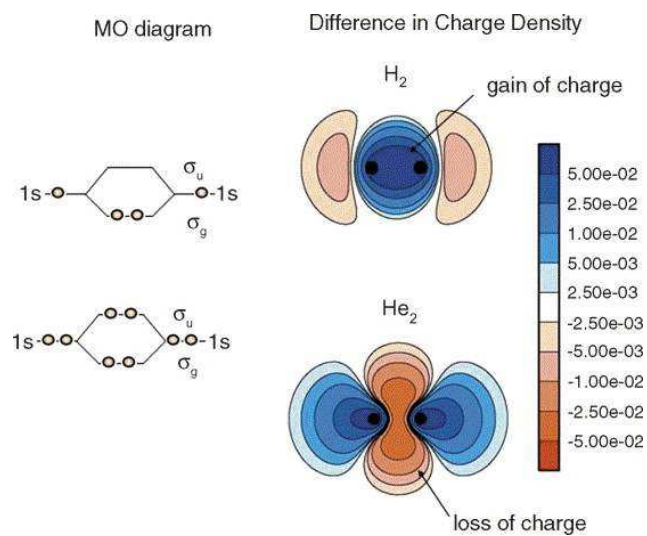
Figure 2.15: The molecular orbital diagram (left) and density difference plots for the H_2 (top) and the He_2 (bottom) molecules. Charge accumulation in between two H atoms indicates the formation of the covalent bond. Charge depletion in between two He atoms leads to a repulsive force between them. Taken from Ref. [26].

Bibliography

[1] P. Hohenberg and W. Kohn, *Inhomogeneous electron gas*, Phys. Rev. **136**, B864 (1964).

[2] W. Kohn and L.J. Sham, *Self-consistent equations including exchange and correlation effects*, Physical Review **140**, A1133 (1965).

[3] R.O. Jones and O. Gunarsson, *The density functional formalism, its applications and prospects*, Rev. Mod. Phys. **61**, 689 (1989).

[4] K. Flensberg and H. Bruus, *Many-body quantum theory in condensed matter physics* (Cambridge University Press).

[5] J.P. Perdew and Y. Wang, *Accurate and simple analytic representation of the electron-gas correlation energy*, Phys. Rev. B **45**, 13244 (1992).

[6] W. Koch and M.C. Holthausen, *A Chemist's guide to the density functional theory* (Wiley-VCH, Weinheim, 1999).

[7] J.P. Perdew and S. Kurth, *Density functionals for non-relativistic coulomb systems in the new century*, Springer Lecture Notes in Physics **620**, 1 (2003).

[8] J.P. Perdew, K. Burke, and M. Ernzerhof, *Generalized gradient approximation made simple*, Phys. Rev. Lett. **77**, 3865 (1996).

[9] M.C. Payne, M.P. Teter, D.C. Allan, T.A. Arias, and J.D. Joannopoulos, *Iterative diagonalization techniques for ab-initio total-energy calculations: molecular dynamics and conjugate gradients*, Rev. Mod. Phys. **64**, 1045 (1992).

[10] D.R. Hamann, M. Schlüter, and C. Chiang, *Norm-conserving pseudopotentials*, Phys. Rev. Lett. **43**, 1494 (1979).

[11] N. Troullier and J.L. Martins, *Efficient pseudopotentials for plane-wave calculations*, Phys. Rev. B **43**, 1993 (1991).

[12] L. Kleinman and D.M. Bylander, *Efficacious form for model pseudopotentials*, Phys. Rev. Lett. **48**, 1425 (1982).

[13] X. Gonze, P. Käckell and M. Scheffler, *Ghost states for separable, norm-conserving, ab initio pseudopotentials*, Phys. Rev. **41**, 12264 (1990).

[14] X. Gonze, R. Stumpf, and M. Scheffler, *Analysis of separable pseudopotentials*, Phys. Rev. B **44**, 8503 (1991).

[15] M. Fuchs and M. Scheffler, *Ab initio pseudopotentials for electronic structure calculations of polyatomic systems using density-functional theory*, Comp. Phys. Comm. **119**, 67 (1999).

[16] M.J. Gillan, *Calculation of the vacancy formation energy in aluminium*, J. Phys. Cond. Mat. **1**, 689 (1989).

[17] L.D. Landau and E.M. Lifshitz, Statistical Physics (Pergamon Press).

[18] H.J. Monkhorst and J.D. Pack, S*pecial points for Brillouin-zone integrations*, Phys. Rev. B **13**, 5188 (1976).

[19] R. Car and M. Parrinello, *Unified Approach for Molecular Dynamics and Density-Functional Theory*, Phys. Rev. Lett. **55**, 2471 (1986).

[20] G. Kresse and J. Furthmüller, *Efficiency of ab-initio total energy calculations for metals and semiconductors using plane-wave basis set*, Comp. Mat. Sci. **6**, 15 (1996).

[21] F.D. Murnaghan, *The compressibility of media under extreme pressures,* Proc. Nat. Acad. Sci. **30**, 344 (1944).

[22] C. Kittel, *Introduction to solid state physics* (John Wiley and sons, New York, 1971).

[23] Y. Wang, W. Wang, K.-N. Fan, and J. Deng, *Structural and electronic properties of silver surfaces: ab initio pseudopotential density functional study*, Surf. Sci. **490**, 125 (2001).

[24] W.-X. Li, C. Stampfl, and M. Scheffler, *Oxygen adsorption on Ag(111): a density-functional theory investigation*, Phys. Rev. B **65**, 075407 (2002).

[25] A. Migani, C. Sousa, and F. Illas, *Chemisorption of atomic chlorine on metal surfaces and the interpretation of the induced work function changes*, Surf. Sci. **574**, 297 (2005).

[26] A. Nilsson and L.G.M. Pettersson, *Chemical bonding on surfaces probed by X-ray emission spectroscopy and density functional theory*, Surf. Sci. Rep. **55**, 49 (2004).

Chapter 3

Chlorine on Ag(111) at submonolayer coverage

In this chapter we describe a simple surface science system - chlorine adsorbed on the Ag(111) surface at submonolayer coverage ($\theta < 1$). We review the most important experimental works, then give a summary of the computational details and finally present the results of DFT calculations and their interpretation. Emphasis is put on theoretical tools used in the analysis of DFT calculations of surface science systems. Comparison with relevant experimental data is made.

3.1   Review of experimental results

In this section we briefly review the most important experimental facts about Cl on Ag(111), investigations of which have quite a long history. The work of Bowker and Waugh represents one of the most thorough early studies [1]. Cl_2 was found to adsorb dissociately, with an initial sticking probability of 0.4. This indicates that atomic adsorption is more favourable than molecular adsorption. In addition, once on the silver surface, chlorine cannot be desorbed neither in molecular nor atomic state, but rather as silver chloride molecules and clusters. The interaction of chlorine with silver surfaces is therefore very strong. The motivation to study Cl/Ag comes from the field of heterogeneous catalysis [2]. Chlorine serves as a promoter of the selective epoxidation of ethylene on silver surfaces. The reaction is a partial oxidation, is described as

$$C_2H_4 + O \rightarrow C_2H_4O,$$
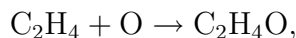
and runs in the presence of silver catalyst. Interestingly, all halogens (F, Cl, Br and I) increase the activity of the silver catalyst. In contrast, only chlorine increases *selectivity* (i.e. epoxidation rather than full burning with production of water and carbon dioxide) [3]. Bearing this in mind, the bulk of experimental work concentrated on industrial conditions, i.e. high pressures [4] and high temperatures [5]. On the contrary, low coverage and low temperature experimental data is more useful for a comparison to our theoretical calculations. Below, we describe two aspects of such experiments - the electronic structure

of chlorine adsorbed on the Ag(111) surface in the sub-monolayer regime, and the atomic structure of the overlayers.

Electronic structure. Adsorption of chlorine on silver surfaces is accompanied by a big increase in the work function. At the saturation coverage, the change is $\Delta\Phi = 1.5 \div 1.8\text{eV}$ [6,7]. We will discuss the experimental data of work function changes in more detail when comparing them to calculated values (Fig. 3.10). The valence electronic structure of the Cl/Ag(111) interface was studied most recently by Pasquali *et al.* [7]. Relatively little changes were seen in valence band ultraviolet photo-emission (UPS) spectra due to a significant overlap of the chlorine-induced features and the silver d-states. However, metastable atom deexcitation spectroscopy, which is a very surface-sensitive technique, shows that chlorine-induced features appear on both sides of the silver d-states [7]. In particular, an antibonding Cl-3p derived state was seen at about -3eV below the Fermi level. We will compare this conclusion with our result.

Atomic structure. The atomic structure of the chlorine adlayer was investigated by several research groups. The most important findings are summarized in the "phase diagram", Fig. 3.1. There, a schematic coverage-temperature $(\theta - T)$ phase diagram is shown and the "scan-lines" of different experiments are indicated. There is much literature about room-temperature (RT) phases of Cl/Ag(111). According to low energy electron diffraction (LEED) patterns, recorded as a function of chlorine exposure (line a in Fig. 3.1), no ordered structures are observed (thin solid line) at low coverage. Slightly below the saturation coverage $\theta_{sat} > 1/3$ (above which the sticking probability reduces drastically and adsorption becomes very difficult), well-defined LEED pattern emerge (thick solid line). However, there is no consensus in the literature about the nature and even periodicity of this structure [8,9,10]. Patterns like 3×3, 10×10 or 13×13 were proposed on the basis of LEED measurements. Andryushechkin *et al.* [11] conjectured a 17×17 registry for this saturation coverage phase on the basis of STM measurements. It may well happen, that at RT, just below the saturation coverage θ_{sat}, a series of closely related structures exist. For saturation coverage θ_{sat} itself, different values, like 0.45, 0.49 or 0.54 were proposed.

Shard and Dhanak [12] investigated the Cl/Ag(111) system at $\theta = 1/3$ as a function of temperature (line b in Fig. 3.1). A sharp LEED pattern indicating an ordered $\sqrt{3} \times \sqrt{3}R30^0$ overlayer was only found at low temperatures. Heating this $\sqrt{3} \times \sqrt{3}R30^0$ structure above 195K resulted in the fractional order spots becoming abruptly diffuse. The order-disorder transition occurred over a small temperature range (about 2K). The disordering mechanism has not been investigated in the literature, however, and is not known at present. Also, no experimental data exist for other regions of the $\theta - T$ diagram.

It is an interesting fact that the phase diagram of chlorine on the Ag(001) surface is fundamentally different [13,14]. The order-disorder transition occurs at a certain coverage $\theta_c \approx 0.39$ and is only very weakly temperature dependent. Chlorine atoms on the Ag(001) surface behave almost like a lattice gas of hard spheres with infinite nearest-neighbour repulsion and (almost) zero interaction energy for larger chlorine-chlorine separations.
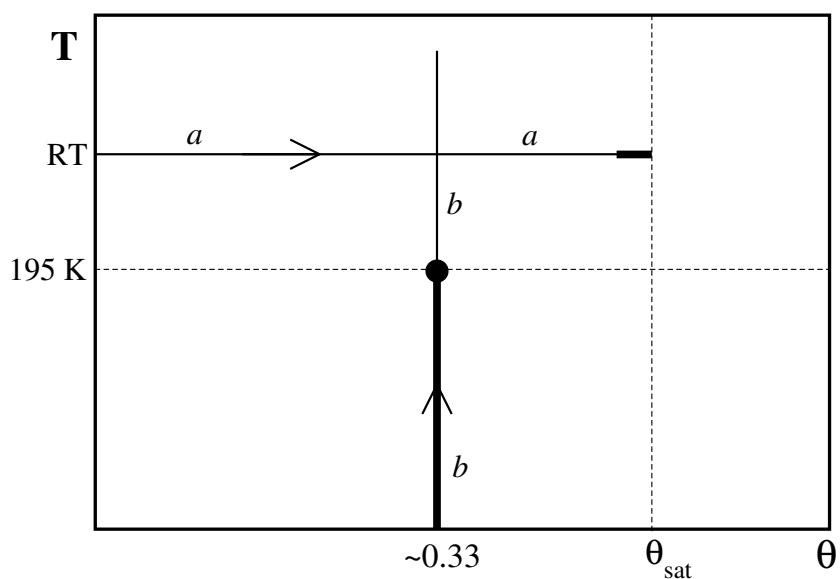
Figure 3.1: Schematic experimental "phase diagram" of the chlorine adlayer on the Ag(111) surface. The regions in the $\theta - T$ space for which experimental data is available, are shown by solid lines (a and b). Line a: room temperature (RT), variable coverage. An ordered phase occurs just below the saturation coverage $\theta_{sat} \approx 0.45$ [11]. In reality, several closely related phases may exist in this region. Line b: $\theta \approx 0.33$, temperature is varied. Order-disorder transition occurs at $T \approx 195K$ [12]. No data exists for other regions. In the diagram, ordered phases are represented by thick lines, disorder phases by thin lines. Order-disorder transition point at $\theta \approx 0.33$ is marked by a black solid circle.
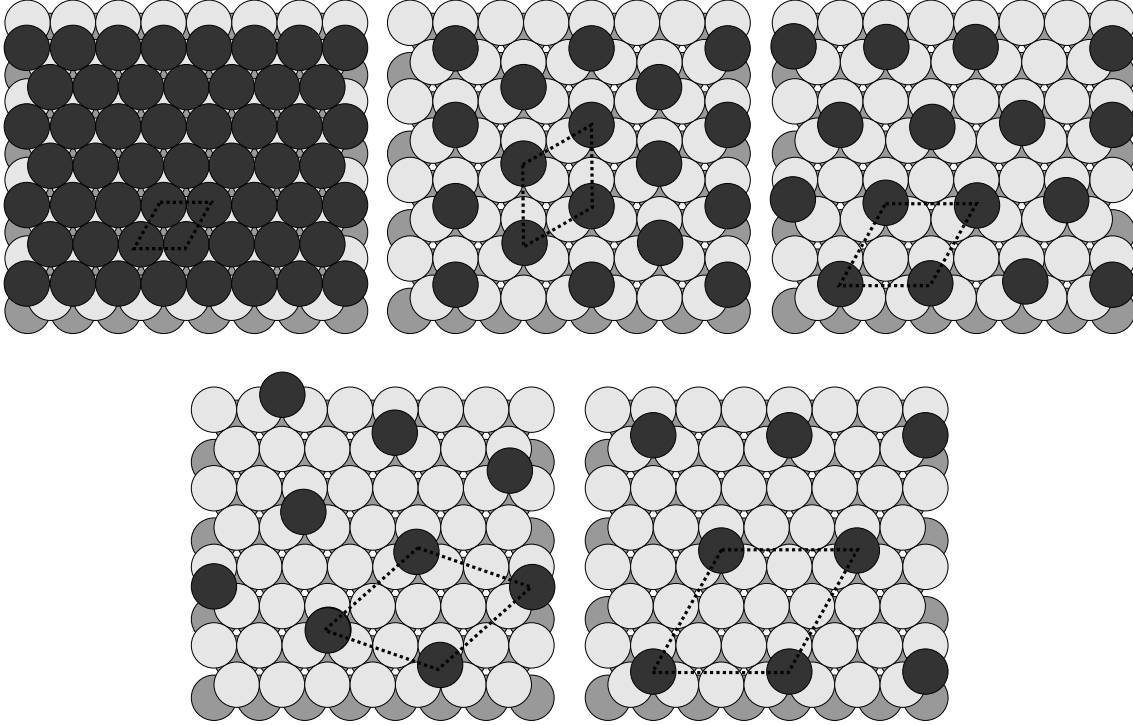
Figure 3.2: Assumed structures of Cl on Ag(111): 1×1, $\sqrt{3}\times\sqrt{3}R30^0$, 2×2, $\sqrt{7}\times\sqrt{7}R19.1^0$ and 3×3. Surface lattice constants are $d = \beta a_0$, where a_0 is the silver-silver nearest-neighbour distance and $\beta = 1, \sqrt{3}, 2, \sqrt{7}$ and 3 for the five structures, respectively.

3.2   Computational details

DFT total energy calculations in this chapter were performed with the CPMD code [15] using a free-energy density functional implementation, applicable to metals [16]. In the calculations the Perdew-Burke-Ernzerhof functional was employed, and wave functions were expanded in plane-waves with a kinetic energy cutoff of 50 Ry. Fermi smearing of 2000 K was applied (Eq. (2.38) in Chapter 2), and total energies were extrapolated to zero Kelvin (Eq. (2.43) in Chapter 2). Iterative diagonalization was performed using the Pollard-Friesner modification of the Lanczos algorithm [17]. In self-consistency cycles Anderson density mixing with a parameter $\alpha = 0.03$ was used. To describe atomic cores, Troullier-Martins norm-conserving pseudopotentials were used in their non-local Kleinman-Bylander form. To get rid of ghost states, the s component was taken as the local potential for silver.

Geometry optimization was performed with the low-memory BFGS algorithm (LBFGS) [18] until the maximum force was less than $5\cdot10^{-4}$ Hartree/bohr, while total energies were converged to within $5\cdot10^{-5}$eV. We found that LBFGS was the most stable optimizer for this systems from all the optimizers available in the CPMD package. This optimizer is similar to the conventional BFGS method, but takes, for example, additional precaution in the regions of small energy gradients, where BFGS becomes unstable. During the geometry optimization, the forces acting on atoms were symmetrized according to the
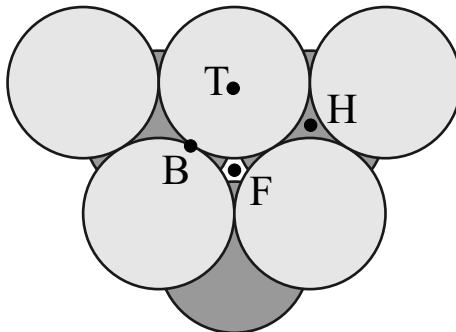
Figure 3.3: High symmetry adsorption sites on the fcc(111) surface: B - bridge site, T - on-top site, F - fcc hollow, H - hcp hollow.

assumed local adsorption symmetry which was then preserved during all iterations.

In the next section we present calculations of chlorine adsorbed on the Ag(111) surface at different coverages. Unit cells with different lattice constants were used. Figure 3.2 shows five lateral surface supercells used in the calculations. Black circles are adsorbed chlorine atoms, light gray circles are silver atoms in the topmost atomic layer, dark gray circles are silver atoms in the second topmost atomic layer. The unit cells of increasing size are indicated by dashed lines. The drawn structures, referred to the substrate, are denoted as 1×1, $\sqrt{3}\times\sqrt{3}R30^0$, 2×2, $\sqrt{7}\times\sqrt{7}R19.1^0$, and 3×3, and correspond to chlorine coverages 1, 1/3, 1/4, 1/7, and 1/9, respectively. The surface lattice constants of the five supercells are $d = \beta a_0$, where a_0 is the silver nearest neighbour distance (calculated PBE value 2.90Å) and $\beta = 1$, $\sqrt{3}$, 2, $\sqrt{7}$ and 3 for the corresponding lattices. The 1×1 structure is never seen in experiment and should be highly unfavourable, because the nearest neighbour distance between adsorbates is much smaller than the sum of their atomic radii. However, we also performed calculations for this structure. For each of the unit cells, a chlorine atom was placed either in the fcc or hcp hollow site (see Fig. 3.3). These are two high symmetry adsorption sites, which were shown to be the most favourable in the $\sqrt{3} \times \sqrt{3}R30^0$ structure [19, 20, 21]. For the lowest coverage we also performed calculations of chlorine adsorbed in the bridge site. Indeed, the bridge site was found to be less energetically favourable and most likely corresponds to the saddle point for diffusion between the fcc hollow and the hcp hollow.

Five layers of silver atoms were considered with a vacuum region equivalent to eight layers. During geometry optimization, the top three layers as well as the vertical position of the adsorbate were allowed to relax while the bottom two silver layers were fixed in their bulk positions. Due to imposed symmetry the lateral force acting on the adsorbate was exactly zero.

Before calculations of the full adsorbate-substrate system were performed, we made test calculations for the bare Ag(111) substrate using the same lateral unit cells and lateral periodicities as for the adsorbate covered surfaces. Let n_{at} be the number of silver atoms in each atomic layer per lateral unit cell, N_{at} the total number of silver atoms per lateral unit cell ($N_{at} = 5n_{at}$ in our case), E_{tot} the total energy of the slab, and ϵ_{bulk} the total energy of bulk silver per one atom. The surface energy is then:

Supercell	1×1	$\sqrt{3} \times \sqrt{3}R30^0$	2×2	$\sqrt{7} \times \sqrt{7}R19.1^0$	3×3
k-point Mesh	$13 \times 13 \times 1$	$9 \times 9 \times 1$	$7 \times 7 \times 1$	$5 \times 5 \times 1$	$5 \times 5 \times 1$
N_k	21	12	8	6	5
n_{at}	1	3	4	7	9
$N_{at} = 5n_{at}$	5	15	20	35	45
E_{sub} [Ha]	-180.88794	-542.66512	-723.549294	-1266.2160	-1627.994737
$N_{at} \times \epsilon_{bulk}$ [Ha]	-180.9125	-542.73750	-723.65000	-1266.3875	-1628.2125
E_S[eV]	**0.334**	**0.328**	**0.342**	**0.333**	**0.329**

Table 3.1: Computational details and results of calculations for different lateral supercells of the Ag(111) surface. N_k is the number of special k-points, n_{at} is the number of silver atoms per one unit cell and per one atomic layer, N_{at} is the total number of silver atoms per unit cell, E_{sub} is the total energy of the slab, ϵ_{bulk} is the total energy of bulk silver per one atom, and E_S is the surface energy of Ag(111) per one surface atom.

$$E_S = (E_{sub} - N_{at}\epsilon_{bulk}) / (2n_{at}) . \tag{3.1}$$

Ideally, E_S should be independent of the surface unit cell used in the actual calculations. In reality, there are some small differences. Table 3.1 summarizes the results of the test calculations.

3.3   Results and discussion

The adsorption energy was calculated using the formula:

$$E_{ad} = - (E_{tot} - E_{sub} - E_{at}) . \tag{3.2}$$

Here, E_{tot} is the total energy of the adsorbate-substrate system, E_{sub} is the total energy of the bare slab (see Table 3.1), E_{at} is the total energy of the chlorine atom in a big computational box (to ensure zero interaction with its images). The total energies of periodic systems, appearing in Eq. (3.4), were extrapolated to zero temperature, and evaluated for the five different lateral supercells (Fig. 3.2) and the two local adsorption sites - fcc and hcp hollow (Fig. 3.3). The adsorption energies are shown in Fig. 3.4 as a function of the surface lattice constant. Two conclusions can be immediately drawn: (i) except for the highly-unfavourable 1×1 surface unit cell, the adsorption energy is weakly dependent on interparticle spacing and is approximately 2.9eV. Later, we will see that a small variation of the adsorption energy can be explained by a weak electrostatic repulsion between adsorption-induced dipoles on the surface. (ii) the fcc hollow site is more energetically favourable than the hcp hollow site at all coverages. The difference in adsorption energies between these two sites is very small, however, $E_{ad}^{fcc} - E_{ad}^{hcp} \approx 7 \div 12$meV, and is only weakly dependent on the coverage. The experimental value of this difference is not known. However, for the rather similar system, Cl/Cu(111), a value of less than 10meV was proposed on the basis of X-ray standing wave experiments and
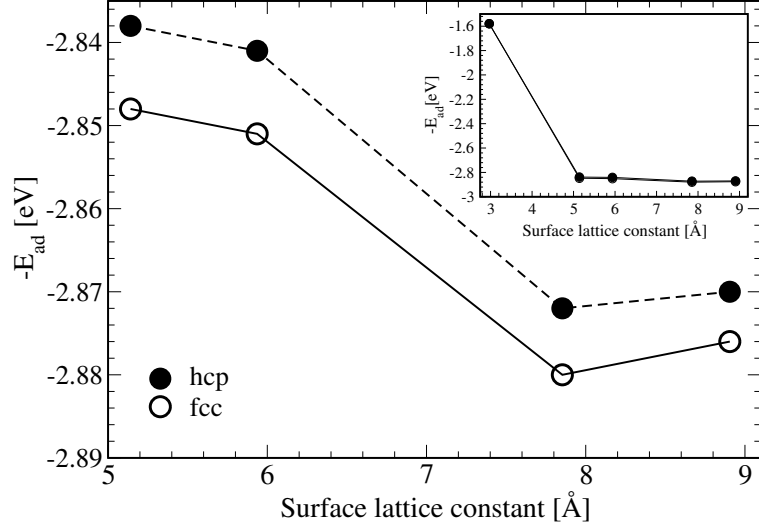
Figure 3.4: Adsorption energies of chlorine on Ag(111) as a function of a surface lattice constant. Filled circles - hcp hollow sites, empty circles - fcc hollow sites. Inset shows the same data with the 1×1 structure included.

Monte-Carlo simulations [22]. Our findings are consistent with this conclusion. In DFT studies of the $\sqrt{3} \times \sqrt{3}R30^0$ structure, other authors obtained values of 12meV [19], 9meV [20] or 7meV [21] for Cl/Ag(111). Thus, all studies confirm that the difference in adsorption energies in fcc and hcp sites is indeed very small. For a comparison, this difference is 180meV for O/Ag(111) [23] and 200meV for O/Pd(111) [24], as might be expected for a smaller, more electronegative adsorbate.

Now let us concentrate on the bonding mechanism between the chlorine and the Ag(111) substrate. In Fig. 3.5, bottom, the surface band structures of the bare substrate and the adsorbate-covered surface are depicted for the $\sqrt{3} \times \sqrt{3}R30^0$ structure. In both cases, Fermi energies were set to zero. The locations of the high-symmetry k-points $\overline{M}$, $\overline{K}$ and $\overline{\Gamma}$ in the Brillouin zone (BZ) are explained in Fig. 3.5, top. We can clearly see the appearance of chlorine-induced antibonding state, located about -2.4eV below E_F. The state marked with an asterisk (*) in the right panel is absent in the left panel.

To gain a better understanding of the chlorine-induced modifications of the electronic structure, we calculated the density of states $\mathcal{D}$ (DOS) of the slab with and without the adsorbate. DOS was calculated employing the formula (the same as Eq. (2.59) in Chapter 2):

$$\mathcal{D}(E) = \sum_{\mathbf{k}} \sum_{n} w_{\mathbf{k}} g_{\sigma}(E - \epsilon_{n,\mathbf{k}}) \tag{3.3}$$

The sum runs over the special k-points $\mathbf{k}$ used in the actual calculation, and all the electronic states n at each k-point, $w_{\mathbf{k}}$ being the weight of each special k-point (see Chapter 2, section 2.3.3), and $g_{\sigma}(x)$ a normalized, symmetric smearing function. We
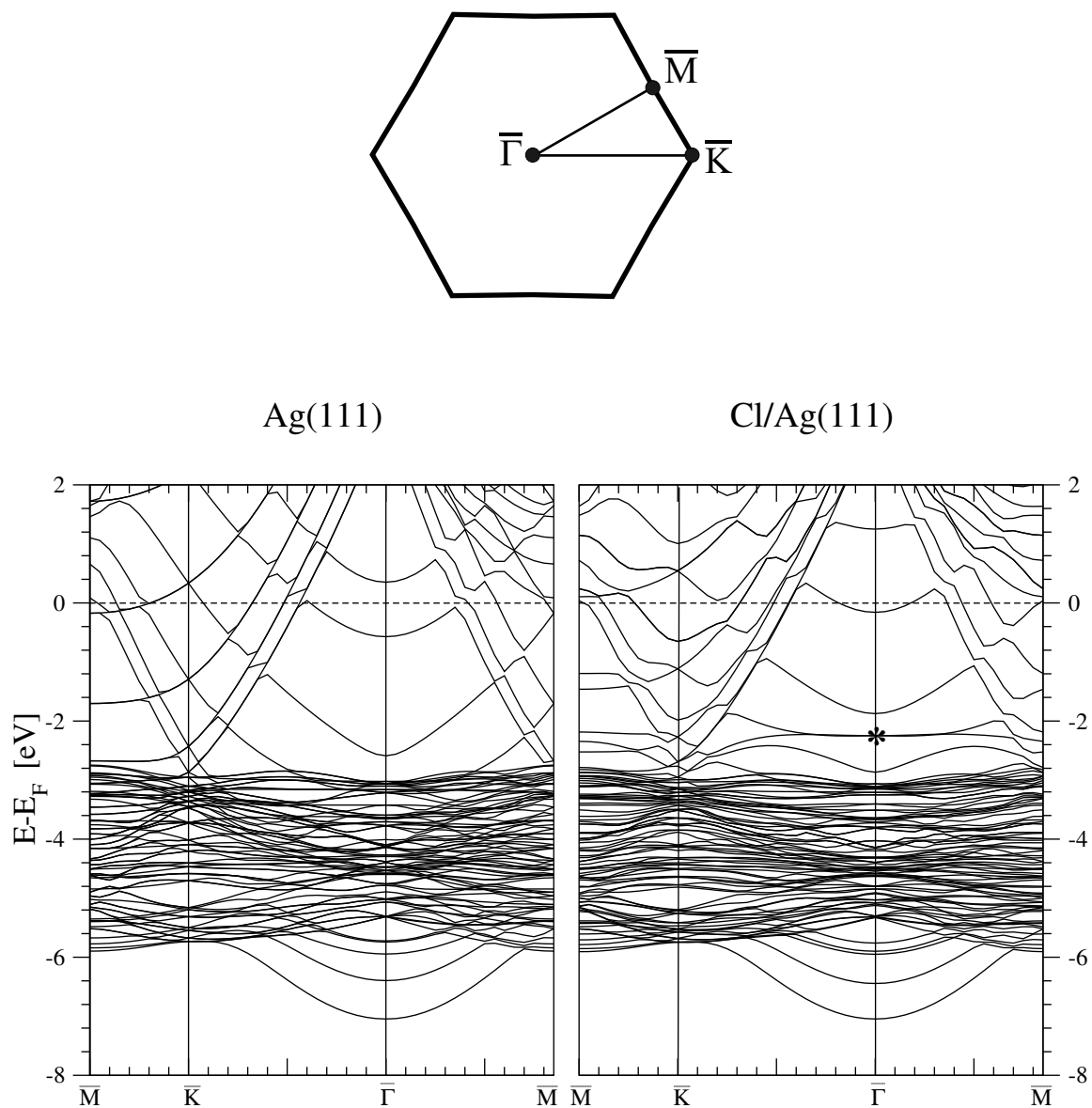
Figure 3.5: Band structure of the clean Ag(111) surface (left) and Ag(111)-Cl (right) in $\sqrt{3} \times \sqrt{3}R30^0$ geometries (Cl 3s-derived states lie distinctly below and are not shown). A chlorine-derived antibonding state is marked by an asterisk *.

chose it to be a simple Gaussian with a dispersion σ:

$$g_\sigma(x) = \frac{1}{\sigma\sqrt{\pi}} e^{-\frac{x^2}{\sigma^2}}. \tag{3.4}$$

$\epsilon_{n,\mathbf{k}}$ in Eq. (3.3) is the Kohn-Sham eigenvalue of the n-th state at the k-point $\mathbf{k}$. DOS difference, $\Delta\mathcal{D}$, is defined as:

$$\Delta\mathcal{D}(E) = \mathcal{D}_{Cl/Ag(111)}(E) - \mathcal{D}_{Ag(111)}(E), \tag{3.5}$$

$\mathcal{D}_{Cl/Ag(111)}(E)$ being the DOS of the adsorbate-covered slab, and $\mathcal{D}_{Ag(111)}(E)$ the DOS of the bare slab. Contrary to $\mathcal{D}$ itself, $\Delta\mathcal{D}$ is not guaranteed to be a non-negative function. However, it integrates to the number of valence electrons on the adatom N_{val} (7 for chlorine):

$$\int_{-\infty}^{E_F} \Delta\mathcal{D}(E)\,dE = N_{val}. \tag{3.6}$$

The DOS and DOS difference for the $\sqrt{3}\times\sqrt{3}R30^0$ and 3×3 structures are shown in Fig. 3.6. In accord with the experimental data of Pasquali *et al.* [7] we see that little chlorine-induced changes occur in th sp-region of the silver DOS (i.e. 2eV below the E_F and above). The main features that appear are (i) an anti-bonding state just above the silver d-states (at about 2.4eV below the Fermi level), which was already identified in Fig. 3.5, and (ii) two bonding states at about 4.5 and 5.8eV below the Fermi level. The overall splitting of the chlorine $3p$-state is more than 4eV, which once again indicates a very strong bonding between the chlorine atom and the silver surface.

Additional insight can be gained from a real-space analysis of the electron density. In the last section of Chapter 2 we introduced density difference plots as powerful tools to analyze the nature of chemical bonds in small molecules. Here we illustrate the usefulness of such analysis in adsorbate-substrate systems. Let $n_{tot}(\mathbf{r})$ be the electron density of the whole system, $n_{sub}(\mathbf{r})$ and $n_{ad}(\mathbf{r})$ the densities of the substrate and adsorbate, respectively. The latter are calculated keeping the atoms fixed in the positions which they assume in the total system (unlike Eq. 3.2). The density difference is defined as

$$\Delta n(\mathbf{r}) = n_{tot}(\mathbf{r}) - n_{ad}(\mathbf{r}) - n_{sub}(\mathbf{r}). \tag{3.7}$$

As in the case of small molecules (Fig. 2.15 in Chapter 2), we expect this function to exhibit specific features of the surface chemical bond. Fig. 3.7 depicts cut of the total density and density difference for the $\sqrt{3}\times\sqrt{3}R30^0$ and 3×3 structures. While little insight can be gained from the total density plots (Fig. 3.7, top), the density difference contour plots are very instructive. First, we conclude right away that some electron charge is transfered from the silver surface (blue color) to the chlorine adatom (red color). This, of course, has to be expected, since chlorine is a very electronegative element. We will quantify this charge transfer below. Second, silver d-states more than sp-states donate the charge, and this conclusion is consistent with the DOS difference (Fig. 3.6). Third, the charge accumulation region on the chlorine atom is most closely related to Cl $3p_{xy}$ states, and this once again is in perfect agreement with the conclusions of Pasquali *et al.* [7]. In contrast, for the smaller adsorbate, oxygen on Ag(111), $2p_z$ rather than $2p_{xy}$ states
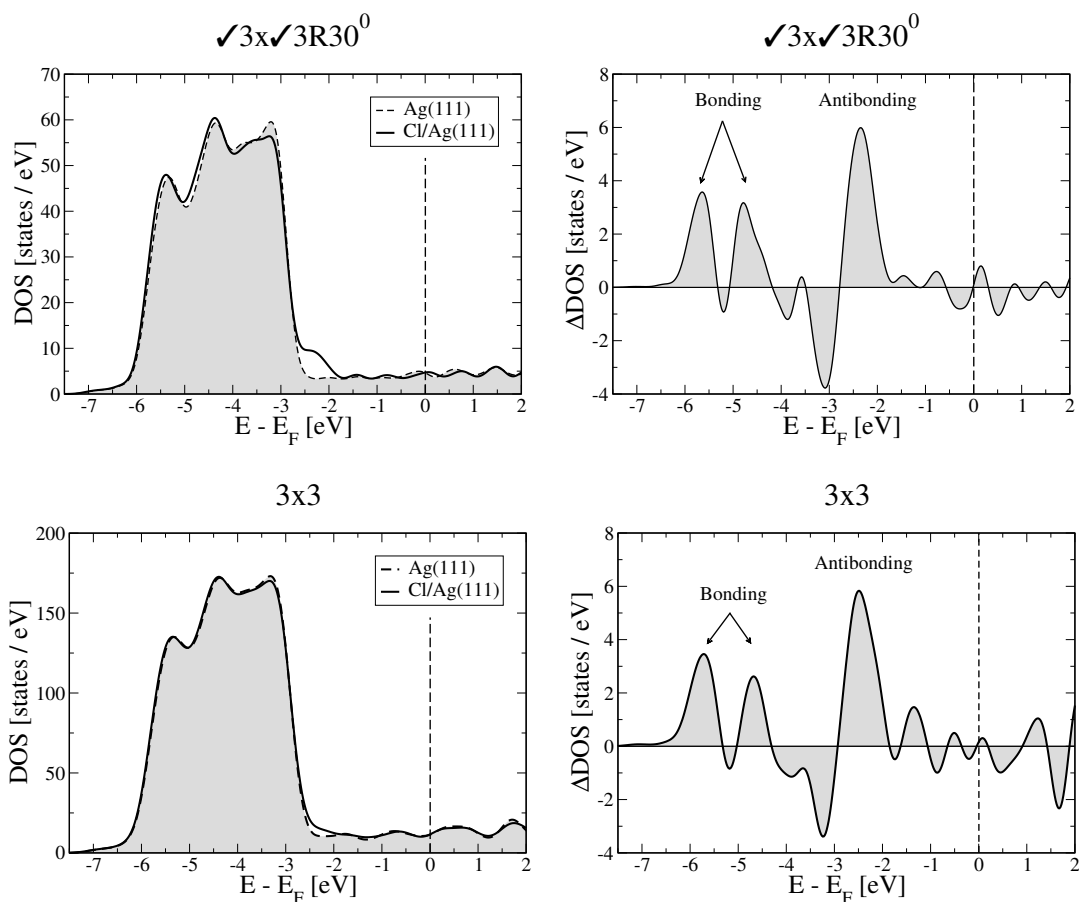
Figure 3.6: Total density of states (left) and the change in density of states (right) induced by chlorine adsorption in a $\sqrt{3} \times \sqrt{3}R30^0$ (top) and 3×3 (bottom) geometries. DOS was calculated using the actual number of k-points employed in the calculation with a Gaussian smearing of 0.17eV. Chlorine 3s-derived bands are not shown.
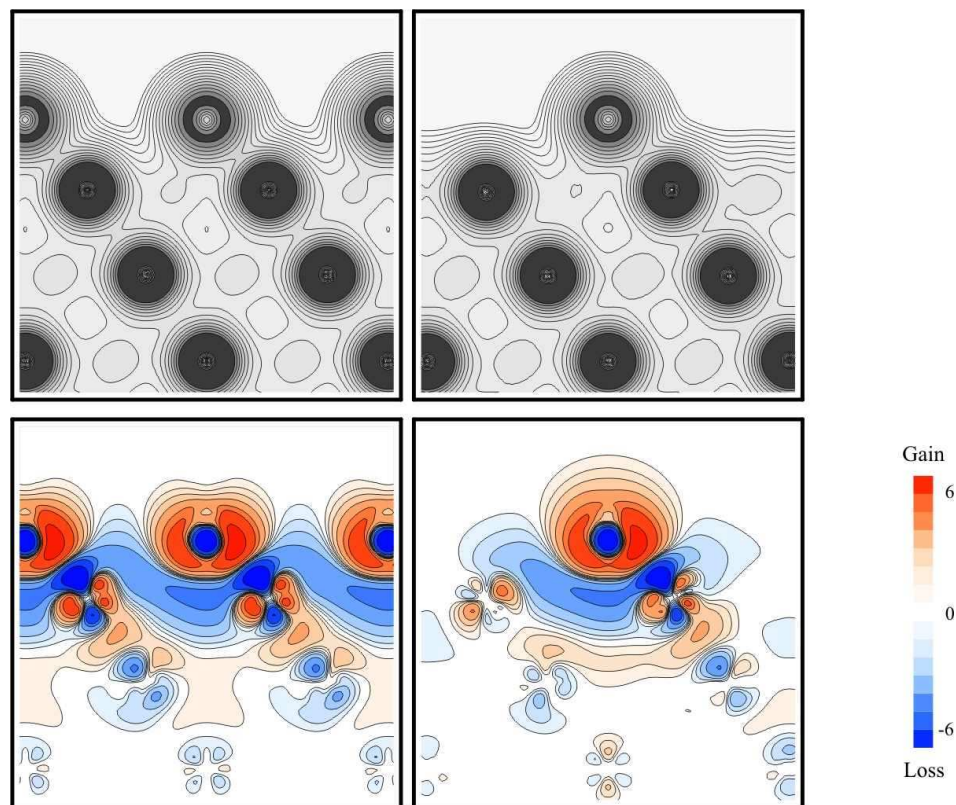
Figure 3.7: Total density (top) and density difference (bottom) for the $\sqrt{3} \times \sqrt{3}R30^0$ (left) and 3×3 (right) structures. In the total density plots contour lines are plotted with a logarithmic scale: the smallest value is $0.02 \mathrm{bohr}^{-3}$, and the subsequent contour line correspond to a density which is bigger by a factor of 1.4. In the density difference plots red regions correspond to electron charge accumulation, blue regions correspond to electron charge depletion and the scale is shown in the legend in the units of bohr^{-3}. The p_{xy} character of the change in charge distribution on the chlorine atom is visible.

acquire more additional electron charge [23]. From all that was said above, Cl-Ag(111) bond can be certainly described as *ionic*.

We can also readily calculate the *xy*-integrated density difference:

$$\Delta n\left(z\right) = \int_{A_{xy}} \Delta n\left(\mathbf{r}\right) dxdy. \tag{3.8}$$

Here, A_{xy} is the area of the surface unit cell ($\sqrt{3}\beta^2 a_0^2/2$ in our case, see Fig. 3.2). This function for the $\sqrt{3} \times \sqrt{3}R30^0$ structure is shown in Fig. 3.8. Changes in the electron density occur only at the interface, and the chlorine-induced perturbation to the electron density is screened beyond the second silver layer. This has to be expected for metals. Another very general and interesting conclusion is that even for such a strong ionic interaction, the change in electron density is but a very small fraction of the total electron density. This is a very well-known but nevertheless amazing, fact: the electron density of usual matter is almost a superposition of atomic electron densities. The word *almost* is crucial here - small deviations from the superposition of the atomic electron densities represent the formation of *chemical bonds*. We can also determine the electron charge on the adsorbate. There are numerous procedures to extract this information. Since partial charges are not observable quantities, all such techniques give only qualitative estimates with relative values being more important than absolute values. We choose the following procedure. One can see in the density difference plot in Fig. 3.8 that there is a plane at z_0 between the substrate and the adsorbate, where Δn is zero. This point almost coincides with the point where $n_{sub}\left(z\right)$ and $n_{ad}\left(z\right)$ are equal. We estimate the charge on the adsorbate as

$$\Delta N = \int_{z_0}^{z_1} \Delta n\left(z\right) dz, \tag{3.9}$$

z_1 being the plane in the middle of the vacuum region where all densities are practically zero. We obtain values $\Delta N = 0.16 \div 0.20$ electrons. Chlorine atoms thus acquire an additional $-0.2e$ charge upon adsorption. Even though this number is less than 1 (which would correspond to a naïve picture of a negatively charge chlorine ion Cl^-), its magnitude is consistent with previous estimates based on a different charge partitioning scheme [19].

Charge transfer from the substrate to the adlayer causes a change in the work function. In Fig. 3.9, left, the *xy*-averaged electrostatic potential

$$V\left(z\right) = \frac{1}{A_{xy}} \int_{A_{xy}} V\left(\mathbf{r}\right) dxdy \tag{3.10}$$

is depicted as a function of the vertical coordinate z for different lateral unit cells. For a clean surface, the work function is:

$$\Phi_m = V\left(\infty\right) - E_F, \tag{3.11}$$

where $V\left(\infty\right)$ is the electrostatic potential in the middle of the vacuum region (practically, at infinity). In the absence of the dipole correction during the self-consistent calculation (Chapter 2), a small electrostatic field is created in the middle of the vacuum region because of periodic boundary conditions in the z direction. This field leads to a linear
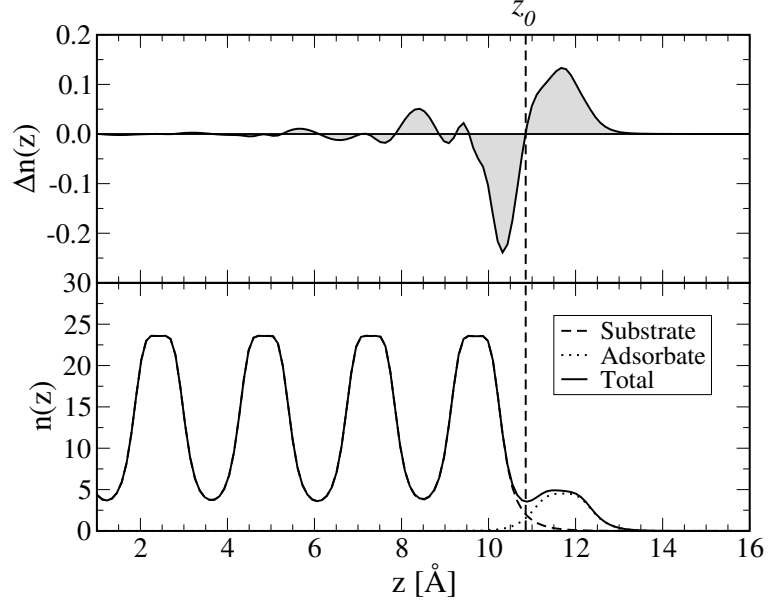
Figure 3.8: *xy*-integrated density (bottom panel) and density difference (top panel) as a function of the vertical coordinate z.

decrease of the electrostatic potential in the vacuum and to a (small, in case of metallic surfaces) electrostatic coupling between the repeated slabs. We approximate the work function for an adsorbate covered surfaces as:

$$\Phi' = V_{max} - E_F, \tag{3.12}$$

where V_{max} is the maximum value of the electrostatic potential close to the adsorbate (where the slope becomes constant). If there is a sufficient vacuum region between the repeated slabs, such a procedure should produce the same work function as the one with the dipole correction. In Fig. 3.9, right, we compare the variations of the electrostatic potential for two values of the vacuum region between the slabs (equivalent to 6 or 8 silver atomic layers, respectively). It can be seen that the vacuum region in those two cases is large enough such that the work functions determined by Eq. (3.12) are converged and would no longer change increasing the vacuum region. It should be said that the dependence of the total energies on the size of the vacuum region is of the order of 1meV for all the unit cells studied and thus does not change our results significantly.

The calculated work function shifts (i.e. $\Delta\Phi = \Phi' - \Phi_m$) as a function of coverage are shown in Fig. 3.10, together with the experimental data, taken from Ref. [6]. A direct comparison between experiment and theory cannot be made because experimental exposure times were not calibrated and the exact physical coverage could not be deduced in the experiment. The general trend, however, is reproduced very well - there is an initial linear increase of the work function upon exposure of chlorine with a tendency to saturate.
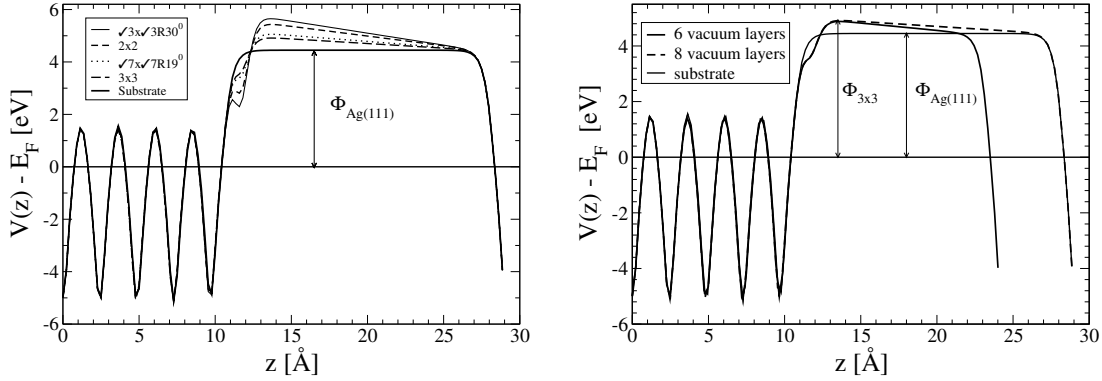
Figure 3.9: xy-averaged electrostatic potential $V(z)$ for bare and chlorine covered silver surfaces. Left, $V(z)$ for Cl/Ag(111) for lateral different unit cells; Right, $V(z)$ for the 3×3 unit cell with two different vacuum layers.

Experimentally, saturation occurs in the chloridation range, which we did not consider in our calculations, with a saturation value $\Delta\Phi \approx +1.5eV$ or $+1.8eV$ according to Ref. [7].

It is straightforward to calculate the vertical adsorption-induced dipole moments from the Helmholtz relation:

$$\mu = \varepsilon_0 A_{xy} \Delta\Phi, \tag{3.13}$$

where A_{xy} again is the area of the surface unit cell. The results are plotted in Fig. 3.11 for both adsorption sites considered. The adsorption-induced dipoles are slightly larger for hcp sites then for fcc sites and decrease when the separation between the laterally repeated adatoms decreases. This is due to a depolarization effect. The periodically repeated dipoles point in the same direction. All the surrounding dipoles create an electric field $\mathcal{E}$ that decreases the dipole moment of a given dipole. If one assumes that each adatom has an effective polarizability α, the dipole moment as a function of the surface lattice constant can be described by the following equation:

$$\mu(d) = \mu_0 \frac{d^3}{d^3 + \alpha T}. \tag{3.14}$$

Here μ_0 is the vertical adsorption-induced dipole moment at infinite separation between adsorbates, d is a surface lattice constant, and T is a 2D lattice sum, which depends on the geometry of the adatom lattice. For a triangular lattice $T \approx 11.034$ [25] (see below the section 'Derivation of the Topping formula'). We obtain the following 'effective' parameters: $\mu_0^{fcc} = 0.86D$, $\mu_0^{hcp} = 0.88D$, $\alpha^{fcc} = 2.8\text{Å}^3$, $\alpha^{hcp} = 3.3\text{Å}^3$. Interestingly, the effective polarizabilities are larger than the polarizability of the isolated chlorine atom $(\alpha = 2.2\text{Å}^3)$, but are quite close to the polarizability of the chlorine ion in ionic crystals $(\alpha = 3.0\text{Å}^3$, as determined in Ref. [26]). This again confirms the ionic nature of the Cl-Ag surface bond.

Having determined the vertical adsorption-induced dipoles (Fig. 3.11) we can estimate the interaction energy between those dipoles. The electrostatic energy per one dipole in
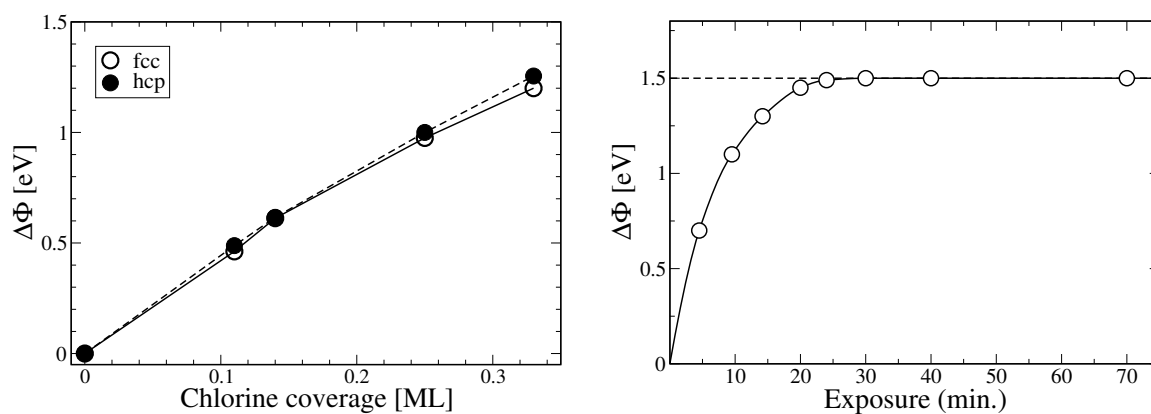
Figure 3.10: *Left*: calculated work function change as a function of chlorine coverage. Empty circles denote work function changes for fcc hollow sites, filled circles denote work function changes for hcp hollow sites. Lines are guide to an eye. Right: measured work function shift as a function of exposure time (from Ref. [6]).

Figure 3.11: Induced vertical dipole moment as a function of surface lattice constant: fcc sites (open circles) and hcp sites (full circles). Line: a fit to a Topping formula with effective parameters.
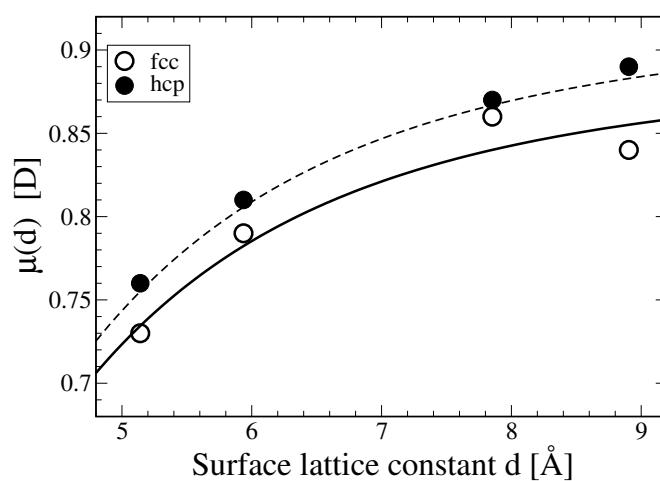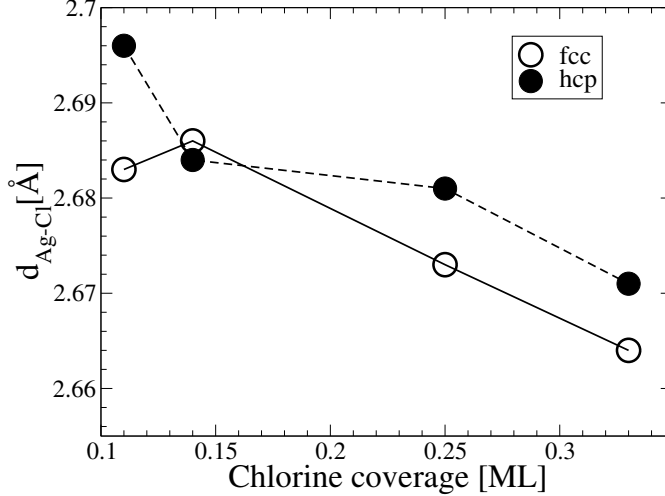
Figure 3.12: Change of the Ag-Cl bond length as a function of chlorine coverage. Filled circles denote bond length for fcp hollow sites, open circles denote bond length fcc hollow sites.

the lattice is given by:

$$E\left(d\right) = \frac{\mu T}{8\pi\varepsilon_0 d^3}.$$ (3.15)

T here is the above introduced lattice sum, and d is again the lattice constant of the lateral supercell. Parallelly oriented dipoles repel each other. Let us calculate this repulsion energy in the $\sqrt{3}\times\sqrt{3}R30^0$ structure, when $d = \sqrt{3}a_0$ as comapared to infinite separation between the adsorbates, $d = \infty$. An evaluation gives $E\left(\sqrt{3}a_0\right) - E\left(\infty\right) \approx 0.03\text{eV}$. Comparing to the variation of the adsorption energies in Fig. 3.4, we see that our estimate is consistent with the *ab-initio* calculated changes in adsorption energy. Therefore these changes should be ascribed to small repulsion between adsorption-induced dipoles.

As a last result, Fig. 3.12 shows the dependence of the Ag-Cl distance on the chlorine coverage. This distance changes very little as a function of coverage, and is about 2.7Å. Small deviations can be attributed to slightly larger lateral and vertical relaxations of the silver substrate with decreasing coverage.

3.4   Derivation of the Topping formula

In this section we will derive the depolarization formula Eq. (3.14). Sometimes it is called the Topping formula, even though only the lattice sum was derived and evaluated by Topping himself [25]. In Fig. 3.13 the hexagonal lattice of polarizable dipoles is depicted. There is a point dipole on each of the lattice points, all dipoles are equivalent and point in the direction perpendicular to the lattice plane. Each dipole has an effective polarizability α' associated with it such that if there is a perpendicular electric field $\mathcal{E}$ at the dipole, the dipole moment is changed by an amount $\Delta\mu = \alpha'\mathcal{E}$. With no external electric field, the dipole moment is μ_0. So let us assume that each dipole in the hexagonal lattice has

a dipole moment μ. The lattice constant (or the nearest neighbour distance between the dipoles) is d. We will now calculate the electric field, created by all other dipoles at the position of the central dipole, which is depicted in black color in Fig.3.13. The Cartesian coordinates of the central dipole are $\{0,0\}$. Unit vectors $\mathbf{a}_1$ and $\mathbf{a}_2$ of the hexagonal lattice are given by:

$$\begin{aligned}
\mathbf{a}_1 &= d\{1,0\}; \\
\mathbf{a}_2 &= d\left\{\tfrac{1}{2}, \tfrac{\sqrt{3}}{2}\right\}.
\end{aligned}$$

The Cartesian coordinates of the lattice point with indices $\{i,j\}$ are given by:

$$\mathbf{r}_{ij} = d\left\{i + \frac{1}{2}j, \frac{\sqrt{3}}{2}j\right\}. \tag{3.16}$$

The partial electric field, created by the dipole $\{i,j\}$ at the site $\{0,0\}$ is:

$$\mathcal{E}_{ij}(r) = -\frac{\mu}{4\pi\varepsilon_0 r_{ij}^3} = -\frac{\mu}{4\pi\varepsilon_0 d^3}\frac{1}{(i^2 + ij + j^2)^{3/2}}. \tag{3.17}$$

The total electric field, created by all the other dipoles at the central site $\{0,0\}$ is the sum of all the partial electric fields $\mathcal{E} = \sum'_{i,j}\mathcal{E}_{ij}$. The prime indicates that the term $i = j = 0$ should be excluded from the sum. Thus we have:

$$\mathcal{E} = -\frac{\mu}{4\pi\varepsilon_0 d^3}\sum_{i,j}\frac{1}{(i^2 + ij + j^2)^{3/2}} = -\frac{\mu T}{4\pi\varepsilon_0 d^3}. \tag{3.18}$$

The sum, appearing in Eq. (3.18), is called a lattice sum, and can be evaluated easily with the help of computer:

$$T = \sum_{i,j}\frac{1}{(i^2 + ij + j^2)^{3/2}} = \sum_{i=1}^{\infty}\sum_{j=0}^{\infty}\frac{6}{(i^2 + ij + j^2)^{3/2}} = 11.034. \tag{3.19}$$

The summation was limited only to one sixth of the plane making use of the symmetry of the system. Interestingly, Topping himself in 1927 evaluated the lattice sum (3.19) by purely mathematical methods, employing the properties of special functions [25].

The electric field at the central dipole $\mathcal{E} = \mu T / (4\pi\varepsilon_0 d^3)$ leads to a depolarization, i.e. the reduction of the dipole moment. Since the same electric field is on all the lattice points, μ in Eqs. (3.17) and (3.18) is already this reduced dipole. Self-consistency condition is thus:

$$\mu - \mu_0 = \alpha'\mathcal{E} = -\frac{\alpha'}{4\pi\varepsilon_0}\frac{\mu T}{d^3}. \tag{3.20}$$

Let us define $\alpha = \alpha' / (4\pi\varepsilon_0)$, which is also a polarizability, but measured in units of Å^3. From Eq. (3.20) we obtain:

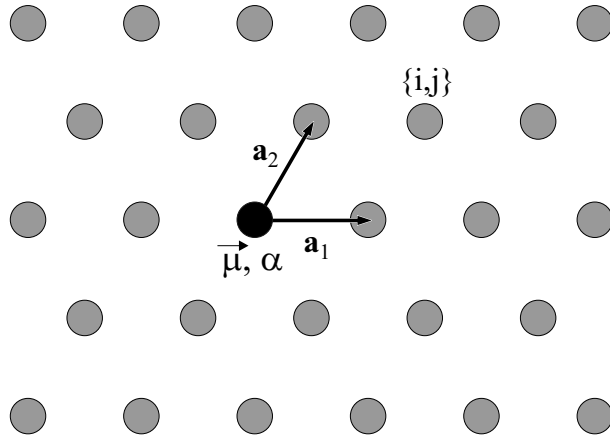$$\mu(d) = \mu_0\frac{d^3}{d^3 + \alpha T}. \tag{3.21}$$

Figure 3.13: Hexagonal lattice of polarizable dipoles.

This equation is the one cited in the previous section and used for the fit in Fig. 3.11. It describes the change of the dipole moment of the dipole in the hexagonal lattice assuming that the effective polarizability α is independent of d. Even though this formula is a classical one, the polarizabilities of chlorine, obtained from the fit, are quite close to the experimental ones.

3.5   Conclusions

In this chapter we have examined a simple surface science system, chlorine adsorbed on the Ag(111) surface. Except for the highly unfavourable 1×1 structure, the adsorption energy depends very weakly on the coverage and is about 2.9eV. Upon adsorption, chlorine atoms acquire about -0.2e charge. A small increase of the adsorption energy with increasing separation between the adsorbates is due to a reduced repulsion between the adsorption-induced dipoles. The analysis of the changes in densities of states, work function increase of adsorbate-covered surfaces and redistribution of electron charge lets us to describe the Cl-Ag bond as *ionic*. Our calculations also show, that fcc hollow site is by $7 - 12$meV more energetically stable than the fcc hollow site. DFT calculations agree nicely with the available experimental data.

Bibliography

[1] M. Bowker and K.C. Waugh, *The adsorption of chlorine and chloridation of Ag(111)*, Surf. Sci. **134**, 639 (1983).

[2] J.G. Serafin, A.C. Liu, and S.R. Seyedmonir, *Surface science and the silver-catalysed epoxidation of ethylene: an industrial perspective*, J. Mol. Catal. A.: Chem. **131**, 157 (1998).

[3] R.M. Lambert, R.L. Cropley, A. Husain, and M.S. Tikhov, *Halogen-induced selectivity in heterogeneous epoxidation is an electronic effect - fluorine, chlorine, bromine and iodine in the Ag-catalysed selective epoxidation of ethene*, Chem. Comm. 1184 (2003).

[4] E.R. Frank and R.J. Hamers, *Chlorine-induced restructuring of Ag(111) films observed by scanning tunneling microscopy*, J. Catal. **172**, 406 (1997).

[5] H. Piao, K. Adib, and M.A. Barteau, *A temperature-programmed X-ray photoelectron spectroscopy (TPXPS) study of chlorine adsorption and diffusion on Ag(111)*, Surf. Sci. **557**, 13 (2004).

[6] K. Wu, D. Wang, J. Deng, X. Wei, Y. Cao, M. Zei, R. Zhai, and Z. Gao, *Chlorine on Ag(111): the intermediate coverage case*, Surf. Sci. **264**, 249 (1992).

[7] L. Pasquali, S. Nannarone, M. Canepa, E.M. Staicu-Casagrande, and V.A. Esaulov, *Chlorine-induced modifications in the electronic structure of Ag surfaces: a metastable deexcitation spectroscopy and photoemission comparative study*, J. Phys.: Cond. Mat. **15**, 3505 (2003).

[8] G.M. Lamble, R.S. Brooks, S. Ferrer, D.A. King, and D. Norman, *Surface structural determination for a weakly ordered and a disordered phase of Cl on Ag(111)*, Phys. Rev. B **34**, 2975 (1986).

[9] J.H. Schott and H.S. White, *Halogen adlyers on Ag(111)*, J. Phys. Chem. **98**, 291 (1994).

[10] J.H. Schott and H.S. White, *Halogen chemisorption on silver(111). Scanning tunneling microscopy of coadsorbed halogen atoms*, Langmuir **10**, 486 (1994).

[11] B.V. Andryushechkin, K.N. Eltsov, V.M. Shevlyuga, and V.Yu. Yurov, *Atomic structure of saturated monolayer on Ag(111) surface*, Surf. Sci. **407**, L33 (1998).

[12] A.G. Shard and V.R. Dhanak, *Chlorine adsorption on silver (111) at low temperatures*, J. Phys. Chem. B **104**, 2743 (2000).

[13] D.E. Taylor, E.D. Williams, R.L. Park, N.C. Bartelt, and T.L. Einstein, *Two-dimensional ordering of chlorine on Ag(100)*, Phys. Rev. B **32**, 4653 (1985).

[14] R.Q. Hwang, E.D. Williams, N.C. Bartelt, and R.L. Park, *Temperature dependence of the phase diagram of Cl/Ag(111)*, Phys. Rev. B **37**, 5870 (1988).

[15] D. Marx and J. Hutter, *Ab initio molecular dynamics: theory and implementation*, in *Modern methods and algorithms of quantum chemistry* (Jülich, 2000); *http://www.cpmd.org*.

[16] A. Alavi, J. Kohanoff, M. Parrinello, and D. Frenkel, *Ab initio molecular dynamic with excited electrons*, Phys. Rev. Lett. **73**, 2599 (1994).

[17] W.T. Pollard and R.A. Friesner, *Efficient Fock matrix diagonalization by a Krylov-space method*, J. Chem. Phys. **99**, 6742 (1993).

[18] S.R. Billeter, A. Curioni, and W. Andreoni, *Efficient linear scaling geometry optimization and transition-state searching for direct wavefunction optimization schemes in density functional theory using plane-wave basis*, Comp. Mat. Sci. **27**, 437 (2003).

[19] K. Doll and N.M. Harrison, *Theoretical study of chlorine on the Ag(111) surface*, Phys. Rev. B **63**, 165410 (2001).

[20] N.H. de Leeuw, C.J. Nelson, C.R.A. Catlow, P. Sautet, and W. Dong, *Density-functional theory calculations of the adsorption of Cl at perfect and defective Ag(111) surfaces*, Phys. Rev. B **69**, 04519 (2004).

[21] L. Jia, Y. Wang, and K. Fan, *Theoretical study of atomic oxygen adsorption on the chlorine-modified Ag(111) surface*, J. Phys. Chem. B **107**, 3813 (2003).

[22] A.G. Shard, C. Ton-That, P.A. Campbell, and V.R. Dhanak, *Site occupancy of chlorine on Cu(111) using normal-incidence X-ray standig waves: the energy difference between fcc and hcp hollow sites*, Phys. Rev. B **70**, 155409 (2004).

[23] W.-X. Li, C. Stampfl, and M. Scheffler, *Oxygen adsorption on Ag(111): a density-functional theory investigation*, Phys. Rev. B **65**, 075407 (2002).

[24] M. Todorova, K. Reuter, and M. Scheffler, *Oxygen overlayers on Pd(111) studied by density functional theory*, J. Phys. Chem. B **108**, 14477 (2004).

[25] J. Topping, *On the mutual potential energy of a plane network of dublets*, Proc. Roy. Soc. London **114**, 67 (1927).

[26] J.R. Tessmann, A.H. Kahn, and W. Shockley, *Electronic polarizabilities of ions in crystals,* Phys. Rev. **92**, 890 (1953).

Chapter 4

Site-selective adsorption of NTCDA on Ag(110)

The present chapter is devoted to density functional theory calculations of 1,4,5,8-naphthalene tetracarboxylic dianhydride (NTCDA for short) adsorbed on the Ag(110) surface. First we review the basic experimental facts about adsorption of NTCDA and of a similar molecule, 3,4,9,10-perylene tetracarboxylic dianhydride (PTCDA for short), on metal surfaces. Then, DFT calculations of isolated PTCDA and NTCDA, and of chemically related 1,4,5,8-naphthalene tetracarboxylic diimide (NTCDI), 3,4,9,10-perylene tetracarboxylic diimide (PTCDI), as well as naphthalene and perylene are presented. These will help rationalize our calculations and to find some general trends. Computational details of our periodic DFT calculations are summarized and the results of the full adsorbate-substrate calculations are presented. This is followed by the analysis of the obtained results. At the end of the chapter, a model explaining the site-selective adsorption of NTCDA on the Ag(110) surface is proposed.

4.1   Experimental results

The atomic structures of NTCDA and PTCDA are shown in Fig. 4.1. NTCDA has a naphthalene aromatic core which is terminated on both sides by two carboxylic anhydride side groups. Similarly, PTCDA has a perylene core which is terminated by the same side groups. Both molecules have a D_{2h} point symmetry. As shown in the next section, despite the difference in size, the electronic structure of isolated NTCDA and PTCDA is rather similar. Both of them possess an electric octupole moment and have strong electron accepting properties. Keeping this similarity in mind, it is justified to compare the behaviour of these two molecules on metal surfaces and to review the experimental results together. In many cases similar behaviour has been proved experimentally. However, there exists much more experimental data for PTCDA than for NTCDA.

Adsorption geometry. Near-edge X-ray absorption fine structure (NEXAFS) measurements have proved that both NTCDA and PTCDA adsorb with their aromatic ring parallel to the surface. In the experiment, absorption is measured with two different polarizations of X-rays. For normal incidence (angle of incidence $\theta \approx 0^0$) the electric
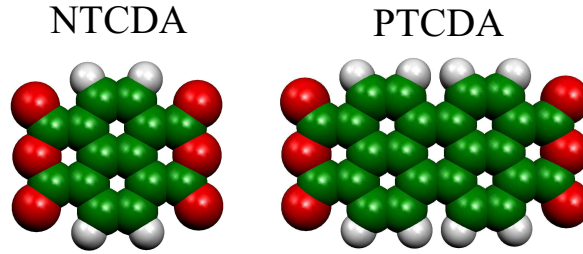
NTCDA   PTCDA

Figure 4.1: Atomic structure of NTCDA and PTCDA. Green spheres - carbon atoms, red spheres - oxygen atoms, white spheres - hydrogen atoms. NTCDA has an aromatic naphthalene core and is terminated by two anhydride side groups at both ends. Similarly, PTCDA has an aromatic perylene core and is terminated by two anhydride side groups at both ends.

field vector is in the surface plane; for grazing incidence ($\theta \lesssim 90^0$) the polarization is (almost) perpendicular to the surface plane. Excitations from the core levels to the π states of conjugated molecules occur only when the electric field vector is perpendicular to the aromatic plane. Thus, comparing the NEXAFS signal for the two limiting angles of incidence, one can tell whether the π-system is parallel or perpendicular to the surface plane. An example of such a measurement is presented in Fig. 4.2, taken from experiments of Gador *et al.* [1, 2, 3]. X-ray absorption was measured for NTCDA adsorbed on silver and copper surfaces, both in multilayer and monolayer regimes. The experimental data shows a drastic increase of X-ray absorption at grazing incidence for a monolayer, hence parallel adsorption configuration. NEXAFS spectra of PTCDA monolayers reveal identical results [4].

Much less is known concerning the local adsorption geometry of the molecules. The lateral registry with respect to the underlying substrate was determined only for PTCDA on the Ag(110) surface. In an elegant STM experiment by Böhringer *et al.* [5], the lateral manipulation of co-adsorbed silver atoms was used to reveal the exact lateral positions of the molecules. Silver atoms can act as markers, since their adsorption sites are well known (Fig. 4.3, (a) and (b)). The local adsorption geometry of PTCDA on Ag(110), determined in this experimental work, is reproduced in Fig. 4.3(c). Most importantly, all oxygens were found to reside almost on top of silver atoms in the $[1\bar{1}0]$ atomic rows.

Lateral order. PTCDA on Ag(111) is a very special system, since it shows a perfect epitaxial growth over extremely long distances [6,7]. Defect-free domains of sizes exceeding 1000Å are quite common [8]. PTCDA molecules form a so-called herringbone pattern on the Ag(111) surface. In this superstructure the molecules are arranged almost like in the (102) planes of the β modification of bulk PTCDA, and this explains the high stability of adsorbed molecular films. On the Ag(110) surface, PTCDA molecules are arranged in the so-called brick-wall structure (Fig. 4.3). This arrangement is alien to bulk PTCDA, and therefore molecular layers on the Ag(110) surface have much worse epitaxial properties,
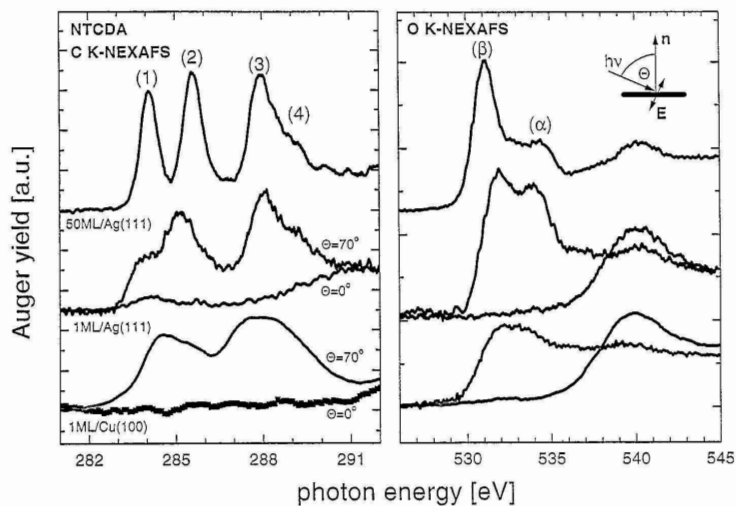
Figure 4.2: Carbon (left) and oxygen (right) K-edge X-ray absorption spectra of NTCDA on metal surfaces for grazing ($\theta = 70^0$) and normal ($\theta = 0^0$) incidence (from Ref. [2]). Comparison of multilayer (top) and monolayer (middle and bottom) spectra show that the π^* LUMO is most affected by interaction with the substrate.
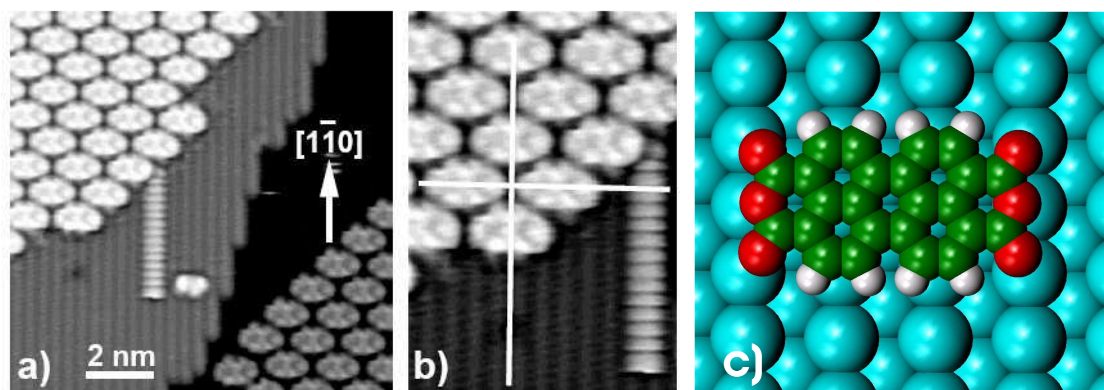

Figure 4.3: (a) and (b) Manipulation of an adsorbed Ag adatom to determine lateral adsorption geometry of PTCDA/Ag(110) (From Ref. [5]). (c) So determined lateral adsorption geometry of PTCDA on the Ag(110) surface. Note that all six oxygens reside almost on top of the silver atoms in the [1$\bar{1}$0] atomic rows underneath.

for example higher defect densities, smaller island sizes, than on the Ag(111) surface.

The lateral ordering of NTCDA on different metal surfaces was investigated by Fink *et al.* [9, 10]. For Ag(001) and Ag(111) surfaces, two phases were found: a low-coverage "relaxed" phase and a high-coverage "compressed" phase. All of them have more than one molecule per surface unit cell. In the "compressed" phases, the area per molecule was found to be $75 - 78\text{Å}^2$. The transition from "relaxed" to "compressed" phases was found to be reversible: upon additional deposition of the molecules, the "relaxed" phase gradually transformed into the "compressed" one; during desorption, the opposite happened. For Cu(001) and Ag(110) surfaces, on the contrary, only one phase of NTCDA was found. Computationally, this is an advantage, since the number of atoms per surface unit cell is smaller. This is one of the practical reasons why NTCDA/Ag(110) was chosen as a model system in the present study. The superstructure of NTCDA on the Ag(110) surface is discussed in more detail in the section "Computational details".

Electronic structure. NEXAFS measurements of Gador *et al.* [2, 1, 3] (see Fig. 4.2) also revealed changes in the electronic structure of the molecules upon adsorption on the surface. The peaks (1), (2) and (4) in the carbon K-edge spectra of multilayers (Fig. 4.2 left, top spectrum) were assigned to excitation from carbons in the naphthalene core. In particular, the peak (1) is due to an excitation to the π^* LUMO of the molecule. This peak decreases substantially in the monolayer (Fig. 4.2 left, middle spectrum), and Gador *et al.* interpreted this as a partial filling of the LUMO state upon adsorption of the molecule. In addition, the peak (2) was shifted by about 0.6eV to lower binding energies due to the interaction with the substrate. On the Cu(100) surface, the LUMO is affected even more (Fig. 4.2 left, middle spectrum). As we will see, theoretical calculations in fact predict that the LUMO is partially filled upon adsorption, too, and thus the conclusions of Gador *et al.* are confirmed by our DFT results. X-ray absorption and ultraviolet photoemission studies of PTCDA overlayers showed that the LUMO of PTCDA is similarly affected by interaction with a metal surface [4, 11].

Intriguing X-ray photoelectron spectroscopy (XPS) results for NTCDA on Ag(111) were published recently by Schöll *et al.* [12]. Interestingly, small but detectable differences were found between the XP spectra of the "relaxed" and the "compressed" super-structures mentioned above. However, due to substantial final state effects, which can be very pronounced in XPS, quantitative conclusions are difficult to draw. XP spectra are significantly changed going from multilayers to monolayers, but it is difficult to extract quantitative information, like the charge state of the molecule, changes in bond lengths, etc.

Adsorption energies. One of the largest differences in adsorption characteristics of PTCDA and NTCDA on noble metal surfaces is the adsorption energy. Experimentally, it can be estimated using the temperature-programmed desorption spectroscopy (TPDS). One slowly raises the temperature of the sample and monitors the amount of molecules desorbed from the surface. Different surface phases identified in diffraction or STM experiments (for instance, the above mentioned "compressed" and "relaxed" phases of NTCDA on Ag(001) and Ag(111)) also reveal themselves as maxima in TPD spectra. TPD measurements of NTCDA on Ag(111) and Ag(001) surfaces show that NTCDA can be desorbed intact from the surface at temperatures $T < 450$K [9, 10]. From the analysis

	T_{des} [K]	E_{ad} [eV]
Ag(001)	430	1.0 ± 0.1
Ag(111)	450	1.1 ± 0.1

Table 4.1: The temperatures of the desorption leading edges and the estimated adsorption energies for NTCDA on the Ag(001) and Ag(111) surfaces. From Refs. [9,10].

of the desorption leading edges, adsorption energies of 1.0eV and 1.1eV were deduced for Ag(001) and Ag(111) surfaces, respectively. The temperatures of the desorption leading edges and estimated adsorption energies are listed in Table 4.1. Interestingly enough, the adsorption energy is larger on the (in general) less reactive Ag(111) surface. The origin of this difference is not known. Unfortunately, no desorption spectra were recorded for the Ag(110) surface, therefore the adsorption energy of NTCDA on the Ag(110) is not known. Keeping in mind that Ag(110) is a more open and more reactive surface, we expect that the adsorption energy is higher on that surface than on Ag(111) or Ag(001).

The situation is completely different for PTCDA. Once adsorbed on the metal surface, PTCDA cannot be desorbed as a whole. Molecular degradation starts before any desorption begins to occur. This means that only molecular fragments can be desorbed from the surface. A clear conclusion is, however, that the adsorption energies of PTCDA on silver surfaces are larger than those of NTCDA, i.e., more than 1eV.

Many more thought-provoking experimental results have been published. As an example, we show in Fig. 4.4 the high resolution electron energy loss (HREELS) spectrum of a PTCDA multilayer, as well as PTCDA and perylene monolayers on the Ag(111) surface [8, 13]. HREELS is a surface-sensitive technique used to measure the vibrational spectrum of the adsorbate layers. Only infrared active modes reveal themselves in the spectra recorded near specular reflections (like in ordinary IR absorption measurements). The spectrum in Fig. 4.4 shows that four intrinsic Raman modes of PTCDA which are silent in the multilayer spectra acquire infrared activity upon adsorption on the Ag(111) surface [14]. An *ab initio* analysis of the electron density redistributions during the vibration of the isolated molecule (Fig. 4.4, bottom) showed that the affected modes are those which involve the largest modulations on the central perylene core. No enhancement of these modes is observed in the monolayer of unsubstituted perylene, however. These findings led the authors to conjecture that the potential reaction center of PTCDA is located on the central part of the perylene core, but the molecule reacts with a metal only when reactive anhydride side groups are attached to the aromatic core. Interestingly, no enhancement of the Raman modes has been seen for PTCDA adsorbed on the Ag(110) surface [15, 16]. The anhydride side groups, however, seem to play an important role in the registry of PTCDA on that surface, too. All these findings raised an interesting question, which we will partly try to answer: why do the anhydride side groups increase the reactivity of the molecule? Two possible mechanisms are illustrated in Fig. 4.5: (a) the anhydride side groups influence the central aromatic part of the molecule (owing to intra-molecular charge transfer) and thus change its reactivity; (b) the side groups react with the substrate directly. We will show that both effects go hand in hand: the side groups
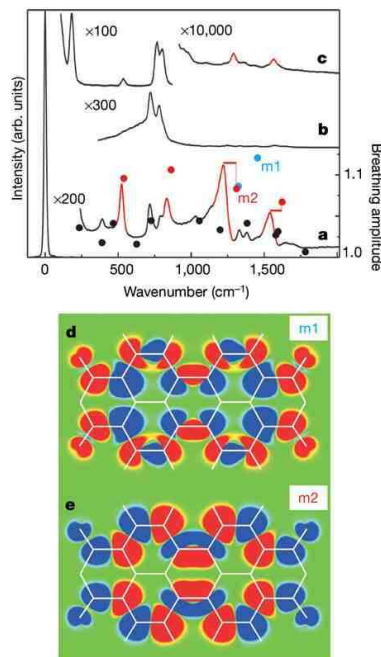
Figure 4.4: Top: High-resolution electron energy loss spectra of perylene and PTCDA adsorbed on Ag(111). (a) 0.3ML of PTCDA, (b) precursor state of 0.3ML of PTCDA, (c) 0.3ML or perylene. Four intrinsic Raman modes (red in (a)) acquire infrared activity upon adsorption of PTCDA on Ag(111). Bottom: DFT calculations have shown that only vibrational modes that modulate the electron density on the central aromatic ring are enhanced. For example, the mode m1 is not enhanced, while the mode m2 is strongly enhanced. From Refs. [8, 13].

increase the electron accepting properties of the molecule, hence charge transfer between the metal and the molecule, and are also responsible for a resulting local electrostatic interaction with the silver substrate.

4.2   DFT calculations of isolated molecules

Before presenting the results for NTCDA adsorbed on the Ag(110) surface, we discuss DFT calculations for isolated NTCDA, PTCDA, as well as chemically related species: naphthalene, NTCDI, perylene and PTCDI. These calculations show, that one of the biggest differences between naphthalene, on one hand, and NTCDA or NTCDI, on the other, is that the latter molecules are strong electrons acceptors. Likewise, PTCDA and PTCDI are electron strong acceptors as compared to perylene. The calculations in this section were performed with the Gaussian 03 program package.

In Fig. 4.6 surface plots of electrostatic potentials of NTCDA and PTCDA molecules are presented. Red (blue) color corresponds to negative (positive) electrostatic potential regions. We see that the electron charge distribution inside the isolated molecules is very
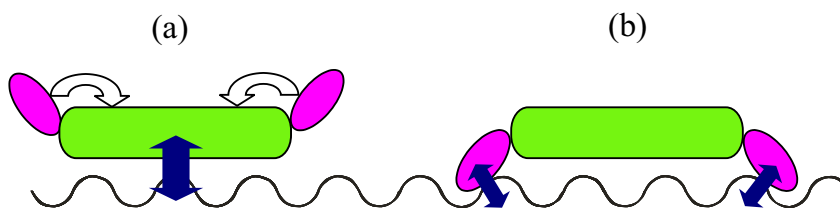
Figure 4.5: Two possible effects of the side groups (red ellipses) on adsorption properties of an aromatic molecule (green square) on a metal surface (represented by a periodically varying potential): (a) intra-molecular charge rearrangement increases the reactivity of the central aromatic core; (b) direct bonding to the surface via the side groups.
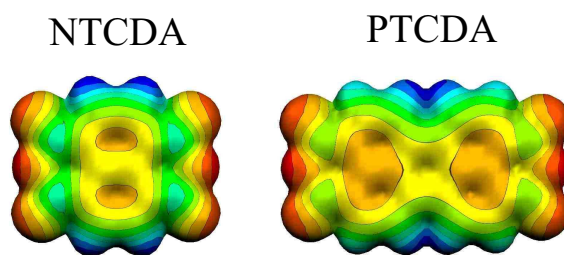

Figure 4.6: The electrostatic potential plots for the NTCDA (left) and PTCDA (right). Red color corresponds to negative, blue color corresponds to positive electrostatic potential regions.

similar despite the difference in size: the peripheral anhydride side groups carry some negative charge, while the central aromatic core is effectively positively charged.

Let us take a closer look at molecular orbitals of the molecules. In Fig. 4.7 the molecular structures of naphthalene, NTCDI and NTCDA, together with 3D images of the frontier Kohn-Sham orbitals are shown. All three mentioned molecules belong to the D_{2h} symmetry group. The LUMOs of both NTCDI and NTCDA have a b_{1g} symmetry, like the LUMO of naphthalene (Fig. 4.7). These orbitals are of the π type, are mostly located on the aromatic part, and exhibit common features in all three molecules. As already mentioned in the previous section, the LUMO of NTCDA plays an important role in the adsorption process.

The situation is a little bit different with the highest occupied molecular orbitals (HOMOs). The HOMOs of both NTCDI and NTCDA (Fig. 4.7) have a b_{3g} symmetry and are of the σ type. These orbitals have largest weights on the p_{xy} atomic states of the peripheral carboxyl oxygens. The π-type orbitals which are related to the HOMO of naphthalene lie energetically slightly below. In fact, we found that the order of those energetically nearly-degenerate highest occupied orbitals are reversed when using other density functionals (for example, hybrid density functional like B3LYP).
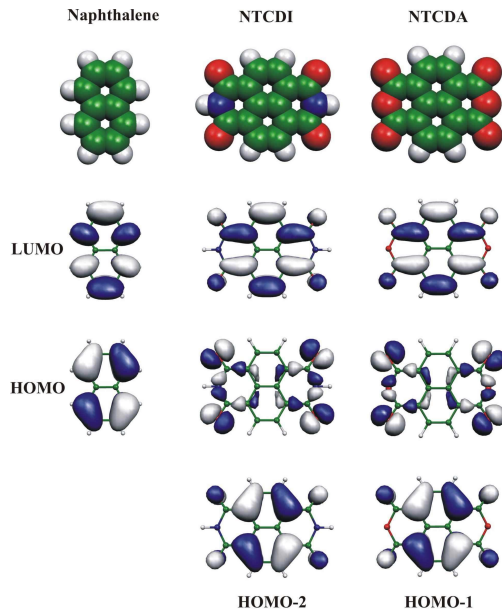
Figure 4.7: The molecular structure (top) and frontier molecular orbitals (bottom) of naphthalene (left), NTCDI (center) and NTCDA (right).

In Fig. 4.8 the Kohn-Sham spectra of the three molecules are shown. The energy positions of the occupied orbitals are indicated with blue horizontal lines, while those of unoccupied orbitals are indicated with red horizontal lines. Inspection of the spectra reveal that the energy positions of the HOMOs and LUMOs of NTCDI and NTCDA are shifted downwards by about 2eV as compared to those of naphthalene. A useful quantity in the forthcoming analysis is the mid-gap position, defined as:

$$\mu = \frac{1}{2}\left(\varepsilon_{HOMO} + \varepsilon_{LUMO}\right), \qquad (4.1)$$

where ε_{HOMO} and ε_{LUMO} are the Kohn-Sham eigenenergies of the HOMO and the LUMO orbitals, respectively. The mid-gap positions are indicated by dashed horizontal lines in Fig. 4.8. More correctly, the mid-gap position of each molecule can be determined via the equation:

$$\mu' = -\frac{1}{2}\left(\text{IP} + \text{EA}\right). \qquad (4.2)$$

Here, IP and EA denote the ionization potential and electron affinity, respectively. Perdew and Levy showed that even though the Kohn-Sham eigenvalues have no direct physical meaning, but the mid-gap position calculated by using Eq. (4.1) should be equal to that calculated using Eq. (4.2) for an exact density functional. The Kohn-Sham spectra in Fig. 4.8 are functional-dependent, the mid-gap positions are much less so. The calculated mid-gap position of NTCDI is 1.7eV lower than that of naphthalene, and the mid-gap position of NTCDA is 2.2eV lower than that of naphthalene. The negative of μ' (defined in Eq. (4.2)) is called absolute electronegativity in chemistry, and was introduced by Mulliken in 1935 [17]. The larger the electronegativity (or the lower the mid-gap position),
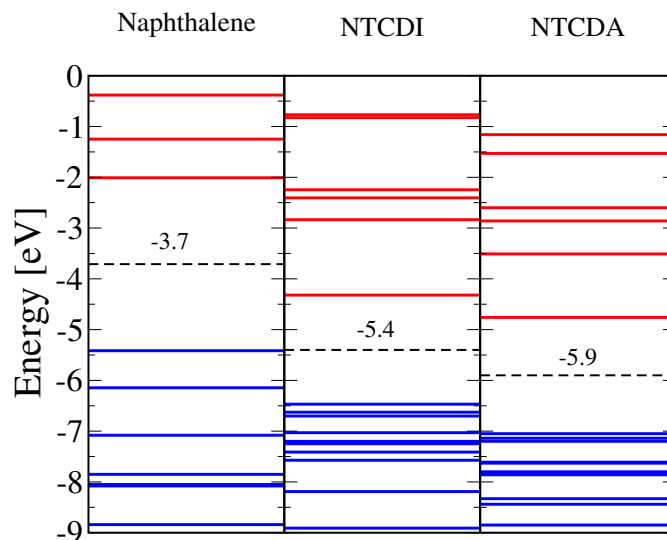
Figure 4.8: The Kohn-Sham spectra of naphthalene (left), NTCDI (center) and NTCDA (right). The occupied states are indicated with blue horizontal lines, the unoccupied ones with red horizontal lines. Mid-gap positions, defined in Eq. (4.1) are indicated by dashed lines.

the stronger the electron accepting properties of the molecule. Judging just from Fig. 4.8 we can expect that NTCDI and NTCDA are much stronger electron acceptors than naphthalene. In fact, this is a well known and documented fact in the chemistry literature [18]. Remarkably, this conclusion can be drawn based solely on DFT calculations for *isolated* molecules. In the next section we show that charge transfer occurs for NTCDA adsorbed on the Ag(110) surface, and the sign of the charge transfer is fully consistent with the high electronegativity of the NTCDA molecule.

Very similar results are obtained for isolated perylene, PTCDI, and PTCDA. The frontier orbitals of the molecules are closely related to each other and exhibit common features (Fig. 4.9). All HOMOs have a a_u symmetry, and all LUMOS have a b_{1g} symmetry. The eigenvalues are different, however (Fig. 4.10). As in the previous case, the HOMOs and the LUMOs of PTCDI and PTCDA are shifted downwards in energy compared to perylene. The mid-gap positions of PTCDI and of PTCDA are 1.5eV and 1.9eV lower than those of perylene. Thus, similar to NTCDI and NTCDA, both PTCDI and PTCDA are strong electron acceptors.

4.3 Computational details

The DFT calculations presented in this chapter were performed with the ABINIT code [19], developed by X. Gonze and collaborators. The ABINIT community is very active and new versions of the code appear on a regular basis. New features, reflecting state-of-the-art achievements in electronic structure theory, are constantly being implemented in the code.

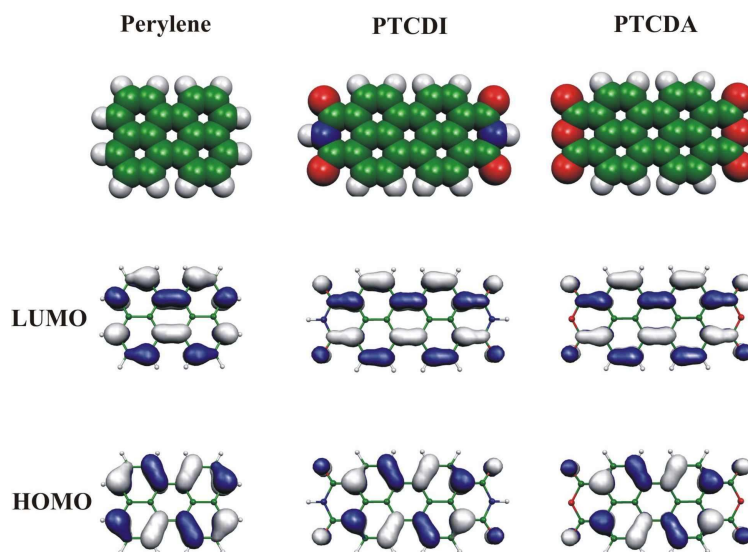Figure 4.9: The molecular structure (top) and frontier molecular orbitals (bottom) of perylene (left), PTCDI (center) and PTCDA (right).

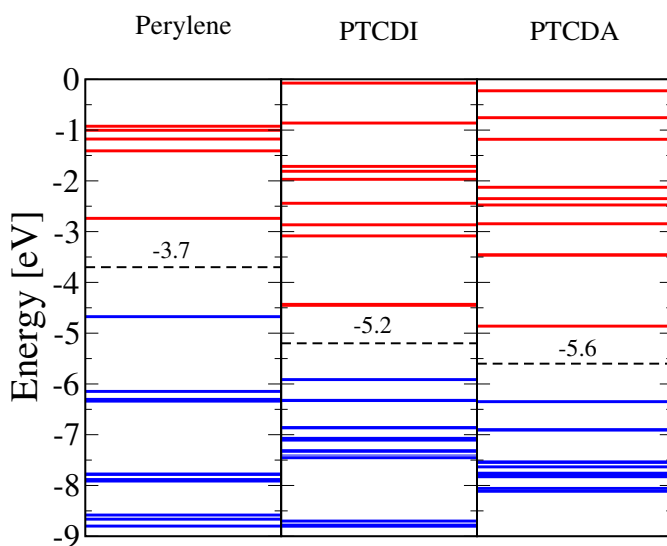

Figure 4.10:   The Kohn-Sham spectra o perylene (left), PTCDI (center) and PTCDA (right). The occupied states are indicated with blue horizontal lines, while the unoccupied ones with red horizontal lines. Mid-gap positions, defined in Eq. (4.1) are indicated by dashed lines.
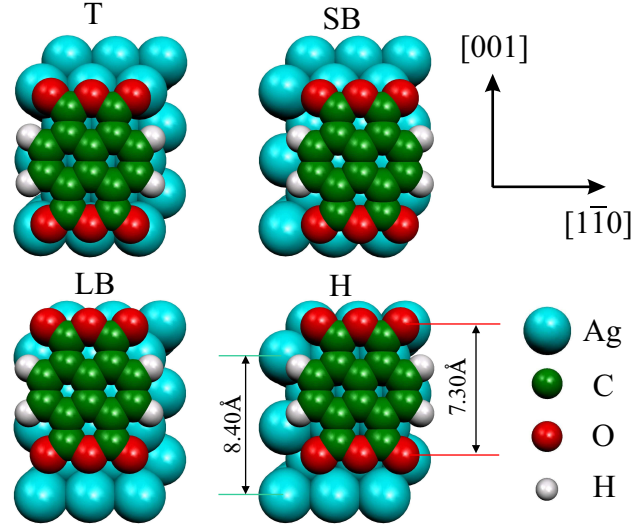
Figure 4.11: Local adsorption geometries studied: T (top), SB (short bridge), LB (long bridge) and H (hollow). The names refer to the position of the midpoint of the central C=C bond with respect to the underlying Ag(110) surface.

As in Chapter 3, we used a slab approach to mimic the adsorption on the Ag(110) surface. The same Troullier-Martins pseudopotentials as in the case of Cl/Ag(111) were used to treat the core states of silver, while dual-space Goedecker-Tetter-Hutter pseudopotentials were used to describe the light atoms H, C and O. Four local adsorption geometries of NTCDA/Ag(110) were studied (Fig. 4.11). We label them according to the position of the mid-point of the central C=C bond: top site (T), short-bridge site (SB), long-bridge site (LB) and hollow site (H). The molecules were oriented with their long axes along the [001] direction of the Ag(110) substrate. In addition to the four local adsorption sites, we considered two different lateral periodicities for the energetically most favourable T site. The periodic arrangement of the molecules, the unit cells and lattice vectors are shown in Fig. 4.12. The first lattice (on the left) is conveniently described by the matrix

$$\mathbf{M}_1 = \begin{pmatrix} 3 & 0 \\ 0 & 3 \end{pmatrix}, \tag{4.3}$$

and the second by the matrix

$$\mathbf{M}_2 = \begin{pmatrix} 3 & 0 \\ -1 & 3 \end{pmatrix}. \tag{4.4}$$

The adsorption energies in both of these lateral arrangements were found to be almost equal, even though only the second superstructure has been experimentally observed [10]. This happens, most probably, because local implementations of DFT (like LDA and GGA) fail to account for long-range van-der-Waals interactions, which are presumably responsible for favouring superstructure $\mathbf{M}_2$ over superstructure $\mathbf{M}_1$. From now on, all the presented results apply to the superstructure $\mathbf{M}_1$ (Fig. 4.12, left).
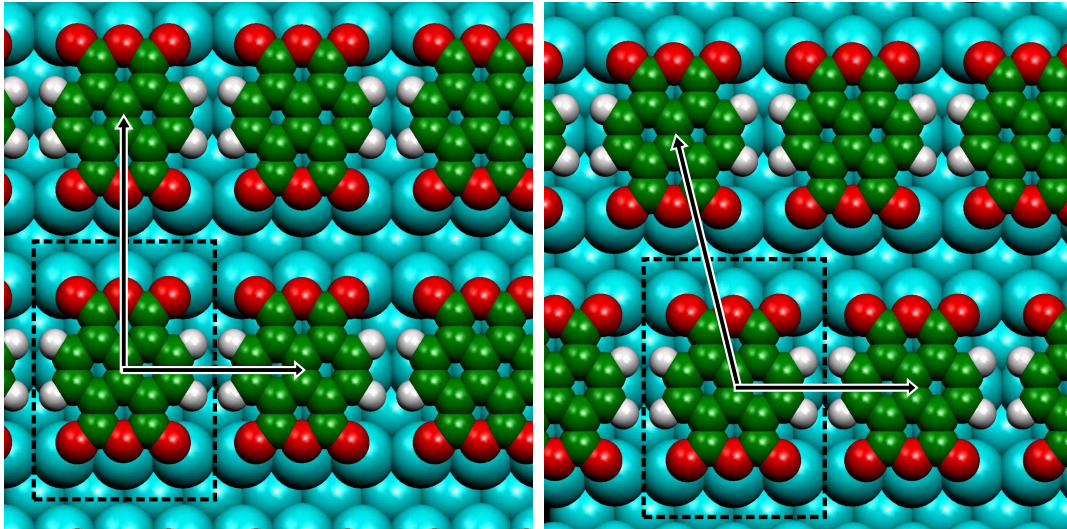
Figure 4.12: Two superstructures of NTCDA/Ag(110): (30/03) (left) and the experimentally found (30/13) (right).

The system we study is already quite large, and therefore we strived to reduce the overall computational time by pursuing the following computational strategy: the kinetic energy cutoff was first set to 50 Ry; a Monkhorst-Pack mesh of $4 \times 3 \times 1$ (producing 4 special k-points) in conjunction with a Fermi smearing of 0.01Ha was used for the Brillouin zone integration; the three topmost silver layers as well as all molecular degrees of freedom were allowed to relax; at first, the geometry of the system was pre-optimized using a four-layer silver slab and a small vacuum region between the slabs; afterwards, the vacuum region was increased to a thickness equivalent to seven metal layers, and a fifth silver layer was added to the metal slab; the geometry was then optimized to reduce the maximum force below threshold of $1 \cdot 10^{-3}$a.u. The damped molecular dynamics methods was employed for the geometry optimization, and the parameters of the optimizer were adjusted in subsequent runs. In Fig. 4.16, the evolution of the total energy (top panel), and the maximum force (bottom panel) are shown as a function of iteration number. More than 100 iterations (about 3 months of computational time) were needed to converge the residual forces. The initial choice of the geometry optimization parameters was unfortunately not optimal in the first sequence of runs. After the residual forces had converged, a sixth silver layer was added to the slab, the vacuum region was increased to a thickness equivalent to nine metal layers, and Brillouin zone integration was made using a finer $6 \times 4 \times 1$ Monkhorst-Pack mesh (6 special k-points). Such a computational setup was used for the final total energy calculations, the results of which are presented in the next chapter. The residual forces even decreased slightly after this procedure and were in all cases below 10^{-3}a.u. The convergence with respect to the basis set was checked using the previously described 5-layer slab and 4 special k-points. The cutoff was increased to 60 Ry and 70 Ry, and the geometry was optimized again. Only intra-molecular bond lengths were slightly affected. Fig. 4.13 shows the dependence of the total energy and the maximum force as a function of geometry optimization iteration for the 60 Ry run. Less
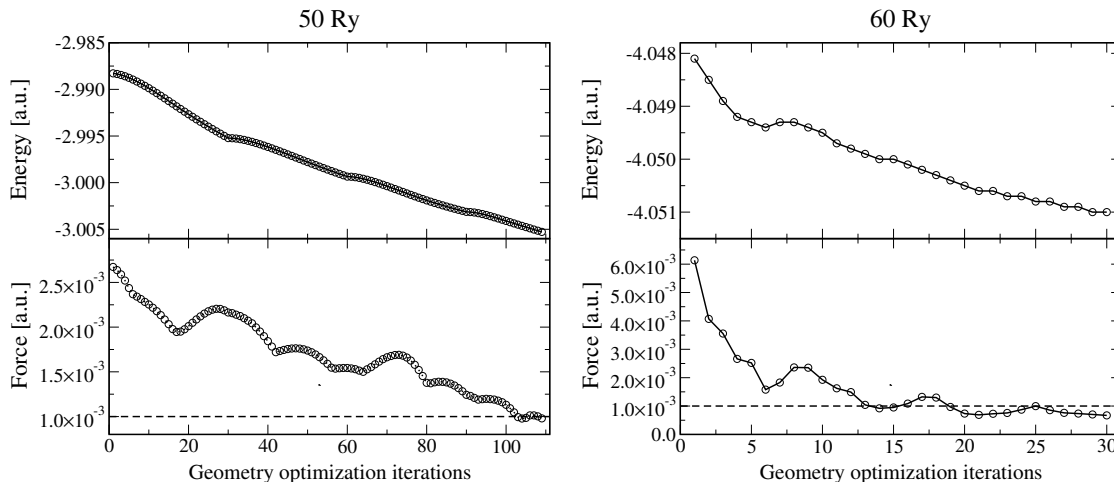
Figure 4.13: Example of geometry optimization runs for the 50 Ry (left) and 60 Ry (right) cutoff. Top panels - total energies (only four significant digits are shown), bottom panel - maximum force. The energy was considered converged when the maximum force F_{max} was below $1 \cdot 10^{-3}$a.u.

than 30 iterations were needed to converge the residual forces, which shows that in this case the choice of parameters was much better than in the case of the 50 Ry run.

4.4   Results and discussion

The adsorption energies of NTCDA at four adsorption sites were calculated using the previously discussed relation:

$$E_{ad} = -\left(E_{tot} - E_{sub} - E_{mol}\right), \tag{4.5}$$

where E_{tot} is the total energy of the slab, E_{sub} is the total energy of the isolated substrate, E_{mol} is the total energy of the molecule. The latter can be computed either for an isolated molecule in a large computational box, or for a molecule in a free standing monolayer with the same lateral periodicities as the full system. It turns out, that if we calculate the energy per one molecule in a free standing monolayer, it is 0.37eV higher than for an isolated molecule. However, the first choice is more suitable for comparison with experiment. We obtained the following adsorption energies: 0.92eV for the top site, 0.44eV for the SB site, and small and slightly negative values (unfavourable adsorption) for the LB and H sites. DFT clearly predicts the T site to be the most energetically favourable. In this configuration all six peripheral oxygens reside almost on-top of silver atoms in $[1\bar{1}0]$ atomic rows (Fig. 4.11). This fact is consistent with the STM results of Böhringer *et al.* [5] for the most stable configuration of PTCDA adsorbed on the Ag(110) surface (Fig. 4.3c). The second most stable configuration is the SB site, and in this case the oxygens reside between the silver atoms in the $[1\bar{1}0]$ rows. For the most unfavourable sites, LB and H, oxygen atoms are between those atomic rows. These results strongly suggest an involvement of peripheral oxygens in the site-selective adsorption.

	T	SB	LB	H
E_{ad} [eV]	0.92	0.44	−0.05	−0.10
ΔN [electrons]	0.38	0.37	0.35	0.34

Table 4.2: Adsorption energies E_{ad} and extra electron charge ΔN for the four local adsorption sites.
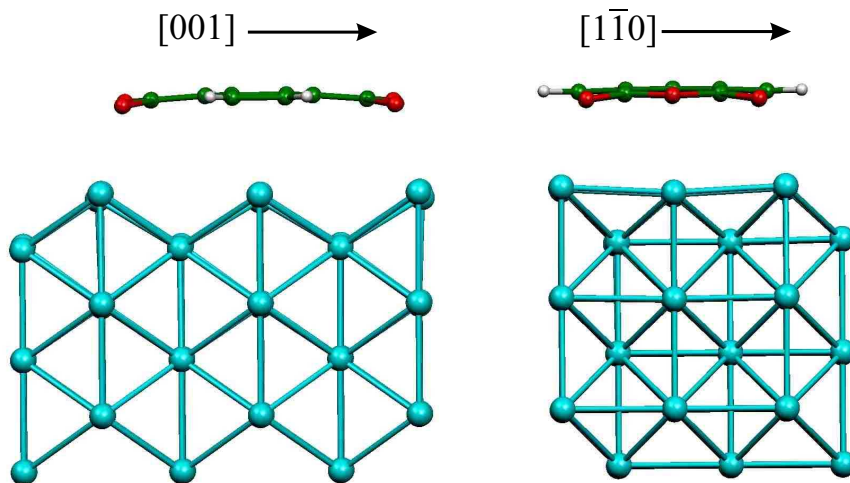

Figure 4.14: Side views of NTCDA in the T position the final relaxed geometry: left, a view along the $[1\bar{1}0]$ direction; right, a view along direction $[001]$ direction.

During the geometry optimization, we observed a bending of the initially flat NTCDA molecule when adsorbed in the energetically favourable T and SB sites. The anhydride side groups, carboxyl oxygens in particular, moved closer to the substrate than the naphthalene core. Side views of the NTCDA adsorbed in the T positions, viewed along the $[1\bar{1}0]$ and $[001]$ directions of the substrate are shown in Fig. 4.14. The bending of the molecule is easily seen. A similar bending of PTCDA on the Ag(111) surface has been recently observed experimentally by Hauschild *et al.* [20] using normal incidence X-ray standing wave technique (NIXSWS) and explained by DFT calculations. In contrast to our work, these authors did not consider the site-selective aspects of the adsorption. Nevertheless, the results of that study are remarkably similar to our results: peripheral oxygens reside closer to the substrate than the aromatic core.

To understand the obtained results in detail, let us first analyze the electron density of the full substrate-adsorbate system. In Fig. 4.15 the total electron densities, averaged over the $[1\bar{1}0]$ and $[001]$ directions are presented. Except for the above-mentioned bending of the molecule, which is also reflected in the total electron density, little insight can be gained from these plots, since, similar to the case of Cl/Ag(111) (Chapter 3), the electron density is almost a superposition of the electron densities of the adsorbate and the substrate. The density difference plots are much more insightful. Again, density difference function is

defined as:

$$\Delta n = n_{tot} - n_{sub} - n_{mol}. \tag{4.6}$$

We expect that similarly to the case of H_2 molecule (Chapter 2) or Cl/Ag(111) (Chapter 3), this function contains useful information about the physical origin of the interaction between NTCDA and the Ag(110) surface. The averages of Δn over the same two directions are shown in Fig. 4.16 for the four adsorption sites. Red colour indicates electron charge accumulation regions, blue colour indicates electron charge depletion regions. We clearly see that NTCDA acquires some additional electron charge upon adsorption on the surface and that the silver atoms in the topmost metal plane become slightly positively charged. Also plotted in Fig. 4.16 is the xy-integrated electron charge density difference

$$\Delta n\left(z\right) = \int_{A_{xy}} \Delta n\left(\mathbf{r}\right) dx dy. \tag{4.7}$$

As in the Cl/Ag(111) case, we quantify the net electron charge on the molecule as

$$\Delta N = \int_{z_0}^{z_1} \Delta n\left(z\right) dz, \tag{4.8}$$

where, again, z_0 is plane between the molecule and the metal, where $\Delta n\left(z_0\right) = 0$, and z_1 lies in the middle of the vacuum region where all densities are practically zero. The calculated values are summarized in Table 4.2 together with adsorption energies. They all amount to about 0.4 electrons and are slightly larger for the T and SB sites than for the H and LB sites. For the most favourable T site, the electron densities $n\left(z\right)$ of the total system, the bare substrate, the adsorbate and the density difference $\Delta n\left(z\right)$ (4.7) are compared in Fig. 4.17. The density difference is but a small fraction of the total valence electron density, as we have already witnessed in Chapter 3.

The inspection of the 3D surfaces of the density difference function leads to the conclusion that the electron charge accumulation regions are most closely related to the LUMO of the isolated molecule. To demonstrate this, we present a cut of the density difference function in a plane about 0.5Å below the molecule when it is adsorbed in the T configuration (Fig. 4.18), together with the frontier orbitals of isolated NTCDA. There is a striking resemblance between this density difference cut and the LUMO of the molecule. Reviewing the experimental results in the first section of this chapter we mentioned the NEXAFS results of Gador $et\ al.$ [2,1,3] which showed a partial filling of the LUMO upon adsorption on the Ag(111) surface (Fig. 4.2). Our calculations nicely agree with this conclusion: we show that the same happens upon adsorption on the Ag(110) surface. The charge transfer from the metal to the molecule is also consistent with the estimated high electronegativity of NTCDA (Fig. 4.8). The chemical potential of NTCDA is approximately equal to the mid-gap position, i.e., $\mu_{NTCDA} \approx -5.9$eV. The chemical potential of the Ag(110) surface, referred to the vacuum level, i.e. electrostatic potential far from the surface, is $\mu_{Ag(110)} \approx -4.2$eV (Fig. 2.11 in Chapter 2). Thus $\mu_{NTCDA} < \mu_{Ag(110)}$ and a net electron transfer from the metal to the molecule is expected.
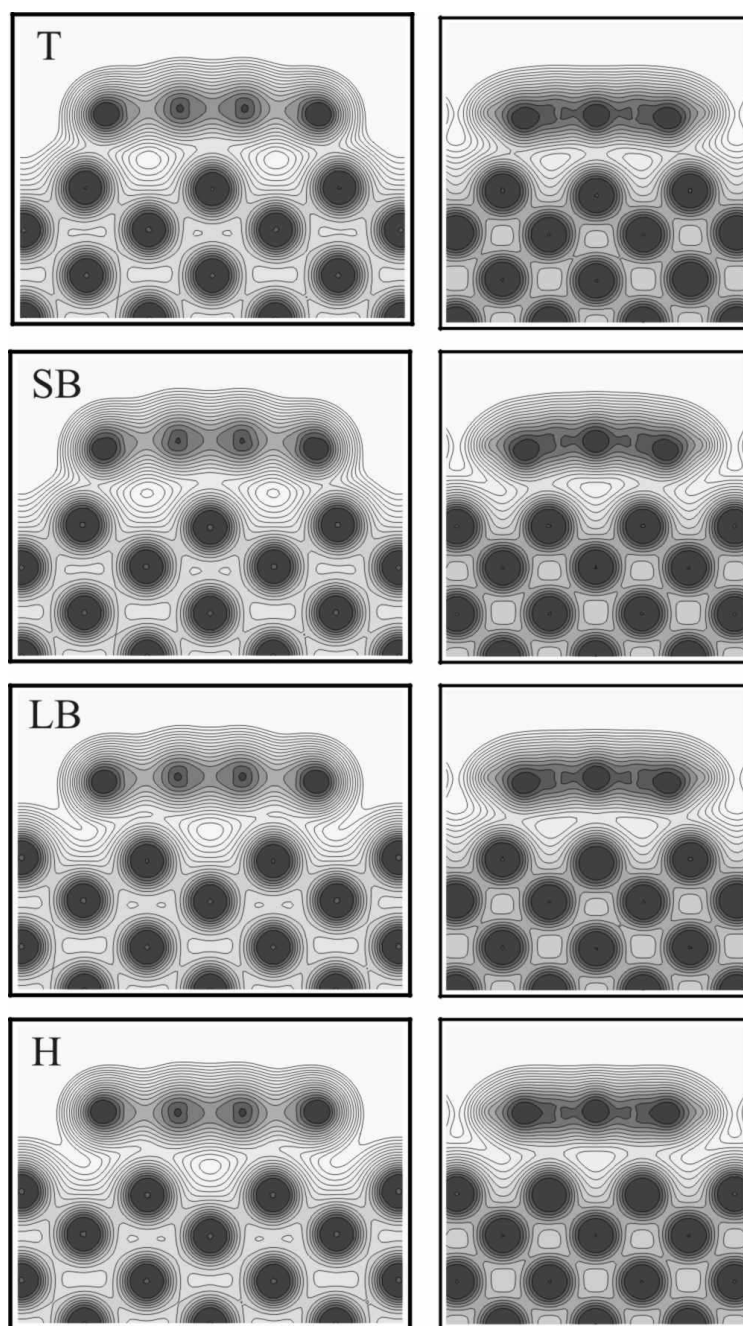
Figure 4.15: Total density for all four adsorption sites. Left column: averages over the [1$\bar{1}$0] direction. Right column: averages over the [001] direction.

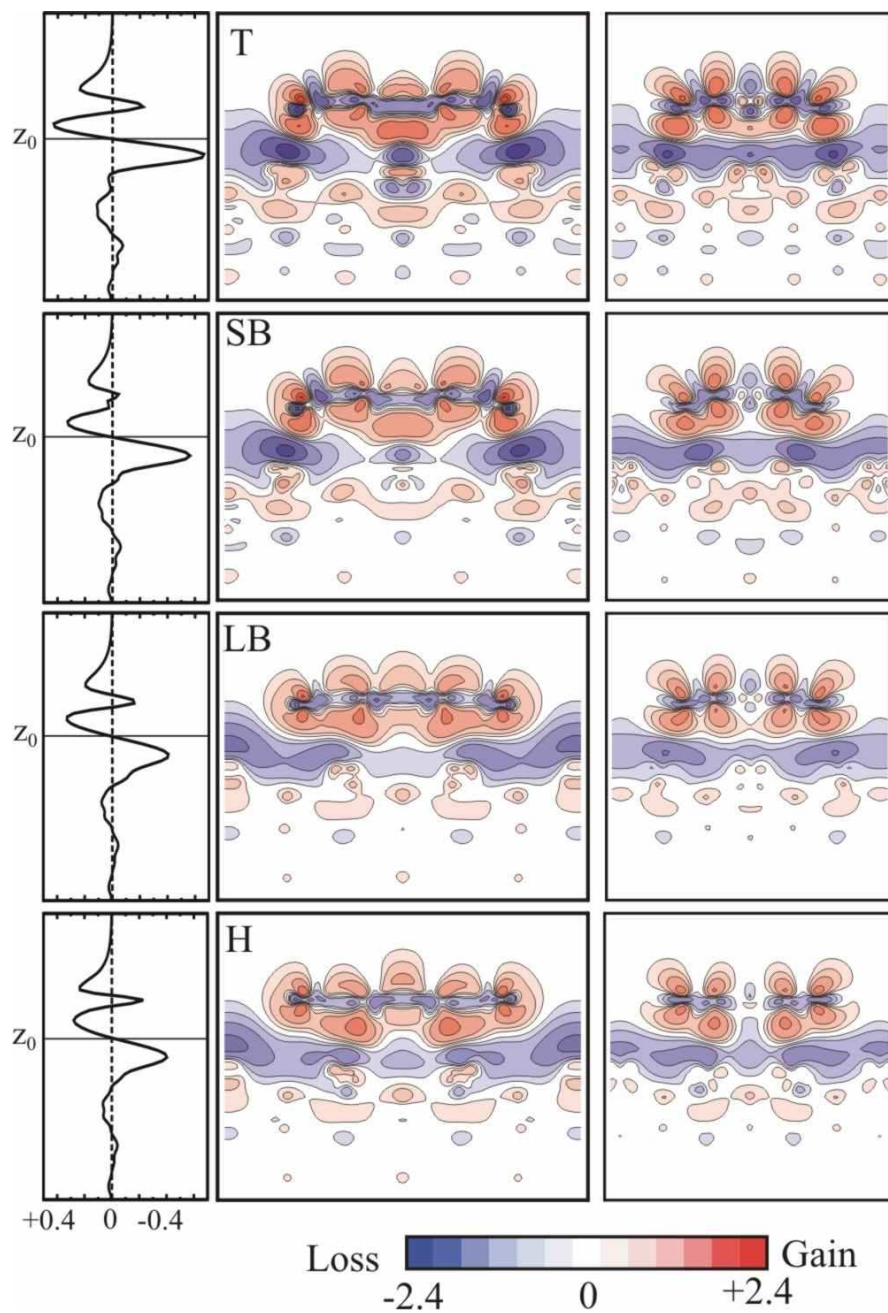Figure 4.16: Density differences for all four adsorption sites. Left column: xy-integrated densities (the units are $e \cdot \text{Å}^{-1}$). Central column: Averages over the $[1\bar{1}0]$ direction. Right: Averages over the $[001]$ direction. For the latter two the units in the color legend are $10^{-2}e \cdot \text{Å}^{-3}$.
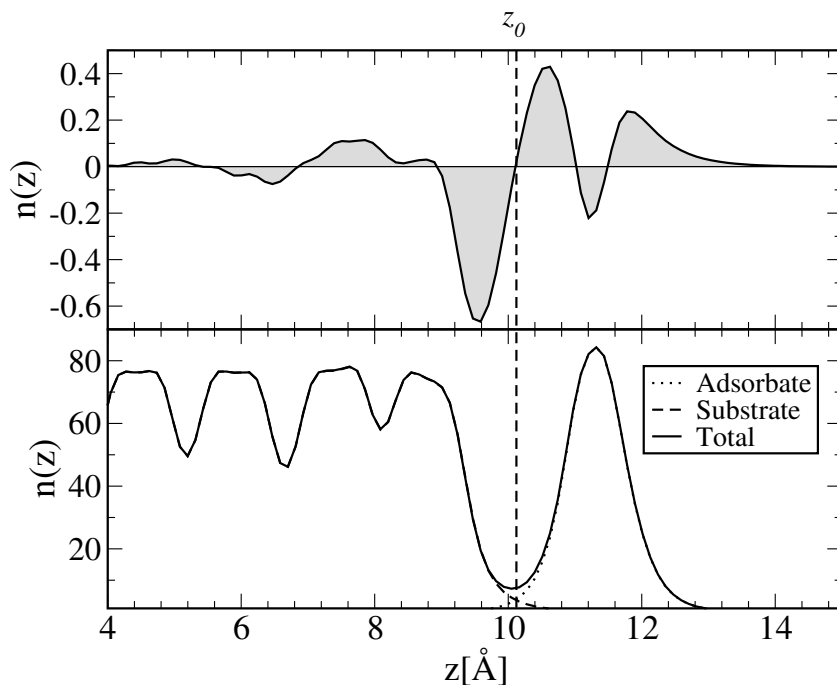
Figure 4.17: Density difference $\Delta n\,(z)$ (top panel) and the total densities of the total system, bare substrate, and the adsorbate (bottom panel) for the NCTDA adsorbed in the T site.
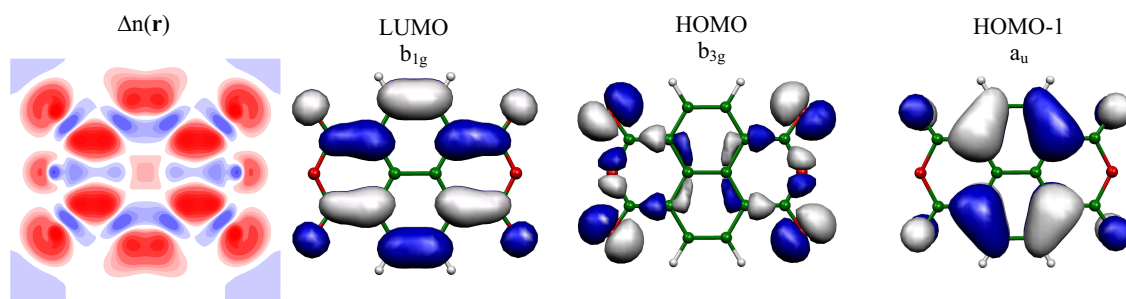
Figure 4.18: Contours of the electron density difference in a plane 0.5Å below the NTCDA molecule at the top site (left, red color - electron charge accumulation, blue - depletion), and 3D views of the LUMO (b_{1g} symmetry), HOMO (b_{3g}) and HOMO-1 (a_u) orbitals of free NTCDA.

4.5   Adsorption mechanism

The analysis in the previous section lets us propose the mechanism for the adsorption of NTCDA on the Ag(110) surface. It accounts for all the facts that have been found in the DFT calculations: the preference of T and SB sites over the LB and H sites, charge transfer from the substrate to the molecule, and bending of the molecule in the favourable sites.

1. NTCDA, being an electron acceptor (see Fig. 4.8), takes ~ 0.4 electrons from the silver substrate upon adsorption. The LUMO of the molecule is partially filled.

2. Charge transfer from the metal to the molecule leads to a slight positive charging of the silver atoms in the topmost layer (Fig. 4.16). The carboxyl oxygens, being already negative in the isolated molecule, are therefore attracted to the positively charged silver atoms atoms in the $[1\bar{1}0]$ atomic rows. This is the main difference between favourable and unfavourable sites: the Ag-O distances are significantly shorter in the case of the T and SB sites than in the case of the LB and H sites.

3. The local electrostatic Ag-O attraction distorts the molecule from the planar configuration.

   The mechanism is schematically illustrated in Fig. 4.19.

4.6   Conclusions

In this chapter we presented thorough DFT studies of NTCDA adsorbed on the Ag(110) surface. The calculated results agree with the relevant experimental data and allowed us to propose a model of the interaction of NTCDA with the Ag(110) surface. We believe that the proposed scenario, which is quite similar to the mechanism recently established for PTCDA on Ag(111) [20], is also applicable to the adsorption of PTCDA on the Ag(110) surface. The mechanism accounts for many of the features which accompany the adsorption of NTCDA and similar molecules, like site-selective adsorption, charge rearrangement, and changes of geometry. Therefore, we believe it us a useful model to understand the physics of this surface system. Finally, let us try to give an answer to the question posed in Fig. 4.5: in which way do the anhydride side groups influence the adsorption of NTCDA on Ag(110)? Do the side groups influence the electronic structure of the molecule and thus increase the interaction of the aromatic part with the substrate? or do they interact with the substrate directly? We have shown, that site selectivity of adsorption comes from the local electrostatic interactions of positively charged silver atoms and negatively charged oxygens (Figs. 4.16 and 4.19c). Positive charging of the silver atoms in the first atomic layer happens because of the charge transfer from the substrate to NTCDA, which is an electron-acceptor molecule (Fig. 4.16). Thus, without the effect, represented in Fig. 4.5a, which in our case means charge transfer from the substrate to the molecule, there would be no effect, depicted in Fig. 4.5b, which in our case means local electrostatic attraction between the peripheral oxygen atoms and silver atoms. Therefore, both effects are equally important.
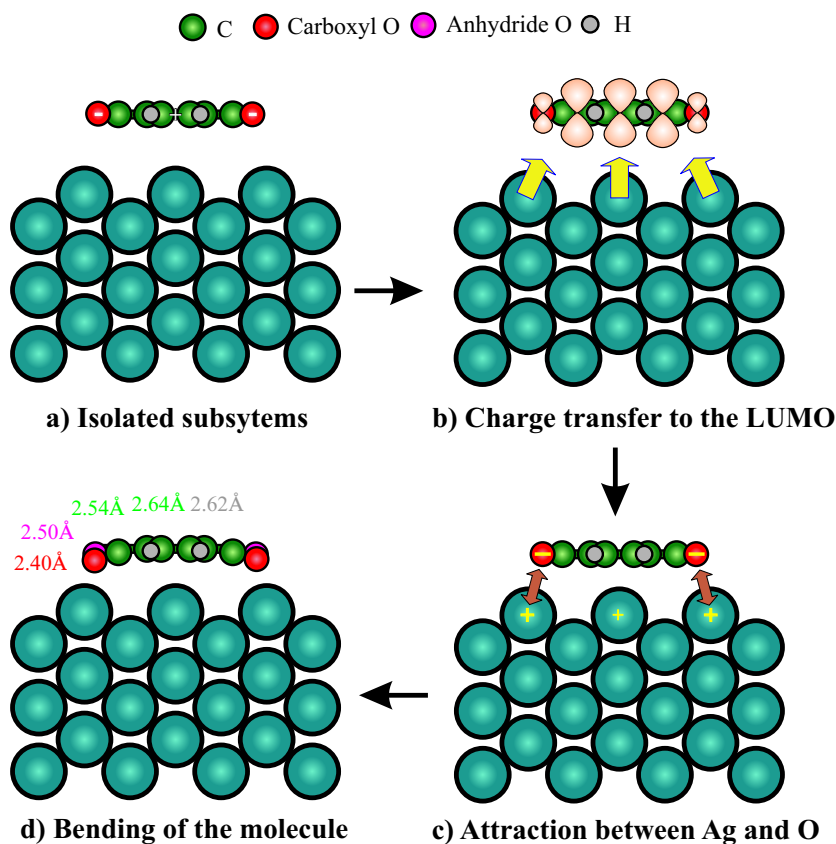
Figure 4.19: Sketch of the mechanism of adsorption of NTCDA on Ag(110), viewed along the $[1\bar{1}0]$ direction. (a) Two isolated subsystems. Note the electron excess on the peripheral oxygens and positive charge on the naphthalene core. (b) Charge transfer from the substrate to the molecule, mainly to its LUMO. (c) Charge transfer causes the positive charging of the topmost silver layer and local electrostatic attraction between positively charged silver atoms and negatively charged carboxyl oxygens. (d) The Ag-O attraction causes a distortion of NTCDA from planarity, with peripheral oxygens moving closer to the surface than the naphthalene core. Numbers indicate vertical distances of the corresponding atoms from the topmost silver plane.

Bibliography

[1] D. Gador, C. Buchberger, R. Fink, and E. Umbach, *Manipulation of molecular orientation in ultrathin organic films: NTCDA on Ag(111)*, Europhys. Lett. **41**, 231 (1998).

[2] D. Gador, C. Buchberger, R. Fink, and E. Umbach, *Characterization of high-quality NTCDA films on metal substrates*, J. Elec. Spectros. Rel. Phen. **96**, 11 (1998).

[3] D. Gador, Y. Zou, C. Buchberger, M. Bertram, R. Fink, and E. Umbach, *NEXAFS investigations of NTCDA monolayers on different metal substrates*, J. Elec. Spectros. Rel. Phen. **101-103**, 523 (1999).

[4] J. Taborski, P. Vaterlein, H. Dietz, U. Zimmermann, and E. Umbach, *NEXAFS investigations on ordered adsorbate layers of large aromatic molecules*, J. Elec. Spectros. Rel. Phen. **75**, 129 (1995).

[5] M. Böhringer, W.-D. Schneider, K. Glöckler, E. Umbach, and R. Berndt, *Adsorption site determination of PTCDA on Ag(110) by manipulation of adatoms*, Surf. Sci. **419**, L95 (1998).

[6] E. Umbach, M. Sokolowski, and R. Fink, *Substrate-interaction, long-range order, and epitaxy of large organic adsorbates*, Appl. Phys. A **63**, 565 (1996).

[7] E. Umbach, K. Glöcker, and M. Sokolowski, *Surface "architecture" with large organic molecules: interface order and epitaxy*, Surf. Sci. **402-404**, 20 (1998).

[8] M. Eremtchenko, J.A. Schaefer, and F.S. Tautz, *Understanding and tuning epitaxy of large aropmatic molecules by molecular design*, Nature **425**, 602 (2003).

[9] U. Stahl, D. Gador, A. Soukopp, R. Fink, and E. Umbach, *Coverage-dependent superstuctures in chemisorbed NTCDA monolayers: a combined LEED and STM study*, Surf. Sci. **414**, 423 (1998).

[10] R. Fink, D. Gador, U. Stahl, Y. Zou, and E. Umbach, *Substrate-dependent lateral order in naphthalene-tetracarboxylic-dianhydride monolayers*, Phys. Rev. B **60**, 2818 (1999).

[11] M. Jung, U. Baston, G. Schnitzler, M. Kaiser, J. Papst, T. Porwol, H.J. Freund, and E. Umbach, *The electronic structure of adsorbed aromatic molecules: perylene and PTCDA on Si(111) and Ag(111)*, J. Mol. Struct. **293**, 239 (1993).

[12] A. Schöll, Y. Zou, T. Schmidt, R. Fink, and E. Umbach, *High-resolution photoe-mission study of different NTCDA monolayers on Ag(111): bonding and screening influences on the line shapes*, J. Phys. Chem. B **108**, 14741 (2004).

[13] M. Eremtchenko, D. Bauer, J.A. Schaefer, and F.S. Tautz, Polycyclic aromates on close-packed surfaces: functionalization, molecular chemisorption and organic epitaxy, New J. Phys. **6**, 4 (2004).

[14] F.S. Tautz, M. Eremtchenko, J.A. Schaefer, M. Sokolowski, V. Shklover, and E. Umbach, *Strong electron-phonon coupling at metal/organic interface: PTCDA/Ag(111)*, Phys. Rev. B **65**, 125405 (2002).

[15] F.S. Tautz, S. Sloboshanin, J.A. Schaefer, R. Scholz, V. Shklover, M. Sokolowski, and E. Umbach, *Vibrational properties of ultrathin PTCDA films on Ag(110)*, Phys. Rev. B **61**, 16933 (2000).

[16] F.S. Tautz, M. Eremtchenko, J.A. Schaefer, M. Sokolowski, V. Shklover, K. Glöckler, and E. Umbach, *A comparison of the chemisorption behaviour of PTCDA on different Ag surfaces*, Surf. Sci. **502-503**, 176 (2002).

[17] R.S. Mulliken, *A new electroaffinity scale; together with data on valence states and on valence ionization potentials and electron affinities*, J. Chem. Phys. **2**, 782 (1935).

[18] R. Foster, *Organic Charge-Tranfer Complexes*, (Academic Press, New York, 1969).

[19] X. Gonze *et al.*, *First principles computation of material properties: the ABINIT software project*, Comp. Mat. Sci. **25**, 478 (2002); *http://www.abinit.org*.

[20] A. Hauschild, K. Karki, B.C.C. Cowie, M. Rohlfing, F.S. Tautz, and M. Sokolowski, *Molecular distortions and chemical bonding of a large π-conjugated molecule on a metal surface*, Phys. Rev. Lett. **94**, 036106 (2005).

Chapter 5

Energy-level alignment at metal/CuOEP interfaces

This chapter deals with the energy level alignment of copper octaethylporphyrin (CuOEP for short) on three noble metal surfaces: Ag(001), Ag(111) and Cu(111). We first critically review different mechanisms that lead to a formation of the electrostatic dipole at metal-organic semiconductor interfaces and present density functional calculations of an isolated CuOEP. Then, we discuss the principles of ultraviolet photo-emission spectroscopy. Afterwards, the experimental data of CuOEP/noble metal interfaces is presented and the data is then thoroughly analyzed.

5.1 Work function changes

It was mentioned in the introductory chapter that when organic semiconductor and metal are in contact with each other an electrostatic dipole forms at the interface [1, 2, 3, 4, 5, 6, 7, 8, 9, 10]. The vacuum level alignment rule no longer holds in this case (compare Fig. 1.5a and Fig. 1.5b in Chapter 1). Two very important parameters characterize the metal-organic interface. One of them describes the change of the interface dipole as a function of the metal work function:

$$S_D = \frac{d\Delta}{d\Phi_m}.$$ (5.1)

One would expect $\Delta = 0$ (and thus $S_D = 0$) for weakly interacting interfaces. This case is the so-called Schottky-Mott limit corresponding to the vacuum level alignment rule. The other limit is the metallic contact for which the interface dipole follows the work function of the metal, i.e. $S_D = -1$. Another useful parameter, which can be measured independently in the experiment, is S_B, and it characterizes the change in the position of the molecular HOMO level with respect to the Fermi energy of the metal:

$$S_B = \frac{d\epsilon_F^v}{d\Phi_m}.$$ (5.2)

By virtue of Eq. (1.4) in Chapter 1 and under the assumption that the ionization potential (IP) is independent of Φ_m, we obtain a "sum rule": $S_B - S_D = 1$. The Schottky-Mott

limit corresponds to $S_B = 1$, while the metallic limit corresponds to $S_B = 0$, when the HOMO of the organic is "pinned" to the Fermi level in the metal.

Numerous measurements of these parameters for different systems have been reported. Usually, the values of S_B S_D are between the two extremes mentioned above. Hill *et al.* [4], for example, reported values of S_D -1.0 for PTCDA, -0.22 for Alq$_3$, -0.53 for NPD and 0 for CBP.

Here we give a short overview of the main reasons which lead to charge rearrangement at the interface. It is this charge rearrangement which leads to a electrostatic potential difference Δ across the interface. In the literature, Δ is also called the interface dipole, the change of the work function of the substrate or the shift of the vacuum level. All these definitions are correct and we use them alternatively. No unique picture however exists about different factors which determine this interface dipole, and thus energy level alignment. Different authors emphasize different mechanisms and the full complexity of the phenomena just starts to be addressed. Therefore some of the mechanisms which will be described here are not independent of each other but represent a different intuitive picture of the *physics* of the charge rearrangement at the interface and the resulting modification of the energy level alignment.

Induced density of interface states (IDIS) model and charge transfer [11, 12]. This mechanism is quite transparent and its name originates from a similar mechanism which governs the energy level alignment at the metal-inorganic semiconductor interfaces. It applies to systems for which, on one hand, the coupling between molecular orbitals and metallic states is present, but, on the other hand, it is weak enough so that perturbative treatment is valid. The way of thought is as follows. Let the molecular levels described by an index i couple weakly to the metallic states ν, and let $T_{i\nu}$ be the coupling terms in the Hamiltonian (also called the hopping terms). The metallic states will broaden the molecular levels (Fig. 5.1a). This can be described quantitatively as the self-energy of the molecular levels due to coupling to the continuum of states in the metal:

$$\Sigma_i(E) = \sum_\nu |T_{i\nu}|^2 \, G_\nu(E), \tag{5.3}$$

$G_\nu(E)$ being the Green's function of the metal states. Local density of states $\mathcal{D}(E)$ projected on molecular levels can then be expressed as the sum over partial local densities of states:

$$\mathcal{D}(E) = -\frac{1}{\pi} \sum_i \Im \frac{1}{(E - E_i) - \Sigma_i(E)}, \tag{5.4}$$

E_i being the energy eigenvalue of the isolated molecule. All terms in Eq. (5.3) and thus also Eq. (5.4) can be evaluated within the Kohn-Sham scheme. Charge neutrality level (CNL) is defined as the energy level E_{CNL} for which the integrated number of electrons of the molecule coupled to the metal is the same as that in the isolated molecule:

$$\int_{-\infty}^{E_{CNL}} \mathcal{D}(E) \, dE = N. \tag{5.5}$$

Let $\mathcal{D}_{CNL}$ be the local density of states at the charge neutrality level $\mathcal{D}_{CNL} = \mathcal{D}(E_{CNL})$ and let us assume for further discussion that the density of states is constant in some

(a)   (b)   (c)

Metal   Molecule   Metal   Molecule   Metal   Molecule
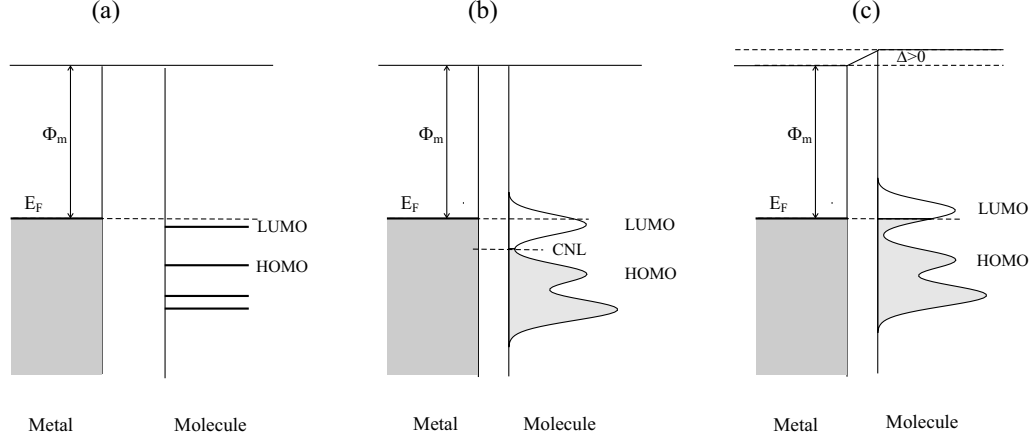
Figure 5.1: Induced density of interface states (IDIS) model. (a) A metal with a work function Φ_m and a molecule with discrete energy levels far apart; (b) Coupling of the molecular levels to the metal states leads to the broadening of the former; charge neutrality level CNL is defined via Eq. (5.5); (c) equilibration of chemical potential leads to a charge transfer and the formation of the interface dipole Δ. In this specific case $\Delta > 0$.

energy range of interest (Fig. 5.1b). Furthermore, let δ be the distance of the molecule to its image in the metal, and A_{xy} the area per molecule in the monolayer. Charge transfer ΔN to the molecule leads to the difference in the electrostatic potentials across the interface, which together with the condition that the chemical potential is the same in the molecule and in the metal allows one to calculate the derivative of the interface dipole as a function of the metal work function:

$$S_D = \frac{d\Delta}{d\Phi_m} = -\frac{e^2 \delta \mathcal{D}_{CNL}}{e^2 \delta \mathcal{D}_{CNL} + \varepsilon_0 A_{xy}}. \tag{5.6}$$

The derivative of the ϵ_v^F as a function of the metal work function, i.e. S_B, can be obtain from the "sum rule":

$$S_B = \frac{d\epsilon_F^v}{d\Phi_m} = 1 + S_D = \frac{\varepsilon_0 A_{xy}}{e^2 \delta \mathcal{D}_{CNL} + \varepsilon_0 A_{xy}}. \tag{5.7}$$

The derivation of these formulas is given at the end of the present chapter. Formulas (5.7) and (5.6) are very useful since they connect two important parameters of the metal-molecule interface: density of states at the charge neutrality level and changes of interface dipoles (and positions of molecular levels with respect to the Fermi level) as a function of the metal work function. Parameters S_B and S_D can be measured experimentally, and therefore $\mathcal{D}_{CNL}$ can be evaluated from experimental data. Even though the formulas are approximate and phenomenological (they involve, for instance, an often unknown parameter δ), they provide useful insight when the discussed mechanism of energy level alignment is the dominant one.

   Reduced metal work function ("push-back" or "pillow effect") [13, 6]. At the metal surface electrons spill out into the vacuum giving rise to an intrinsic electrostatic surface
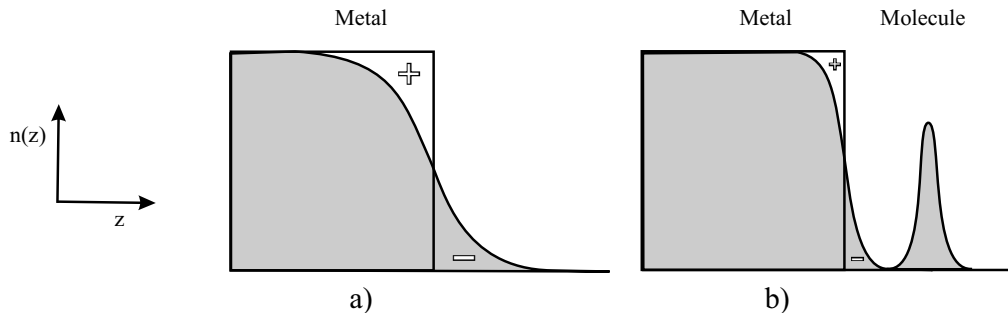
Figure 5.2: "Push-back" effect. (a) Electrons spill out into the vacuum at the surface of the metal. The created electrostatic dipole contributes to the work function of the bare substrate [13]. (b) Closed-shell adsorbates push the metal electrons back into the bulk because of the Pauli repulsion, thus reducing the work function of the substrate [6]. Horizontal axis is a direction perpendicular to the surface z, vertical axis is electron density $n(z)$.

dipole. For the jellium model within the LDA approximation this was demonstrated in the seminal paper of Lang and Kohn in the 70s [13] (Fig. 5.2a). This dipole is substrate-dependent and contributes to the total work function of the metal surface. When the closed-shell molecule adsorbs on the metal, it pushes the metal electrons back into the bulk reducing the spill-out and also reducing the work function of the combined system (Fig. 5.2b). The physical reason behind such a behaviour is Pauli repulsion between electrons in the closed-shell molecule and electrons at the metal surface, arising because of the orthogonality constraints [14] (similar the the He$_2$ case, see Chapter 2). Even though it is impossible to tell which electrons belong to the metal and which to the molecule, such an intuitive picture was proposed by Crispin *et al.* [6] from the detailed investigation of the experimental data. Analysis of closed-shell adsorbates, like Xe, on metal surfaces has shown that the contribution of the push-back effect to Δ is always negative and varies in the range $-0.4 \div -0.6$eV for different noble metal surfaces.

Polarization of the adsorbate [15]. This effect is closely related to the push-back effect. In practice they are indistinguishable. Push-back effect reveals the influence of the closed-shell molecule on the electronic structure of the metal. Let us now consider the opposite, i.e. the effect of the surface potential on the electronic structure of molecule (we assume weak interaction). Figure 5.3 shows the electrostatic surface potential perpendicular to the surface. This potential oscillates in the bulk and then rises to a constant value, called the vacuum level. The position of the adsorbate plane is z_{ad}. The electric field $\mathcal{E}$ at the position of the adsorbate z_{ad} is

$$\mathcal{E} = -\left(\frac{dV}{dz}\right)_{z_{ad}}. \tag{5.8}$$

Let α be the polarizability of the adsorbate. Finite electric field leads to a polarization of the molecule, and the induced electric dipole can be written as

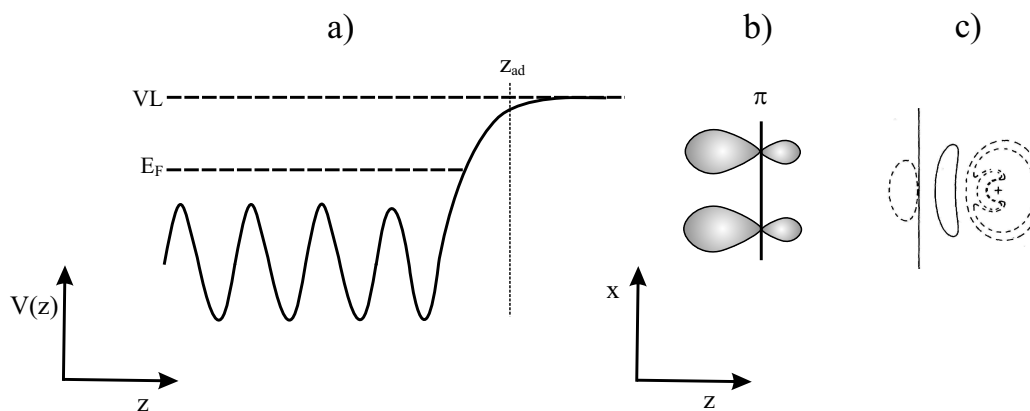$$\Delta\mu = \alpha\mathcal{E}, \tag{5.9}$$

Figure 5.3: Polarization of an adsorbate by an attractive surface potential. (a) Electrostatic potential of the metal surface $V(z)$ as a function of the vertical coordinate z. The potential oscillates in the bulk, and then increases to the vacuum level VL. E_F is the Fermi energy of the metal, z_{ad} is the plane of the adsorbate. There is a finite electric field $\mathcal{E}$ at $z = z_{ad}$. (b) Electric field $\mathcal{E}$ polarizes the adsorbate and leads to the accumulation of electron charge on the metal side and depletion of electron charge on the vacuum side. This contributes to a decrease of the work function Φ_m of the substrate, i.e. $\Delta < 0$. The example shows a polarization of the π-type state of some aromatic molecule. (c) An example of the actual calculation, illustrating the polarization effect: Xe adsorbed on the jellium surface (taken from Ref. [15]).

This induced electric dipole leads to a change of the work function of the substrate. It is easy to realize that polarization of the adsorbate contributes to the work function *decrease*, because the polarizing electric field leads to the accumulation of electron charge on the metal side and depletion of electron charge on the vacuum side (Fig. 5.3). According to the theorists' joke, "metal is always more electronegative than vacuum".

Molecules with permanent dipole moments [16]. When molecules which have an intrinsic electric dipole moment are adsorbed on the surface, it also leads to an electrostatic potential difference across the interface. This happens, for example, in the case of self-assembled alkane-thiol monolayers. De Renzi *et al.* [16] have shown that the interface dipole in these system arises mainly from the intrinsic dipole moments of methyl-thiol (MT) molecules.

Chemical interactions [17]. So far, the interaction of the molecule with the surface was considered to be weak. In this case the interaction between the subsystems is only a perturbation to their electronic structure and one can still think in terms of subsystems, for instance consider the influence of the substrate potential on the molecule, speak about charge transfer from the metal to the molecule, etc. In most systems interactions are indeed not very strong. However, for strongly interacting system such a subdivision is no longer meaningful. In this case new electronic states can be formed, which can sometimes lie in the gap of molecular states. This usually occurs for contacts of molecules with reactive metals, such as Ti or Pb [17] (Fig. 5.4). No general conclusions can be drawn about the influence of such interactions on the electrostatic dipole at the interface. The
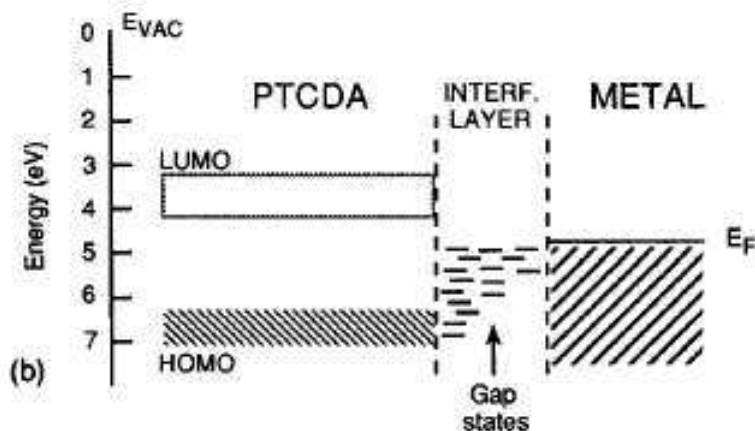
Figure 5.4: Formation of hybrid interface electronic states at reactive metal - PTCDA contact, revealed by UPS measurements (from Ref. [17]). In the case of strong interactions, hybrid states can be formed in the energy gap of the organic material.

electrostatic dipole varies greatly from system to system.

Band bending. The previous contributions to the interface dipole arise at the direct contact between the metal and the organic material. All these contributions originate from a change in the ground state electronic structure. In principle, all the previous terms can be treated together by electronic structure methods. There is however one more contribution which arises for higher temperatures and can play an important role for thick films. Due to disorder and interactions between the molecules, LUMO and HOMO states of molecules are broadened in the bulk crystal (Fig. 5.5a). At finite temperatures, the LUMO is populated by electrons and the HOMO is populated by holes. Screening due to these mobile carriers in the organic semiconductor leads to a band bending at the interface, which naturally affects the energy level alignment [7].

5.2   DFT Calculations

In this section, DFT calculation of the isolated copper octaethylporphyrin will be presented.

The structural formula of CuOEP is shown in Fig. 5.6. This molecule is composed of a copper porphine central part and eight alkyl side groups ("legs") attached to the β positions of the porphine ring. Due to the rotations of these groups around the single C-C bonds, many conformations of this molecule exist. Fig. 5.7 shows five symmetric conformers. The symmetry group, the side view, the top view, as well as the schematic representation is shown. Open square corresponds to the porphine central ring, open circles correspond to the alkyl "legs" pointing upwards, filled circles correspond to the alkyl "legs" pointing downwards. For the sake of convenience, we label the conformers P1, P2, etc.

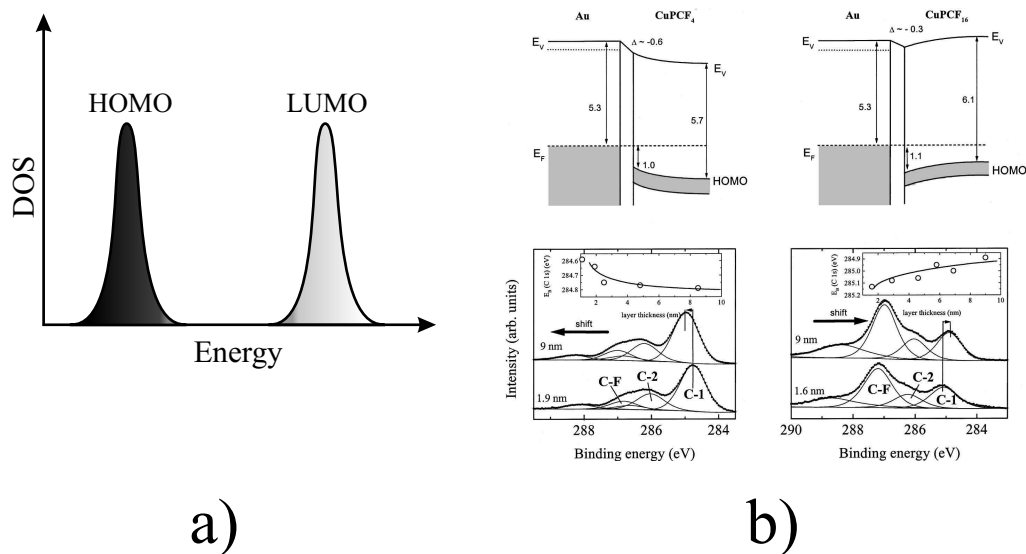a)   b)

Figure 5.5: Band bending in an organic semiconductor. (a) Density of states in the molecular solid. Due to interactions between molecules and/or disorder, the HOMO and the LUMO states are broadened. At room temperature, there is a finite density of mobile charge carriers in those states. (b) Screening due to mobile carriers in the organic leads to a band bending at the interface. The example shows band bending in CuF_4Pc and $CuF_{16}Pc$ as determined from XPS measurements [7].
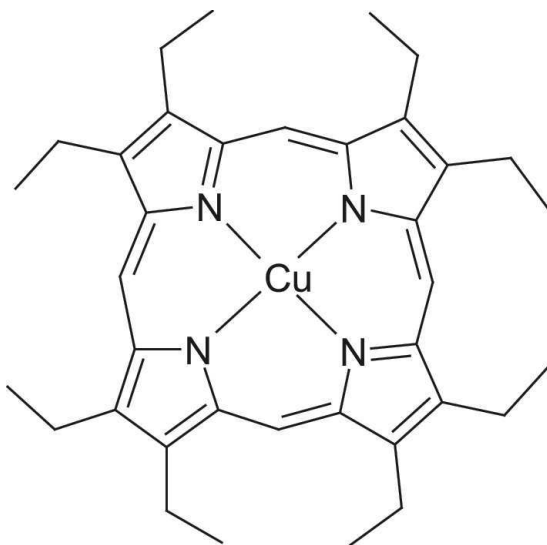

Figure 5.6: Structural formula of the copper octaethylporphyrin.

Comformer	P1	P2	P3	P4	P5
Symmetry	C_{4v}	C_S	C_{2v}	C_{2h}	D_4
E_{tot} [Ha]	-1813.36546	-1813.36556	-1813.36573	-1813.36554	-1813.36557
E_{rel} [meV]	7.2	4.5	0	5.1	4.2
p [D]	0.45	0.30	0	0	0

Table 5.1: Calculated properties of five high-symmetry conformers of CuOEP. E_{tot} is the total energy, E_{rel} is the energy relative to the most stable conformer, p is the electrical dipole moment. Conformers P3, P4 and P5 have no net dipole moment.

Density functional calculations were performed with the commercial Gaussian 03 package [18]. D95V double-zeta basis set was used for light atoms (H, N and C), while 1s states of the Cu atom were replaced by an analytic pseudopotential (sometimes called effective core potential in quantum chemistry), and the basis set of double-zeta quality was used for higher lying states. Hybrid functional B3LYP is a functional of choice for isolated molecules, and this functional together with the above mentioned basis set was used to optimize geometries of the five conformers of CuOEP shown in Fig. 5.7. The total energies, relative energies, and electric dipole moments of the five conformers are summarized in Table 5.1. The energy differences between the various conformers is of the order of meV. This is a very small difference. However, this small difference had to be expected in DFT. The differences in energies between different conformers of large organic molecules usually arise due to non-bonding van-der-Waals interactions, which are not properly grasped by DFT. We show in Fig. 5.8 the Kohn-Sham densities of states (DOS) of the five different conformations of CuOEP. As expected, the frontier orbitals are not affected by the rotations of the alkyl side groups. This is logical, since, as will be discussed below, the frontier orbitals of porphyrins are of the π type and are located on the central porphine ring with no weight on the peripheral side groups. In contrast, the orbitals which have substantial weight on the alkyl side groups, are slightly affected by the rotations of these groups, for example, orbitals which are about 5 eV below the HOMO (Fig. 5.8). The conformation that the molecule will assume in the real physical system will be determined by the interaction with the environment. This is a conclusion we make keeping in mind the smallness of differences in energies between different conformers. In fact, it is known that CuOEP assumes the P4 conformation (Fig. 5.7) in the solid phase [19]. STM measurements of Ramoino *et al.* showed that when adsorbed on the metal surface, the molecule assumes the P1 conformation [20]. All the subsequent calculations therefore were performed for this particular conformation. The top and side views of the conformer P1 are plotted in Fig. 5.9.

Let us analyze the electronic structure of CuOEP in a little bit more detail. We have plotted the energy spectrum of the CuOEP molecule in the P1 conformations together with the 3D views of the corresponding orbitals in Fig. 5.10. P1 conformer belongs to the C_{4v} symmetry group and thus all the states are labelled according to the irreducible representations of this group. The inversion symmetry of the central porphine ring is removed by the eight alkyl "legs". The HOMO of CuOEP is composed of two near-degenerate states of a_1 and a_2 symmetries, and the LUMO is made of two degenerate

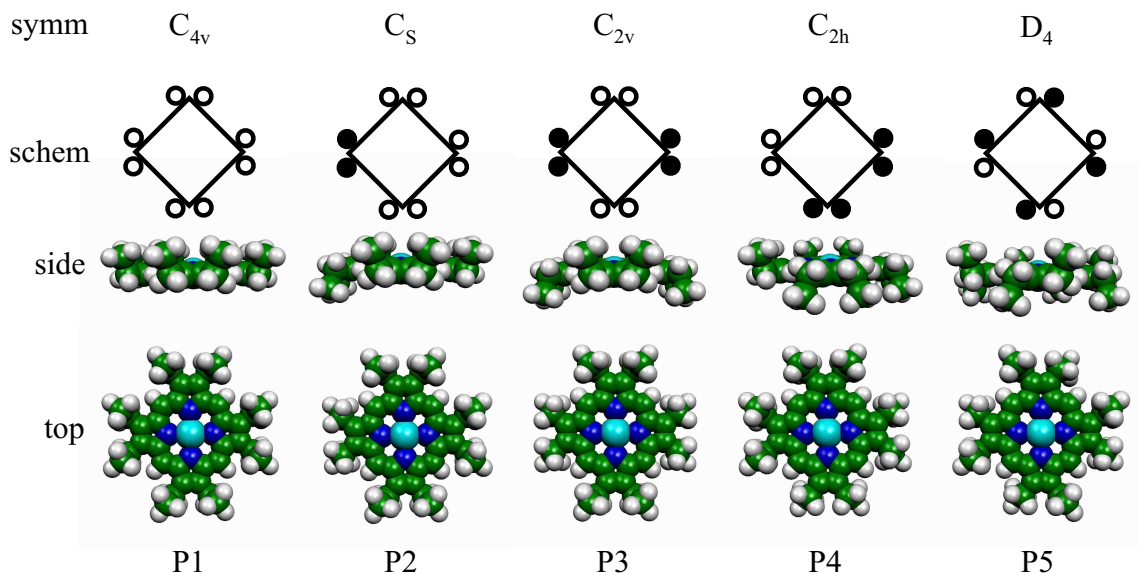| symm	C_{4v}	C_S	C_{2v}	C_{2h}	D_4
schem					
side					
top					
	P1	P2	P3	P4	P5

Figure 5.7: Five high-symmetry conformers of CuOEP. Bottom row - top view, middle row - side view, top row - schematic representation: open square corresponds to the porphine ring, open circles correspond to the alkyl "legs" pointing upwards, filled circles correspond to the alkyl "legs" pointing downwards. The symmetry group of each conformer is also indicated.

orbitals of e symmetry, in accordance with the Gouterman's picture of the frontier orbitals of porphyrins [21] and other calculations [22, 23]. For copper porphyrins, in addition, a state of a b_1 symmetry state derived from the Cu $d_{x^2-y^2}$ state belongs to the LUMO manifold. Also indicated in Fig. 5.10 is the mid-gap position of CuOEP, defined as:

$$\mu = \frac{\varepsilon_{HOMO} + \varepsilon_{LUMO}}{2} \tag{5.10}$$

We have seen in Chapter 4 that the midgap position of the molecule is a useful quantity. Mid-gap positions for NTCDA and PTCDA were found to be -5.9eV and -5.6eV, respectively, and they correlated with electron accepting properties of those molecules. The mid-gap position of CuOEP is found to be -3.9eV. We have also estimated the mid-gap position using the formula:

$$\mu' = -\frac{\text{IP} + \text{EA}}{2}, \tag{5.11}$$

where IP and EA are, as before, ionization potential and electron affinity of the molecule. The ionization potential was calculated according to equation

$$\text{IP} = E(N-1) - E(N), \tag{5.12}$$

and the electron affinity according to equation
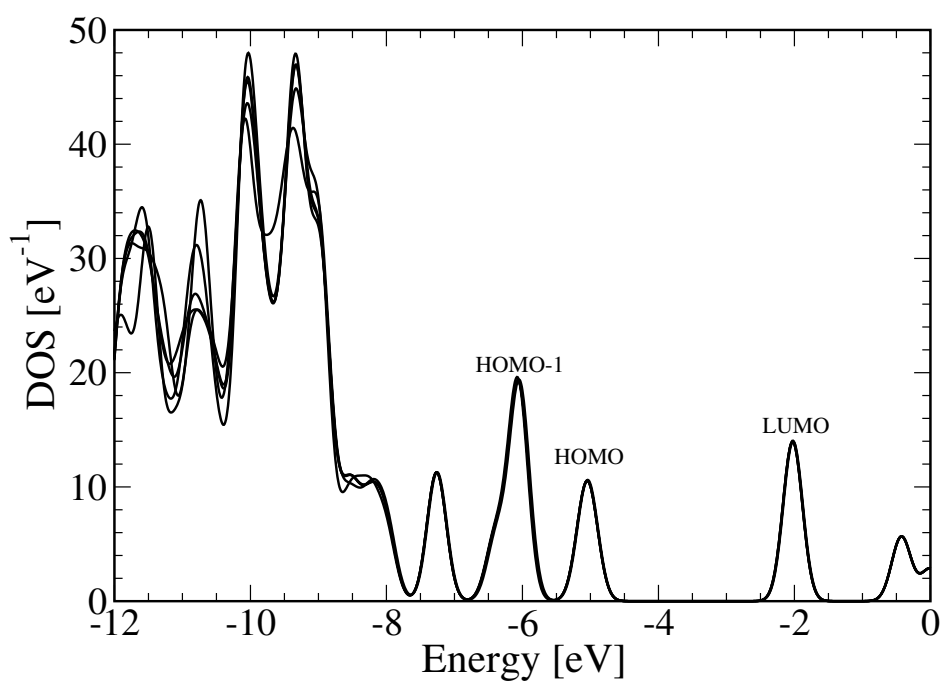
$$\text{EA} = E(N) - E(N+1). \tag{5.13}$$

Figure 5.8: Calculated B3LYP Kohn-Sham spectra of 5 different conformers of CuOEP. Rotations of the alkyl "legs" around single C-C bonds do not affect the π-type frontier orbitals of CuOEP.
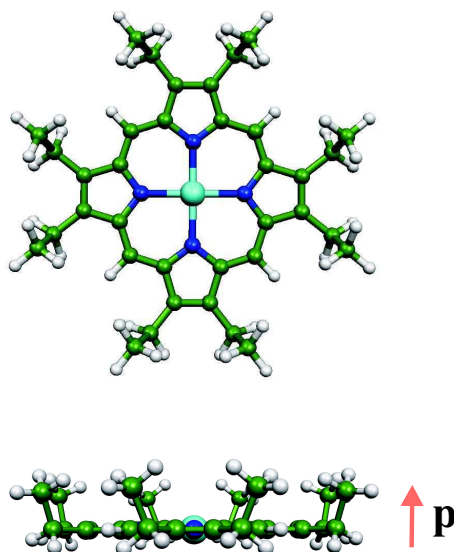
Figure 5.9: The structure of the P1 conformer of CuOEP molecule: top view (above) and side view (below). In this particular configuration with all ethyl "legs" pointing up, CuOEP possesses a small calculated electric dipole moment $p \approx 0.45$D.

p [D]	IP [eV]	ε_{HOMO} [eV]	EA [eV]	ε_{LUMO} [eV]	μ [eV]	μ' [eV]
0.45	7.22	-5.11	0.6	-2.16	-3.9	-3.6

Table 5.2: Calculated properties of the isolated CuOEP molecule in the assumed adsorbate configuration (conformer P1): p - dipole moment, ε_{HOMO} and ε_{LUMO} - Kohn-Sham eigenenergies of the frontier orbitals, IP - ionization potential, EA - electron affinity, μ and μ' - midgap positions, calculated according to Eqs. (5.10) and (5.11), respectively.

Above, $E(N-1)$, $E(N)$ and $E(N+1)$ are the total energies of the cation CuOEP^{+1}, the neutral molecule, and the anion CuOEP^{-1}, respectively. A value $\mu' = -3.6$eV was obtained. The results of the calculation for the P1 conformer are summarized in Table 5.2.

Dependence on the functional. In addition to the B3LYP functional, we have calculated the Kohn-Sham spectra of CuOEP using another hybrid functional, B3PW91, as well as pure GGA functionals BLYP and PBE. Densities of states for these four functionals are shown in Fig. 5.11. There are two major differences. First, pure GGAs predict that the unoccupied b_1 state derived from the Cu $d_{x^2-y^2}$ state is lower in energy than the π-type degenerate e states. Second, the band gap is smaller in the case of pure GGAs. We must stress again, that the Kohn-Sham spectra are not the spectra of electronic excitations. Calculations show that even though PBE and BLYP predict the b_1 state to lie below the e states in the neutral CuOEP, the order is reverse in the anion CuOEP^{-1}. This means,
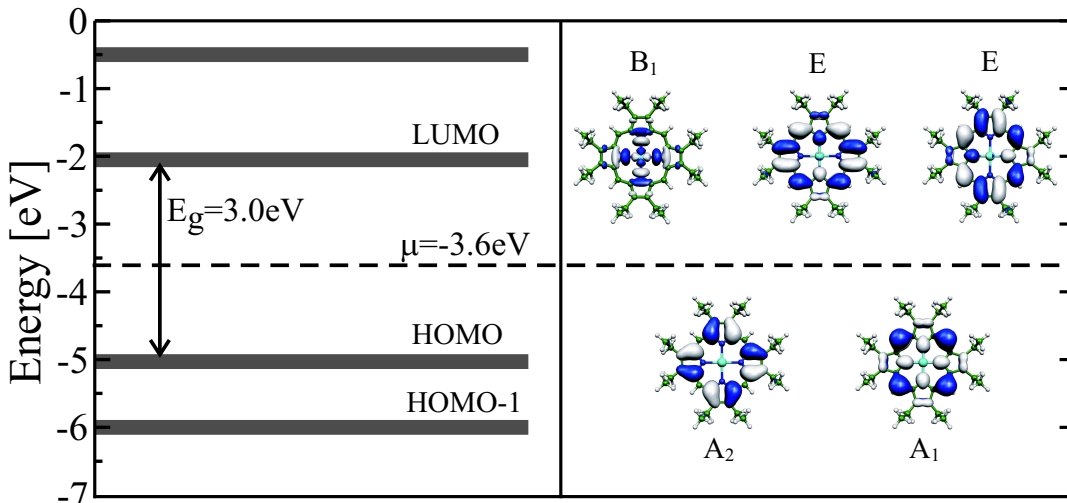
Figure 5.10: The computed DFT-B3LYP eigenvalues (left) and top views of CuOEP with superimposed frontier orbitals (right). The midgap position is indicated by a dashed horizontal line.

that an added extra electron occupies the e state rather than the b_1 state. This is also true for hybrid functionals. The discrepancy between the pure and the hybrid functionals in description of the b_1 state originates from the spurious self-interaction errors in local density approximation [24].

5.3   Ultraviolet photoemission spectroscopy

Ultraviolet photoelectron spectroscopy (UPS) is a technique which is based on the photoelectric effect. Photoelectric effect (or, photoeffect, for short), was discovered in 1887 by H. Hertz and the quantum theory of it was formulated by A. Einstein in 1905. In photoemission spectroscopy, the investigated material is irradiated with a monochromatic ultraviolet light with frequency a ω. If the work function of the sample is Φ, the ejected electrons (called photoelectrons), have a kinetic energy:

$$E_{kin} = \hbar\omega - \Phi - E_b. \tag{5.14}$$

Here E_b is the binding energy of electrons in the solid with respect to the Fermi energy (in this chapter we deal only with metallic systems). In Fig. 5.12, left, the principles of UPS are illustrated. The electronic states in the metal are distributed according to the total density of states, and all the states up to the Fermi level are occupied (the shaded region). A quantum of light with an energy $\hbar\omega$ is incident on the solid. If we neglect all the inelastic processes, the kinetic energy of the emitted electrons will be given by the Eq. (5.14). Under an assumption that the photon absorption cross section does not depend on the energy of the emitted electrons, the distribution of the kinetic energies of the emitted photoelectrons will resemble the density of states in the metal (this is not exactly true due to the so-called final state effects). Thus UP spectra provide useful information
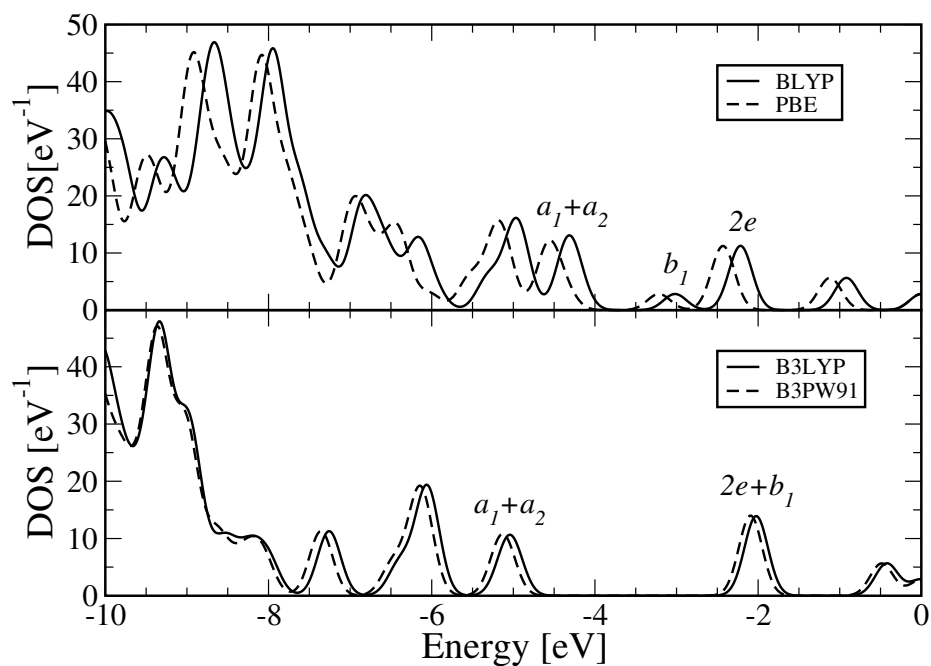
Figure 5.11: DOS of the isolated molecule calculated using pure GGA functionals BLYP and PBE (top panel) and hybrid functionals B3LYP and B3PW91 (bottom panel). The gap is smaller for pure functionals. Also the unoccupied b_1 state, derived from the Cu $d_{x^2-y^2}$ state, is lower in energy than the two e states for pure functionals.
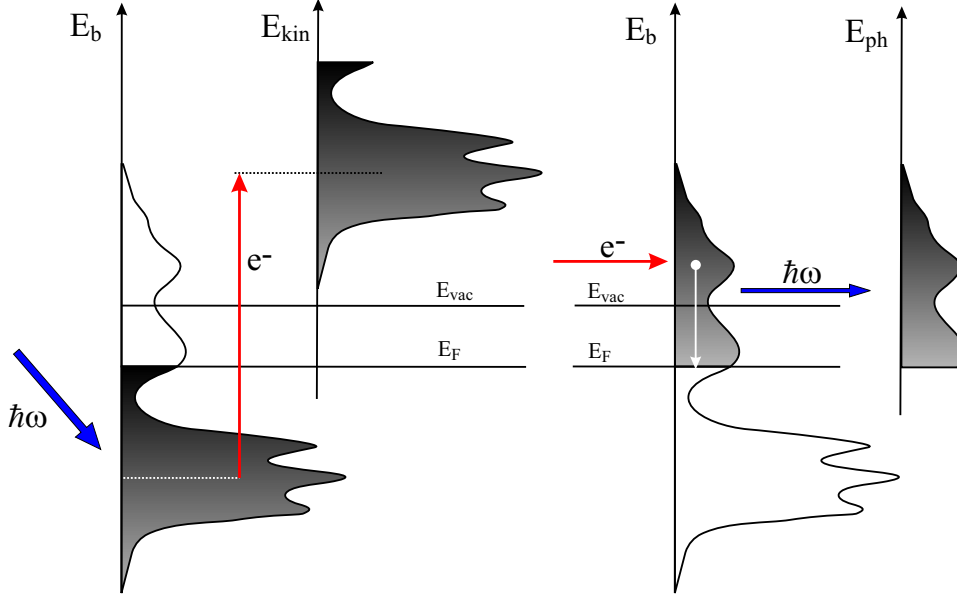
Figure 5.12: The principles of ultraviolet photoemission spectroscopy (left) and inverse photoemission spectroscopy (right).

about density of states inside the solid. Only occupied states can be monitored with UPS because of the nature of the photoemission process. The unoccupied states can be monitored using a complementary technique - inverse photoemission (Fig. 5.12, right).

The presented picture of UPS is oversimplified. In reality Eq. 5.14 is not completely correct and should be slightly modified. In fact, not only the work function of the sample, but also the work function of the detector plays a role. Thus, in principle,

$$E_{kin} = \hbar\omega - \Phi - E_b + \Delta E, \tag{5.15}$$

where ΔE is (generally) an unknown constant. Besides the elastic processes, inelastic electron-electron collisions occur in the metal. An electron, which acquires additional energy after an absorption of the photon, can loose it to other electrons through inelastic collisions and only then leave a solid. These electrons are called secondary electrons. Some electrons loose all their kinetic energy and never reach the surface. A small fraction of the secondary photoelectrons after many collisions leave the metal but have almost zero kinetic energy at the surface of the solid. To detect them, a potential V is applied between the sample and the detector. Let us look at Fig. 5.13. The largest kinetic energy electrons are those that originate from the Fermi level and do not loose any energy through inelastic collisions. In the detector, the kinetic energy of those electrons is:

$$E_{max} = \hbar\omega - \Phi + eV + \Delta E. \tag{5.16}$$

The smallest kinetic energy electrons are those that have zero kinetic energy at the surface of the sample. The kinetic energy of those electrons in the detector is:

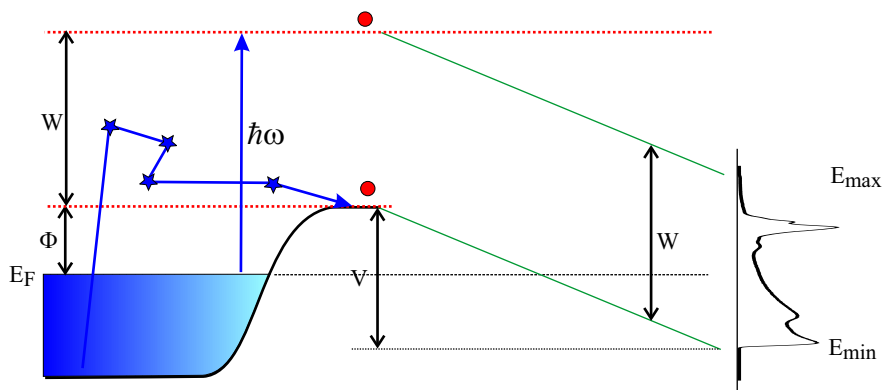$$E_{min} = eV + \Delta E. \tag{5.17}$$

Figure 5.13: The principles of work function measurements with UPS. Φ_m is the work function of the sample, V is the retarding potential, W is the spectral width, $\hbar\omega$ is the photon energy, E_{max} and E_{min} are maximal and minimal kinetic energies of electrons reaching the spectrometer.

In both Eq. (5.16) and Eq. (5.17) ΔE is the same, and V is an additional potential (sometimes called the retarding potential) to ensure that all secondary electrons reach the detector. Subtracting Eq. (5.17) from Eq. (5.16) one obtains:

$$E_{max} - E_{min} = \hbar\omega - \Phi. \tag{5.18}$$

The quantity $W = E_{max} - E_{min}$ is called the spectral width. The work function can then be determined:

$$\Phi = \hbar\omega - W. \tag{5.19}$$

This equation is used to determine the work function of the solid. An unknown quantity ΔE (which we do not even show in Fig. 5.13) now longer appears.

Formula (5.19) is also valid for surfaces covered with adsorbates. Measuring the whole width of the UP spectra for adsorbate-covered surfaces allows to determine the work function of the solid Φ', and thus the change of the work function caused by the adsorption of molecules:

$$\Delta = \Phi' - \Phi_m. \tag{5.20}$$

Here Φ_m is the work function of the clean metal surface.

5.4   UPS Results

Three metal surfaces were used in this study: Ag(001), Ag(111) and Cu(111). First, the UP spectra of bare metal surfaces were recorded. Afterwards, the UP spectra were measured as a function of CuOEP coverage. This allowed to monitor the change of the work function under deposition of the molecules. The low binding energy spectra of CuOEP at saturation coverage, together with the UP spectra of bare metal substrates, are presented in Fig. 5.14. Two sets of molecular states are clearly resolved in the spectra.
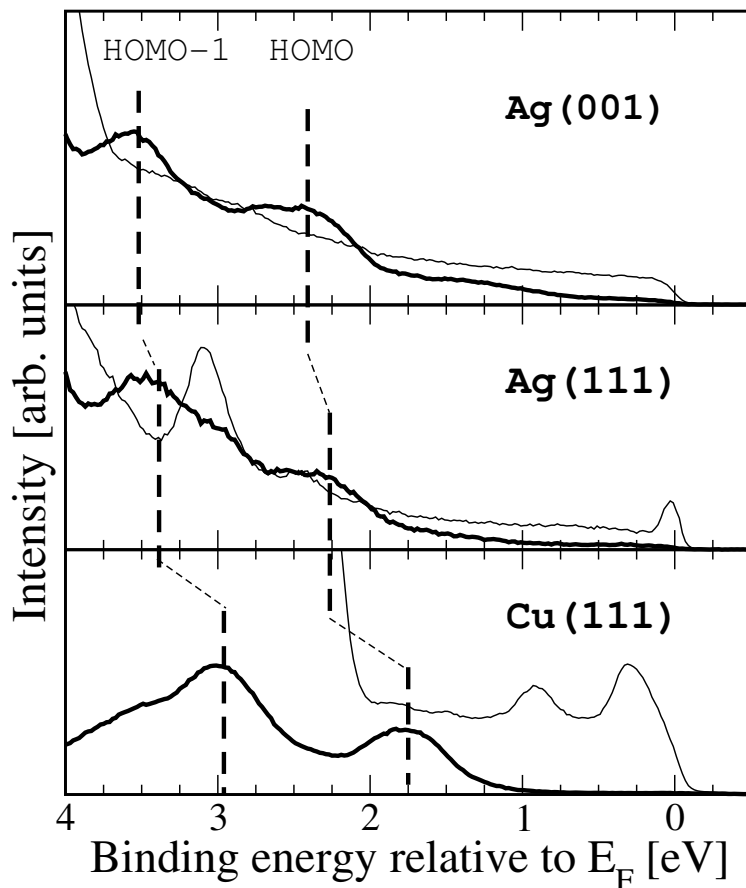
Figure 5.14: The low binding energy part of the UP spectra of CuOEP adsorbed on Ag(001), Ag(111) and Cu(111) at saturation coverage. Dashed lines - bare metal surfaces, full lines - multilayers of CuOEP at saturation coverage. The vertical dashed lines indicate the approximate positions of the HOMO and HOMO-1 states of CuOEP.

These are the HOMO and HOMO-1 states. As it was already mentioned, the HOMO, as well as the HOMO-1, consist of more than one state of similar energies. From the spectra in Fig. 5.14 the positions of the HOMO with respect to the Fermi energies, ϵ_F^v, can be deduced. For a more meaningful comparison with the published gas phase data [25], we use the positions of the maxima of the HOMO peaks as reference energies. In the organic electronics literature, the top of the HOMO band is more frequently used instead.

The evolution of the UP spectra under the deposition of CuOEP is presented in Fig. 5.15. The shift of the secondary electron low-energy peak towards smaller kinetic energies is clearly seen. The work functions of the substrates as a function of the CuOEP coverage are calculated from the spectra. The changes Δ with respect to the work function of the bare substrate are depicted in Fig. 5.16. For all the three substrates Δ's are negative, i.e. deposition of the organic reduces the work function of the metal substrate. Initially work functions decrease linearly as a function of CuOEP coverage θ, but then saturate for $\theta > 2$ (Fig. 5.16). The decrease at saturation is about 0.85eV for the Ag(001)

Surface	Φ_m	Δ	ϵ_F^v	IP1	IP2
Ag(001)	4.55	−0.85	−2.3	5.9	7.0
Ag(111)	4.62	−1.10	−2.2	5.7	6.8
Cu(111)	5.10	−1.30	−1.8	5.5	6.7
Gas phase [25]	-	-		6.5	7.6

Table 5.3: Summary of the UPS results at the saturation coverage. Φ_m is the metal work function, Δ is the work function shift at saturation, ϵ_F^v is the position of the HOMO level with respect to the Fermi energy, IP1 and IP2 are the first and the second ionization potentials of the molecular film.

substrate, 1.1eV for Ag(111), and 1.3eV for Cu(111).

The results obtained from the UP spectra are summarized in Table 5.3.

5.5 Discussion

Ionization potentials and screening. First we discuss the ionization potentials (IPs) of the molecular films. These can be deduced from the following formula:

$$\text{IP} = \hbar\omega - E_{HOMO} + E_{min}, \tag{5.21}$$

which is analogous to Eq. 5.19. Here E_{HOMO} is the kinetic energy at the center of the HOMO peak, E_{min} is, as before, the secondary-photoelectron kinetic energy cutoff, and $\hbar\omega$ is the photon energy. We find that the measured ionization potentials of the saturated organic films are slightly different on the three substrates (Table 5.3): 6.0 ± 0.2 eV for Ag(001), 5.7 ± 0.2 eV for Ag(111) and 5.6 ± 0.2 eV for Cu(111). The ionization potential of the CuOEP in vacuum was measured in 70s by Kitagawa *et al.* [25]. As was discussed previously, the HOMO of the porphyrins consist of two nearly degenerate energy levels. These can be resolved in the gas phase. Kitagawa *et al.* [25] obtained ionization energies of 6.31eV and 6.72eV for these two states. These two states appear as one broad peak in the Basel condensed-phase experiments (Fig. 5.14). For a reasonable comparison, we use an average of the two above mentioned gas-phase values, i.e. 6.5eV. The first conclusion which can be drawn is that the ionization potentials of the molecular films are smaller than the gas phase value ($5.6 - 6.0$eV vs. 6.5eV). The reasons for this are well known and are thoroughly analyzed in the literature [26, 27]. When the photohole is created on some certain molecule in the crystal, the surrounding molecules screen the created positive charge. In the end, the positively charged molecular ion is stabilized due to electrostatic interactions (electronic screening). The resulting stabilization energy is also called the polarization energy and is usually labeled P_+ (see Fig. 5.17a). The measured ionization potential in the solid state is therefore smaller than the ionization potential of the isolated molecule:

$$\text{IP}_{bulk} = \text{IP} - P_+. \tag{5.22}$$

Screening by surrounding molecules is basically a bulk phenomenon. However, the ionization potential of the molecule in the solid is not easily accessible experimentally. UPS
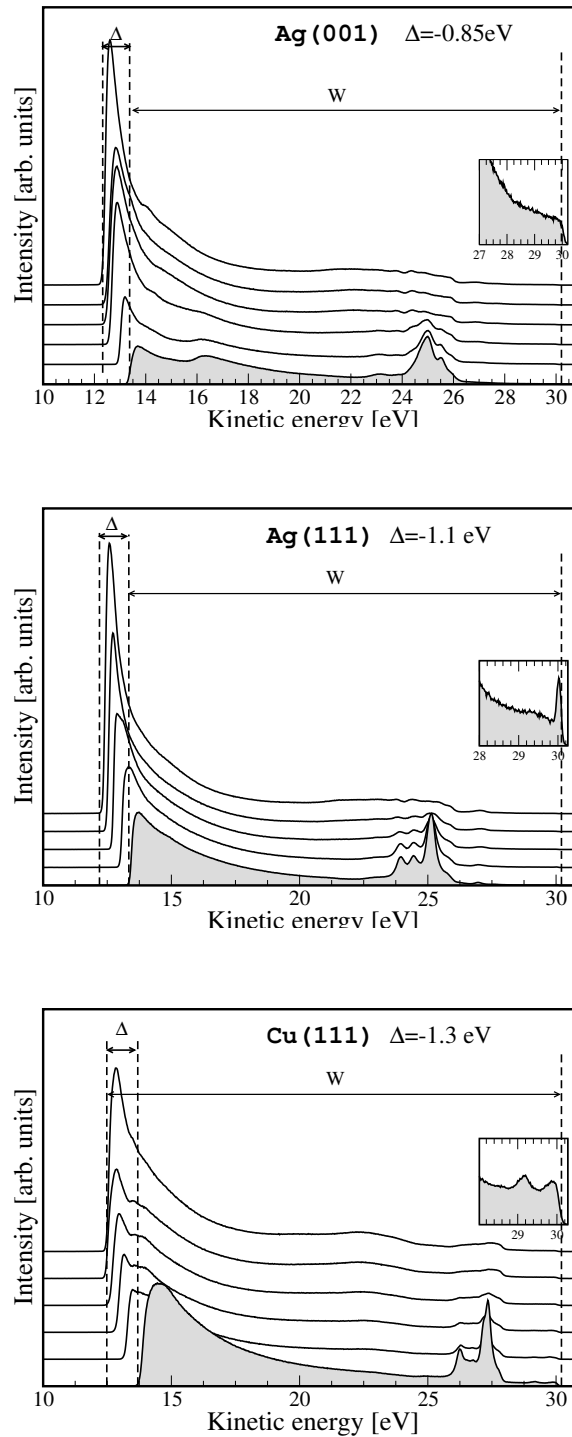
Figure 5.15: Evolution of the UPS spectra for the three different surfaces upon deposition of CuOEP. Spectral widths W and work function shifts at saturation Δ are shown. Spectra for different CuOEP coverage is shifted in vertical direction for clarity, and the UP spectrum of the bare metal surface is shaded. Insets show the spectra of the bare metal surfaces near the Fermi edge.
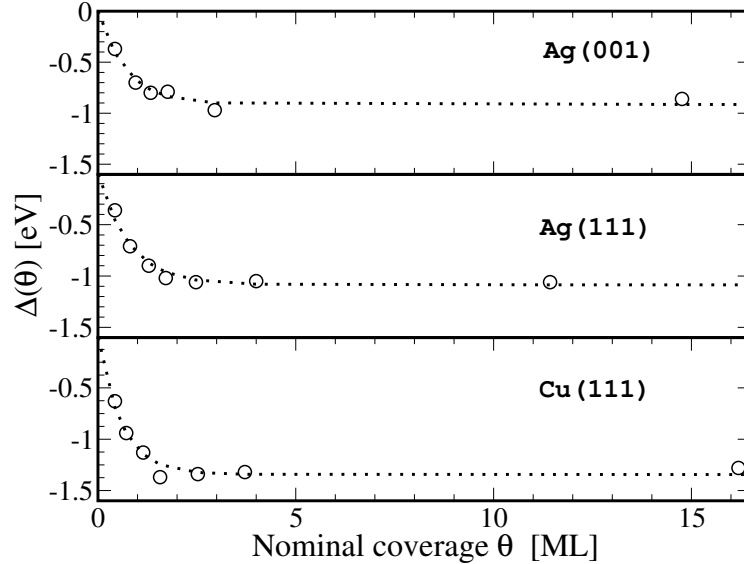
Figure 5.16: Work function shift $\Delta(\theta)$ as a function of the nominal CuOEP coverage θ for the three different substrates as determined from UPS measurements. Top panel - Ag(001), middle panel - Ag(111), bottom panel - Cu(111). Dotted lines are guides to the eye.

is a surface-sensitive technique and only molecular layers which are close to the surface are probed. This also means, that the resulting photohole is only partially screened (Fig. 5.17b). The measured ionization potential of the molecules at the surface of the molecular crystal is:

$$IP_{surf} = IP - \eta P_+. \tag{5.23}$$

The parameter η accounts for a partial screening. $\eta = 1$ corresponds to bulk screening, $\eta = 0$ corresponds to no screening. At the surface $0 < \eta < 1$. For thin molecular layers on metallic substrates, screening due to the conduction electrons in the metal underneath can also be appreciable (Fig. 5.17c). Quantitatively, this was analyzed by Gadzuk in the context of XPS [28] and by Tsiper *et al.* in the context of thin organic films [29]. The latter authors employed a microscopic model to study the screening of the photohole in the topmost molecular layer as a function of the thickness of the molecular film. The screening was found to be as large as 1.0eV for the molecules in the one-monolayer film. Polarization energy decreases to less than 0.1eV for the outer molecules in the five-monolayer film. Since saturation coverages which are used to determine the ionization potentials are at least 5ML in our case (Fig. 5.16), we can neglect the screening due to metallic electrons. Thus, the reduced ionization potential is mainly due to electronic screening of the surrounding molecules at the surface of the organic film (Fig. 5.17b). The typical values of ηP_+ in Eq. (5.23) were found to be around 0.8eV [27] for a wide range of different organic molecules. Our measurements give $\eta P_+ = 0.5 \div 0.9$eV, and these values are consistent with previous estimates.

LEED patterns [30] reveal that CuOEP films on each of the two silver surfaces have a specific lateral periodicity which is quite different from the packing in the bulk molecular
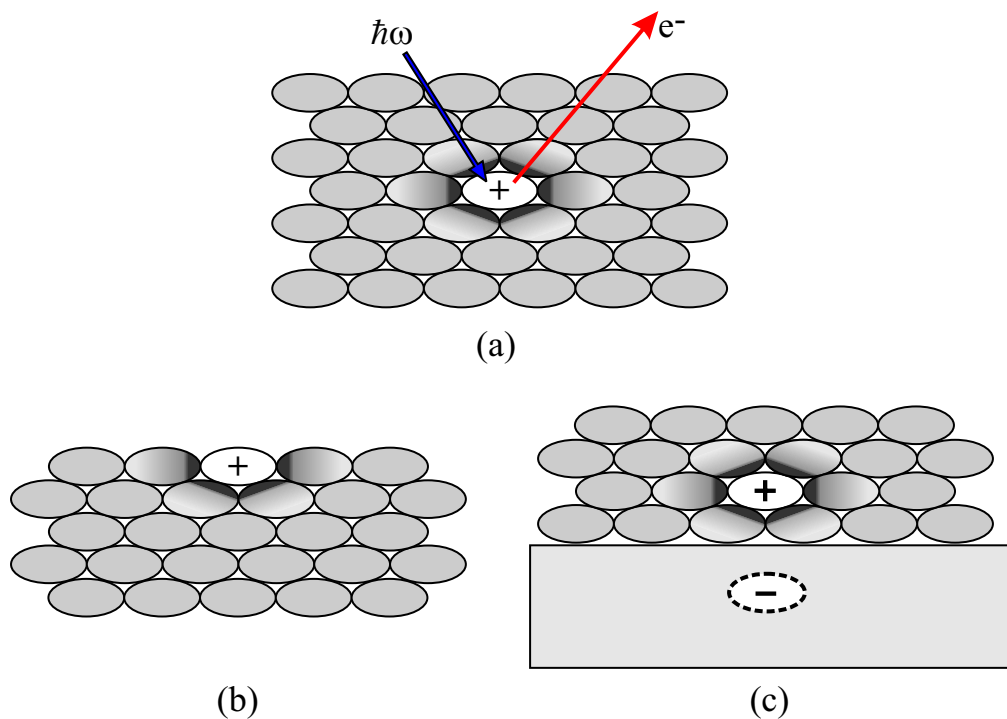
Figure 5.17: Screening of the photohole: (a) Due to electronic polarization of the surrounding molecules, ionization potential of the molecule is smaller by P_+ in the bulk than in vacuum; (b) at the surface of the organic crystal, the screening is incomplete - ionization potential is reduced by ηP_+ with $0 < \eta < 1$; (c) for molecules in thin films screening due to electrons in the metal also lead to a decrease of the measured ionization potential.
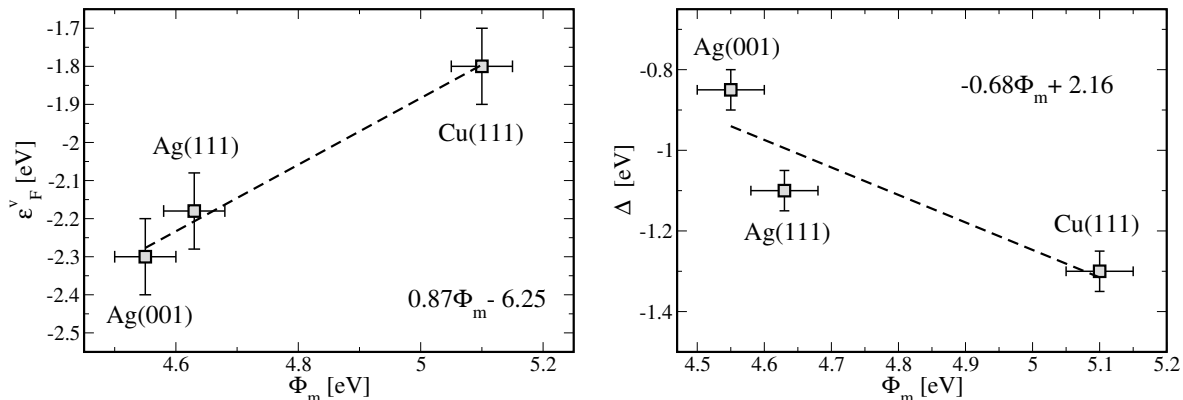
Figure 5.18: Left: position of the HOMO of the organic film with respect to the Fermi level ε_F^v as a function of the substrate work function Φ_m. Right: interfacial dipole at saturation Δ as a function of the substrate work function.

crystal [19]. On the Cu(111) surface no lateral order at saturation coverage is observed. The different experimental values of IPs might be therefore due to the differences in the local environments of the molecules. A small dependence of the ionization potential of the molecular film on thin film morphology was already observed previously for 4,4'-N,N'-dicarbazolyl-biphenyl (CBP) on Au, Ag, and Mg by Hill *et al.* [5].

Work function shifts. The measured dependencies of Δ and ϵ_F^v on the work function of the substrate, which were presented in Table 5.3, are plotted in Fig. 5.18. Least-squares linear fits were used to extract the values of the interface slope parameters, S_D (Eq. 5.1) and S_B (Eq. 5.2). We have obtained: $S_B \approx 0.87$, and $S_D \approx -0.68$. A small dependence of the ionization potential on the substrate leads to a violation of the "sum rule" $S_B - S_D = 1$. In the introductory section of this chapter we have discussed too limiting cases of metal-organic interfaces: the case $S_D = -1$ corresponds to the Fermi level "pinning" or the metallic interface, while thaw case $S_D = 0$ corresponds to the vacuum level alignment. In our case, as for the other systems, the obtained value ($S_D = -0.68$) is between these two extremes.

At the end of this Chapter, we evaluate different contributions to the interface dipole at the CuOEP-metal interfaces. Let us focus only on the first monolayer. The corresponding dipoles for the 1ML coverage are -0.6eV, -0.7eV, and -1.0eV for the Ag(001), Ag(111), and Cu(001) surfaces, respectively. As we have discussed in the first section of this Chapter, the electrostatic dipole at the interface between the metal and the organic semiconductor is composed of several contributions. As a first approximation, we can write:

$$\Delta = \Delta_{met} + \Delta_{pol} + \Delta_{dipole} + \Delta_{CT}, \tag{5.24}$$

where Δ_{met} is the contribution from the push-back effect, Δ_{pol} is the contribution from the polarization of the adsorbate, Δ_{dipole} comes from the intrinsic dipole moment of CuOEP,

and Δ_{CT} is the charge transfer part (as described by the induced density of interfaces states model). For Xe on silver and copper surfaces the first two contributions are $\Delta_{met} + \Delta_{pol} \approx -0.6.. - 0.4$eV. For more polarizable adsorbates, like CuOEP, this part can even be larger.

The contribution from the intrinsic dipole moment of the molecules can be evaluated using the Helmholtz relation:

$$\Delta_{dipole} = \frac{\Delta\mu}{\varepsilon_0 A_{xy}}.$$

The areas per molecule are known from LEED experiments [20]. CuOEP adsorbed on the metal surface assumes a configuration with all alkyl "legs" pointing up (Fig. 5.9), and the dipole moment in such a configuration is 0.45eV with alkyl "legs" being slightly positively charged, and the porphine ring carrying some effective negative charge. The corresponding contributions Δ_{dipole} are about -0.1eV for all three surfaces.

The chemical potential of the molecular solid is approximately equal to the midgap positions, i.e. $\mu_{mol} \approx -3.6$eV. The chemical potential of the metal with respect to the vacuum level close to the surface is $\mu_{met} = -\Phi_m$ (see Table 5.3). In all cases $\mu_{met} < \mu_{mol}$, and thus charge transfer from the molecule to the metal can also be expected. This would yield $\Delta_{CT} < 0$. However, for this to happen, metal-induced density of states at the midgap position should be large enough (Fig. 5.1). In other words, coupling of molecular states to the metallic states should be strong enough. This is unlikely in our case, since low-binding energy UP spectra show (Fig. 5.14) that occupied molecular states are quite far from the Fermi level and have widths smaller than 1eV. We therefore conclude that the charger-transfer contribution to the interface dipole is small.

5.6   Derivation of S_D in the IDIS model

In this section we derive the expression of the interface slope parameter in the IDIS (induced density of interface states) model, Eq. (5.6).

Let us first assume that the monolayer of molecules is interacting with a metal with a work function Φ_{m1} (Fig. 5.19, left). Let us assume also for simplicity that for this particular work function of the metal Φ_{m1} the vacuum level alignment rule holds, that is, the charge neutrality level of the molecule is aligned to the metal Fermi level (this assumption does not change the general result obtained below but simplifies the derivation). The density of states on the molecule is assumed to be constant, $\mathcal{D}$, and independent of the metal work function. The distance from the monolayer to the metal is δ, and A_{xy} is the area per molecule. Now let the molecule interact with a metal which has a different work function, Φ_{m2} (Fig. 5.19, right). Let us work out the case when the metal work function is larger, i.e. $\Phi_{m2} > \Phi_{m1}$. In equilibrium, the chemical potential in the molecule must be the same as that in the metal. To fulfill this, ΔN electrons flow from the molecule to the metal. This change of an electron charge on the molecule leads to a potential energy drop, Δ. We see from Fig. 5.19, right, that the amount of electrons transfered from the molecule to the metal can be written as:

$$\Delta N = (\Phi_{m2} - \Phi_{m1} + \Delta)\,\mathcal{D} = (\Delta\Phi_m + \Delta)\,\mathcal{D} \qquad (5.25)$$

(potentials are in energy units). Here we assume $\Delta < 0$, $\Delta\Phi_m = \Phi_{m2} - \Phi_{m1} > 0$, and $\Delta N < 0$. Condition (5.25) is the condition of equilibration of chemical potentials, which we assume. On the other hand, the drop in electrostatic potential is related to the change in electron number on the molecule via Gauss's theorem:

$$\Delta = -\frac{e^2 \Delta N \delta.}{\varepsilon_0 A_{xy}} \tag{5.26}$$

Combining Eqs. (5.25) and (5.26) gives:

$$\left(\frac{\varepsilon_0 A}{e^2 \delta \mathcal{D}} + 1\right)\Delta = -\Delta\Phi_m. \tag{5.27}$$

From here we can derive the quantity of interest:

$$S_D = \frac{d\Delta}{d\Phi_m} = -\frac{e^2 \delta \mathcal{D}}{e^2 \delta \mathcal{D} + \varepsilon_0 A_{xy}}. \tag{5.28}$$

The latter equation can be re-written as

$$S_D = -\frac{\mathcal{D}E_C}{\mathcal{D}E_C + 1}, \tag{5.29}$$

E_C being twice the energy needed to charge a capacitor with the capacitance $C = \varepsilon_0 A_{xy}/\delta$ with a elementary charge e:

$$E_C = \frac{e^2 \delta}{\varepsilon_0 A_{xy}}. \tag{5.30}$$

5.7 Conclusions

In this chapter we have studied the interfacial electronic properties of copper octaethylporphyrin adsorbed on Ag(001), Ag(111) and Cu(111) single crystal surfaces. On all of these substrates a lowering of the work function upon molecular adsorption has been found. The surface-dependent work function shifts are slightly larger than for tetraphenylporphyrins on metallic substrates [1]. Ethyl substituents allow for a direct contact of the porphine ring and the metallic surface, thus ensuring a stronger interaction. On the contrary, more bulky phenyl groups do not allow for such a contact. This is an interesting demonstration of the effect of side groups on the energy level alignment at the organic-metal interface. We have estimated different contributions to the interface dipole and concluded that it is dominated by polarization and push-back effects, while charge transfer contribution should be smaller. The discussion of the origin of the observed work function change shows the inherent difficulties to extract the different contributions to it. Finding a practical recipe to determine the magnitude of all physically relevant terms would greatly help for the general understanding of organic-metal interfaces.
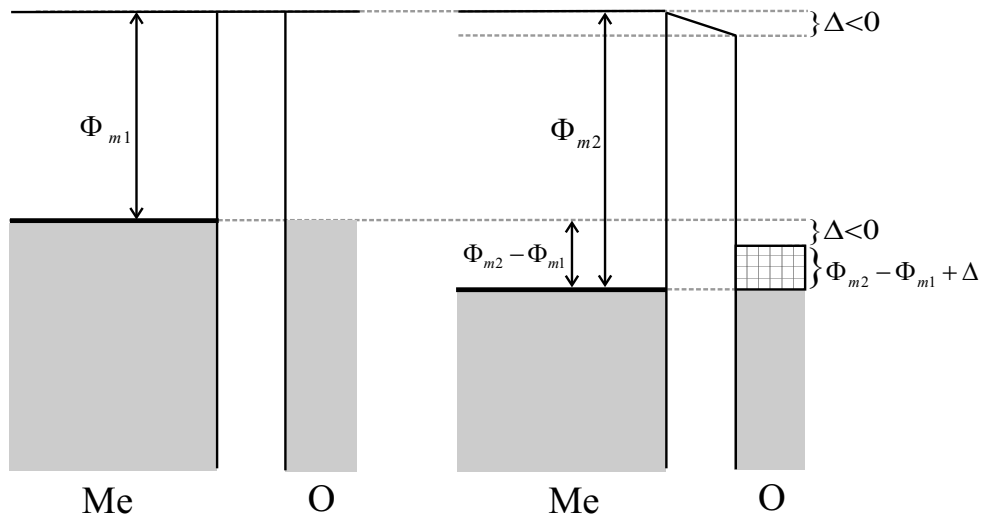
Figure 5.19: Derivation of the slope parameter in the induced density of interface states (IDIS) model. *Left*: metal with a work function Φ_{m1} (Me) interacting with a monolayer of organic molecules (O). For this specific value of Φ_{m1} the vacuum-level alignment rules holds. *Right*: metal with a work function Φ_{m2} interacting with a monolayer of organic molecules. ΔN electrons are transfered from the molecule to the metal, which leads to a formation of an interface dipole Δ.

Bibliography

[1] S. Narioka, H. Ishii, D. Yoshimura, M. Sei, Y. Ouchi, K. Seki, S. Hasegawa, T. Miyazaki, Y. Harima, and K. Yamashita, *The electronic structure and energy level alignment of porphyrin/metal interfaces studied by ultraviolet photoelectron spectroscopy*, Appl. Phys. Lett. **67**, 1899 (1995).

[2] K. Seki, E. Ito, and H. Ishii, *Energy level alignment at organic/metal interfaces studied by UV photoemission*, Synth. Met. **91**, 137 (1997).

[3] H. Ishii, K. Sugiyama, E. Ito, and K. Seki, *Energy level alignment and interfacial electronic structure at organic/metal and organic/organic interfaces*, Adv. Mat. **11**, 605 (1999).

[4] I.G. Hill, A. Rajagopal, A. Kahn, and Y. Hu, *Molecular level alignment at organic semiconductor-metal interfaces*, Appl. Phys. Lett. **73**, 662 (1998).

[5] I.G. Hill, A. Rajagopal, and A. Kahn, *Energy-level alignment at interfaces between metals and the organic semiconductor 4,4'-N,N'-dicarbazolyl-biphenyl*, J. Appl. Phys. **84**, 3236 (1998).

[6] X. Crispin, V. Geskin, A. Crispin, J. Cornil, R. Lazzaroni, W.R. Salaneck, and J.-L. Bredas, *Characterization of the interface dipole at organic/metal interfaces*, J. Am. Chem. Soc. **124**, 9161 (2002).

[7] H. Peisert, M.Knupfer, and J. Fink, *Energy level alignment at organic-metal interfaces: dipole and ionization potential*, Appl. Phys. Lett. **81**, 2400 (2002).

[8] M. Knupfer and H. Peisert, *Electronic properties of interfaces between model organic semiconductors and metals*, phys. stat. sol. (a) **201**, 1055 (2004).

[9] M. Knupfer and G. Paasch, *Origin of the interface dipole at the interfaces between undoped organic semiconductors and metals*, J. Vac. Sci. Technol. A **23**(4), 1072 (2005).

[10] D. Cahen, A. Kahn and E. Umbach, *Energetic of molecular interfaces*, Materials Today July/August, 32 (2005).

[11] H. Vazquez, R. Oszwaldowski, P. Pou, J. Ortega, R. Perez, F. Flores, and A. Kahn, *Dipole formaton at metal/PTCDA interfaces: role of charge neutrality level*, Europhys. Lett. **65**, 802 (2004).

[12] H. Vazquez, F. Flores, R. Oswaldowski, J. Ortega, R. Perez, and A. Kahn, *Barrier formation at metal-organic interfaces: dipole formation and the charge neutrality level*, Appl. Surf. Sci. **234**, 107 (2004).

[13] N.D. Lang and W. Kohn, *Theory of metal surfaces: charge density and surface energy*, Phys. Rev. B **1**, 4555 (1970).

[14] P.S. Bagus, V. Staemmler, and C. Wöll, *Exchangelike effects for closed-shell adsorbates: interface dipole and work function*, Phys. Rev. Lett. **89**, 096104 (2002).

[15] N.D. Lang, *Interaction between closed-shell systems and metal surfaces*, Phys. Rev. Lett. **46**, 842 (1981).

[16] V. De Renzi, R. Rousseau, D. Marchetto, R. Biagi, S. Scandolo, and U. Del Pennino, *Metal work-function changes induced by organic adsorbates: a combined experimental and theoretical study*, Phys. Rev. Lett. **95**, 046804 (2005).

[17] Y. Hirose, A. Kahn, V. Aristov, P. Soukiassian, V. Bulovic, and S.R. Forrest, *Chemistry and electronic properties of metal-organic semiconductor interfaces: Al, Ti, In, Sn, Ag and Au on PTCDA*, Phys. Rev. B **54**, 13748 (1996).

[18] Gaussian 03, M.J. Frisch *et al.*, Gaussian, Inc., Wallingford CT, 2004.

[19] R. Pak and W.R. Scheidt, *Structure of (2,3,7,8,12,13,17,18 Octaehylporphinato)copper(II)*, Acta Cryst. **C47**, 431 (1991).

[20] L. Ramoino, S. Schintke, M. von Arx, M. Wahl, A. Alkauskas, A.Baratoff, and T.A. Jung, *Local adsorption geometry and tunneling voltage-dependent contrast of adsorbed copper octaethylporphyrin*, in praparation (2006).

[21] M. Gouterman, in *The Porphyrins*; D. Dolphin, ed. (Academic Press, New York, 1978)

[22] D.A. Case and M. Karplus, $X\alpha$ *multiple scattering calculations on copper porphine*, J. Am. Chem. Soc. **99**, 6182 (1977).

[23] M.-S. Liao and S. Scheiner, *Comparative study of Metal-Porphyrins, Porphyrazines and Phthalocyanines*, J. Comp. Chem. **23**, 1391 (2002).

[24] J.P. Perdew and A. Zunger, *Self-interaction correction to density-functional for many electron systems*, Phys. Rev. B **23**, 5048 (1981).

[25] S. Kitagawa, I. Morishima, T. Yonezawa, and N. Sato, *Photoelectron Spectroscopic study on Metallooctaethylporphyrins*, Inorg. Chem. **18**, 1345 (1979).

[26] E.A. Silinsh and V. Čapek, *Organic molecular crystals*, AIP Press, New York, 1994.

[27] I.G. Hill, A. Kahn, Z.G. Soos, and R.A. Pascal, *Charge-separation energy in films of π-conjugated organic molecules*, Chem. Phys. Lett. **327**, 181 (2000).

[28] J.W. Gadzuk, *Screening energies of photoelectron spectroscopy of localized electron levels*, Phys. Rev. B **14**, 2267 (1976).

[29] E.V. Tsiper, Z.G. Zoos, W. Gao, and A. Kahn, *Electronic polarization at surfaces and thin films of organic molecular crustals: PTCDA*, Chem. Phys. Lett. **360**, 47 (2002).

[30] L. Ramoino, S. Shintke, M. von Arx *et al.*, unpublished data.

Chapter 6

Conclusions and outlook

In this Thesis we presented studies of two aspects of the adsorption of organic molecules on noble metal surfaces: site-selective adsorption and energy level alignment.

In Chapter 1 we have described the motivation to study the adsorption of large organic molecules on metallic substrates. Relevant aspects of density functional theory (DFT), our main theoretical tool, are reviewed in Chapter 2. Technical details of the plane-wave implementation of DFT were presented. Test calculations show that DFT performs well for bulk silver and copper, as well as silver and copper surfaces.

In Chapter 3 the adsorption of chlorine on the Ag(111) surface was studied as a further test system. Our calculations are consistent with previous theoretical studies and with available experimental results. The local adsorption site of chlorine on Ag(111) is the fcc hollow site for all the coverages studied, but the hcp hollow site is only slightly higher in energy. In general, the Cl/Ag(111) bond was found to be very strong, in accord with experimental findings. Nevertheless, the adsorption energy depends very weakly on coverage. Adsorption of Cl is accompanied by charge transfer from the metal to the adsorbate. Chlorine acquires about 0.2 additional electrons upon adsorption on the surface, and this charge transfer leads to a work function increase. The dependence of the work function on coverage is consistent with the experimental trend. The calculated adsorption-induced dipole moments helped us rationalize the small dependence of adsorption energies on coverage.

The site-selective adsorption of NTCDA on the Ag(110) surface is the topic of Chapter 4. Studies of NTCDA and the related molecule PTCDA on metal surfaces are interesting because they are prototype molecules which exhibit site-selective adsorption. Furthermore, a lot of well-established experimental data is available. Our attention was focused on lateral variation of the adsorption energy. DFT calculations of isolated NTCDA enabled us to understand the influence of the carboxylic anhydride side groups on the electronic structure of the molecule. Attaching such side groups to the naphthalene core lowers the HOMO and the LUMO energies of the molecule by about 2 eV, making it an electron acceptor. Electron accepting properties play an important role in site-selective adsorption. Large-scale DFT calculations showed that charge transfer from the metal to the molecule happens upon adsorption. The resulting electron density redistribution is responsible for the preference of specific local adsorption configurations. A similar mechanism is likely responsible for the site-selective adsorption of many other aromatic

electron-acceptor molecules with electronegative side groups on noble metal surfaces.

In Chapter 5, the energy level alignment of copper octaethylporphyrin (CuOEP) on three noble metal surfaces was studied. First, a review of different mechanisms that lead to a deviation of the vacuum level alignment rule was discussed. In-house ultraviolet photoemission results are presented and analyzed in the light of those different mechanisms. We could conclude that the dipole at the interface of CuOEP with noble metals is dominated by the push-back and polarization effects, while the charge transfer contribution is much smaller.

The field of aromatic molecules, self-assembled on metal surfaces, is an active one. There are a lot of experimental and theoretical efforts around the world. In this Thesis we concentrated on two particular aspects of this area of research. Apart from discussing the screening of the photo-hole in electron photoemission experiments, we dealt with electronic ground state properties. Even here many interesting problems remain. As a continuation of Chapter 4, it would be useful to study the adsorption properties of NTCDA on the other low-index silver surfaces, Ag(111) and Ag(001), as well as Cu(001), for which experimental data exist. For less reactive surfaces like Ag(111) and Ag(001) an approximate inclusion of dispersion forces would be highly desirable. Unfortunately, weak van-der-Waals interactions are not properly treated in present implementations of DFT. Further development of the so-called van-der-Waals DFT in surface science and its application to model systems is an interesting field on its own.

A very interesting topic for further research, inspired by Chapters 4 and 5, would be a theoretical study of work function shifts caused by an adsorption of chemically related molecules with variable electron accepting properties. One example is copper phthalocyanine (CuPc), and the related fluorinated phthalocyanines CuF_4Pc and $CuF_{16}Pc$. Those molecules have almost identical shapes, but change from electron donors to acceptors upon fluorination. Experiments show a reversal of work function shifts: the interface dipole is negative for CuPc and positive for $CuF_{16}Pc$. Theoretical studies should reveal the relationship among the energy spectra of the isolated molecules, the adsorption-induced charge rearrangement, and the site-specific bonding of this class of molecules, which are also used in organic electronics.

List of Publications

- L. Ramoino, S. Schintke, M. von Arx, M Wahl, A. Alkauskas, A. Baratoff, H.-J.Güntherodt, and T.A. Jung
  Local adsorption geometry and tunneling voltage-dependent submolecular contrast of copper octaethylporphyrin adsorbed on metals
  In preparation (2006).

- A. Alkauskas, A. Baratoff, and C. Bruder
  Site-selective adsorption of naphthalene-tetracarboxylic dianhydride on Ag(110): first principles calculation
  Phys. Rev. B **73**, 165408 (2006).

- A. Alkauskas, L. Ramoino, S. Schintke, M. von Arx, A. Baratoff, H.-J. Güntherodt, and T.A. Jung
  Energy level alignment at metal-octaethylporphyrin interfaces
  J. Phys. Chem. B **109**, 23558 (2005).

- L. Nony, E. Gnecco, A. Baratoff, A. Alkauskas, R. Bennewitz, O. Pfeiffer, S. Maier, A. Wetzel, E. Meyer, and C. Gerber
  Observation of individual molecules trapped on a nanostructured insulator
  Nano Lett. **4**, 2185 (2004).

- A. Alkauskas, A. Baratoff, and C. Bruder
  Gaussian form of effective core potential and response function basis set derived from Troullier-Martins pseudopotential: results for Ag and Au
  J. Phys. Chem. A. **108**, 6863 (2004).

- A. Alkauskas, B.Y.K. Hu, K. Flensberg, and A.-P. Jauho
  Sign reversal of drag in bilayer systems with in-plane periodic potential modulation
  Phys. Rev. B **66**, 201304(R) (2002).

- A. Alkauskas
  Tunneling of edge states. Non-interacting electrons
  Lith. J. Phys. **41**, 17 (2002).

- A. Alkauskas, J. Čeponkus, V. Aleksa, B. Mikulskienė, E. Butkus, and V. Šablinskas
  Conformational stability of bicyclo[3.3.1]nonane-2,6-dione and bicyclo[3.3.1]nonane-2,9-dione: ab-initio calculations and vibrational spectroscopy studies
  J. Mol. Struct. **563**, 517 (2001).

Curriculum Vitae

Audrius Alkauskas
Date of Birth - 1978 February 08
Citizenship - Lithuanian

Education

- 1985-1993: J. Biliūnas secondary school, Anykščiai, Lithuania;

- 1993-1996: Gymnasium of Kaunas University of Technology, Kaunas, Lithuania;

- 1996-2000: Undergraduate physics studies in Vilnius University, Lithuania;

- June 2000: Bachelor of Science (*Bakalauras*) degree from Vilnius University for the Thesis "Conformational studies of bicyclo[3.3.1]nonane-2,6-dione and bicyclo[3.3.1]-nonane-2,9-dione by means of vibrational spectroscopy and *ab initio* calculations";

- 2000-2002: Graduate physics studies in Vilnius University, Lithuania;

- Sep. 2001-Feb. 2002: Exchange student in the University of Copenhagen, Denmark;

- June 2002: Master of Science (*Magistras*) degree from Vilnius University for the Thesis "Coulomb drag in lateral superlattices";

- 2002-2006: PhD studies in the Institute of Physics, University of Basel, Switzerland.

To these professors I am grateful for my university education:
Vilnius University: V. Aleksa, M.L. Balevičius, V. Balevičius, A.R. Bandzaitis, J. Bučinskas, G. Dikčius, K. Glemža, J. Grigas, A. Gruodis, V. Ivaška, J.J. Kaladė, R. Kašuba, L. Kimtys, A. Matulis, A.V. Medeišis, E. Montrimas, V. Rinkevičius, V. Shugurov, A.P. Smilga, V. Smilgevičius, A. Stabinis, R. Stepanauskas, J. Storasta, V. Šablinskas, P.J. Žilinskas;
University of Copenhagen: K. Flensberg, P.E. Lindelof:
Technical University of Denmark: A.-P. Jauho;
University of Basel: A. Baratoff, C. Bruder, S. Goedecker, C. Schönenberger.